Accessible Adaptive Optics and Super-resolution Microscopy to Enable Improved Imaging



Nicholas James Hall

Linacre College

University of Oxford

A thesis submitted for the degree of

Doctor of Philosophy

Michaelmas 2020

For everyone who cheered me on as I ran
but never got to see me cross the finish line;
Tell them I made it

Acknowledgements

A particularly pernicious myth is that science is moved forward by lone geniuses - this idea is just that, a myth. It would have been impossible for me to get this far without an overwhelming amount of support, a full account of which would likely be as long as the thesis itself. Hopefully, this abbreviated form will suffice.

Firstly, I would like to thank my supervisors; Ian Dobbie, Martin Booth and Ilan Davis. Their input, feedback, expertise, and encouragement were invaluable to me. Ian in particular was always on hand to offer support and insight at critical moments. I owe everyone I worked alongside at Micron during my time a debt of gratitude, particularly Mick Philips and David Pinto; building and writing code for bespoke super-resolution microscopes has one hell of a learning curve, and you made it much easier for me to climb it. Thank you for showing me the ropes, answering my many questions and for tolerating my more vocal outbursts in the office when Python proved particularly adversarial.

I received incredible support from the Davis lab, particularly from Richard Parton, Josh Titlow and Dalia Sara Gala in providing biological samples and key feedback. From the Dynamic Optics and Photonics Group, I am extremely grateful to Mantas Žurauskas, Jacopo Antonello and Syed Hussain for their expertise and advice on adaptive optics. It has been my immense pleasure to learn from and work alongside such accomplished individuals.

My thanks to Sara Abrahamsson and Marcel Müller for their encouragement and willingness to collaborate with me on a number of occasions.

The 2016 ONBI cohort, program coordinator Peter Jezzard, and administrator Lisa Bligh all deserve thanks for building a supportive environment to enjoy camaraderie, laughter, and many, many caterpillar cakes.

Rick Lange, Sarah Fynes-Clinton, Barney Bridges, Leah Barton, John-Luke Treadgold, Simon Parnham, Jon Collins, Tim Curtis, and Kyle Hall have all given me unflagging support, encouragement, and enthusiasm. They have been boundless sources of joy, levity, and steadfast bulwarks when I needed them most. I will never forget their faultless kindness to me. If a man's wealth is indeed measured by his friendships, I am rich beyond all measure.

Finally, I would like to thank my family: my parents, Trevor and Karen Hall; my sister and brother-in-law, Annabelle and Christopher Holloway; and my sister, Meghan Hall. They have consistently been my most vocal supporters, and fierce sources of love and encouragement. The fruits of my labour are a testament to the good soil I was planted in and the nourishment I received from them.

You all have my eternal gratitude and my most heartfelt, effusive thanks.

Abstract

Many of the recent innovations in biological imaging have revolved around the quest for greater resolving power, ultimately culminating in the advent of super-resolution microscopy techniques. However, all microscopy techniques are vulnerable to optical aberrations which distort the light wavefront. This leads to a gulf between theoretical and practical resolution for an imaging system. For super-resolution techniques, this can lead to reconstruction artifacts or the failure of the imaging technique entirely.

Implementing adaptive optics (AO) in microscopy has already been shown to be highly effective at reducing these aberrations and yielding significant improvements to image quality and resolution in numerous proof of principle systems. Despite this, AO technology has yet to be widely adopted in microscopy. This is for two principle reasons. Firstly, AO implementations to date have not been robust or generalised which makes transferring them between microscopy systems, imaging modalities and sample type troublesome to impossible. Secondly, AO implementations to date have not been accessible to typical microscope users and instead have been the purview of AO microscopy specialists.

This thesis presents a generalised, robust implementation for AO; Microscope-AOtools. This implementation has all the necessary methods for setting up and operating an adaptive element in microscopy. It has a flexible, modular design which allows for easy transfer between imaging systems, modalities, hardware configurations and sample types. These methods are integrated into Microscope-Cockpit for user accessibility. The evidence of these claims are substantiated by a detailed description of Microscope-AOtools' successful deployment on both a spinning disk confocal system and a bespoke, upright structured illumination microscope with a range of sample types.

Contents

1 Introduction **1**

1.1 Introduction to Microscopy 1

1.1.1 Fluorescence microscopy 2

1.1.2 Resolution 4

1.2 Super-resolution Microscopy 9

1.2.1 Structured Illumination Microscopy 10

1.3 Optical Aberrations 18

1.3.1 Zernike Polynomials 19

1.3.2 Aberrations and Resolution 21

1.4 Adaptive Optics 21

1.5 Overview and Aims of the Thesis 25

2 Systems and Implementations **28**

2.1 Aurox Clarity System 28

2.1.1 Aurox Clarity System Optical Set-up 29

2.1.2 Image Formation in Aurox Clarity Module 30

2.2 DeepSIM 34

2.2.1 DeepSIM Optical Set-up 35

2.2.2 Optical Alignment 36

2.3 Control Software 40

2.3.1 *Python Microscope* 40

2.3.2 *Microscope-Cockpit* 40

3 Adaptive Optics Control Software **43**

3.1 Set-up Methods 44

3.1.1 Direct wavefront sensing 44

3.1.2 Zernike Mode Amplitude Measurement 50

3.1.3 Calibration 52

3.1.4 Characterisation . . . 55
3.1.5 System Aberration Correction . . . 59
3.2 Sample Correction Methods . . . 62
3.2.1 Sensorless Correction . . . 62
3.2.2 Image Quality Metric: Fourier Power . . . 66

4 Aberration Correction for Spinning Disk Confocal Microscopy 69
4.1 Aberrations and Image Formation . . . 69
4.2 Biological Exemplar . . . 69
4.2.1 Sample preparation . . . 69
4.2.1.1 Neuro-muscular Junction . . . 69
4.2.1.2 Egg chambers . . . 70
4.3 Experimental Results . . . 70

5 Enabling Structured Illumination Microscopy at greater depth 75
5.1 Sample Induced Aberrations in Structured Illumination Microscopy 75
5.2 IsoSense . . . 77
5.3 Experimental Setup . . . 78
5.4 Biological Exemplar . . . 79
5.4.1 Sample preparation . . . 80
5.5 Experimental Results . . . 80

6 Discussion 86
6.1 Limitations of Microscope-AOtools . . . 86
6.1.1 Zernike mode fitting accuracy . . . 86
6.1.2 Sensorless correction accuracy . . . 90

7 Conclusions 94
7.1 Summary of Contributions . . . 94
7.2 Future development . . . 95
7.3 Final Conclusion . . . 98
7.4 Distribution . . . 99

A Noll indexing and Zernike polynomial expansions 100

B Point object seperation figure generation 102
B.1 Ideal point object seperation . . . 102
B.2 Aberrated point object seperation . . . 104

Bibliography **109**

List of Figures

1.1 Example excitation and emission spectra . . . 3
1.2 A simplified schematic of a light microscope. . . . 5
1.3 Illustration of the resolution limit as determined by the Rayleigh criterion . . . 6
1.4 Widefield observable region visualisation . . . 9
1.5 Visualisation of moiré fringes . . . 11
1.6 Resolution enhancement with 2D SIM imaging . . . 15
1.7 Resolution enhancement with 3D SIM imaging . . . 17
1.8 A visualisation of the effect of optical aberrations on image resolution 22
1.9 Illustration of aberrations affecting a microscope objective focus. . . . 23
1.10 Schematic of the emission path of an adaptive optics system. . . . 24
1.11 Flowchart depicting the general process for building a system utilising AO. . . . 25

2.1 Aurox system beam path layout . . . 29
2.2 Simplified Nipkow-Petran confocal layout . . . 31
2.3 A simple schematic diagram of a transmissive optical system . . . 31
2.4 Complete beam path layout for DeepSIM. . . . 37
2.5 The aligned DeepSIM optical set-up. . . . 39
2.6 Microscope-Cockpit GUI for controlling DeepSIM . . . 41

3.1 Microscope-Cockpit GUI DM specific functionality . . . 45
3.2 User interface for selecting the interferometric region of interest . . . 46
3.3 Visualisation of the stages of the phase acquisition workflow. . . . 48
3.4 User interface for viewing the phase wavefront . . . 50
3.5 Visualisation of the influence function fitting stage of the calibration routine . . . 55
3.6 Calibration routine workflow . . . 56
3.7 Characterisation routine workflow . . . 57

3.8 Example characterisation routine results 58
3.9 Direct wavefront correction workflow 60
3.10 Example direct wavefront correction results 61
3.11 Principle of sensorless adaptive optics correction. 63
3.12 Sensorless adaptive optics correction workflow 64
3.13 Visualisation of the modulation mask 68

4.1 Depth comparison of the Aurox imaging system 72
4.2 *Drosophila* egg chamber data acquired on the Aurox imaging system 73
4.3 *Drosophila* neuro-muscular junction data acquired on the Aurox imaging system 74

5.1 IsoSense pattern visualisation. 79
5.2 Argolight slide data 82
5.3 Live *Drosophila* neuro-muscular junction data acquired on the DeepSIM imaging system 84
5.4 Fourier plots of *Drosophila* neuro-muscular junction data acquired on the DeepSIM imaging system 85

6.1 The effect of image size on Zernike mode fitting accuracy 88
6.2 The effect of image resizing on Zernike mode fitting accuracy 89
6.3 Effect of parameter bounds on sensorless correction fitting accuracy 91
6.4 Visual distinction between unsuccessful and successful sensorless correction routines 93

Chapter 1

Introduction

1.1 Introduction to Microscopy

The principle of optical magnification was known at least as early as the 1st Century CE. The enhancement of resolving power for objects viewed through spherical glass objects filled with water (a kind of proto-lens) was noted by Seneca and some of his contemporaries[1]. Even after the collapse of the Roman Empire and Europe entered the Dark Ages other scholars, such as Ibn al-Haytham, noted and investigated the phenomenon of optical magnification through convex-planar pieces of glass[2]. Given the importance which microscopy has had in furthering biological understanding, it is an amusing anecdote that it took over a millennia for anyone to identify an application for the phenomenon of magnification. It was not until the end of 13th Century when Roger Bacon penned his *Opus majus* that a practical use for magnification could be found - eyeglasses. It was a further 300 years until the first telescopes and microscopes were developed. The exact date and inventor of the first telescope is unknown, but the credit is usually attributed to one of four Dutchmen at the start of the 17th Century; Hans Janssen, his son Zacharias, Hans Lippershey, or Jacob Metius. Likewise, precise date and inventor of the first microscope is not known, but the invention did occur at around the same time and the term was coined by Giovanni Faber in 1625[3]. It is interesting to note that the invention of microscopes and telescopes are so closely linked, and that both astronomy and microscopy continue to enjoy a mutually beneficial relationship. The true power of microscopes to yield novel biological understanding was first popularised by Robert Hooke and then later by Antonie van Leeuwenhoek[4, 5]. Since then, the microscope has been and remains one of the premiere tools enabling biological discoveries.

1.1.1 Fluorescence microscopy

Microscopes allowed biologists to visualise structures well below the length-scale available to the naked eye. However, living material still remained resistant to optical examination due to a number of properties: strong scattering properties, particularly for wavelengths of light within the visible spectrum; transparency; innate light-protective mechanisms to prevent damage from solar radiation. Phase contrast microscopy could solve some of the issues when visualising otherwise transparent samples[6]. More typically microscopy samples were chemically fixed as these samples were more stable and easier to refractive index match to the microscope. Histological staining was, for decades, the primary method for revealing biological structures[7]. The properties and functions of living material were then inferred from fixed samples. This was, as one author put it, "like reconstructing a football game from a series of still pictures,...an arduous (and some would say hopeless) endeavour"[8].

Fluorescence microscopy enabled the selective visualisation of specific molecules, as well as the imaging of dynamic processes *in situ*. Fluorescence is the property of atoms and molecules whereby they emit light after stimulation from an external energy source. In steady-state conditions (i.e. without an external energy source) the electrons of the atom are found in the ground state. Photons from the external energy source are absorbed by these electrons, raising them to excited singlet states. When these excited electrons return to the ground state, they can release their energy as a photon - it is this phenomenon which is called fluorescence[9]. For atoms, these energy states are discrete and (for the lowest levels) easy enough to draw in Jabłonski diagrams. Molecules capable of fluorescence, called fluorophores, have more complex energy level landscapes and broad "energy bands" of possible excitation and emission wavelengths. Additionally, the absorption and emission cross-sections are not the same for all wavelengths. This leads to excitation and emission spectra for fluorescent molecules. Figure 1.1 shows the excitation and emission spectra for Green Fluorescent Protein (GFP), generated with SpekCheck[10].

The first fluorescence microscopes were developed at the beginning of the 20th Century[8, 11]. The real power of fluorescence microscopy came as the specificity of labelling improved. The first iteration of this was the development of antibody fluorescent labelling which allowed for, among other things, localisation of viral particles in biological cultures[12, 13, 14]. The second iteration was the

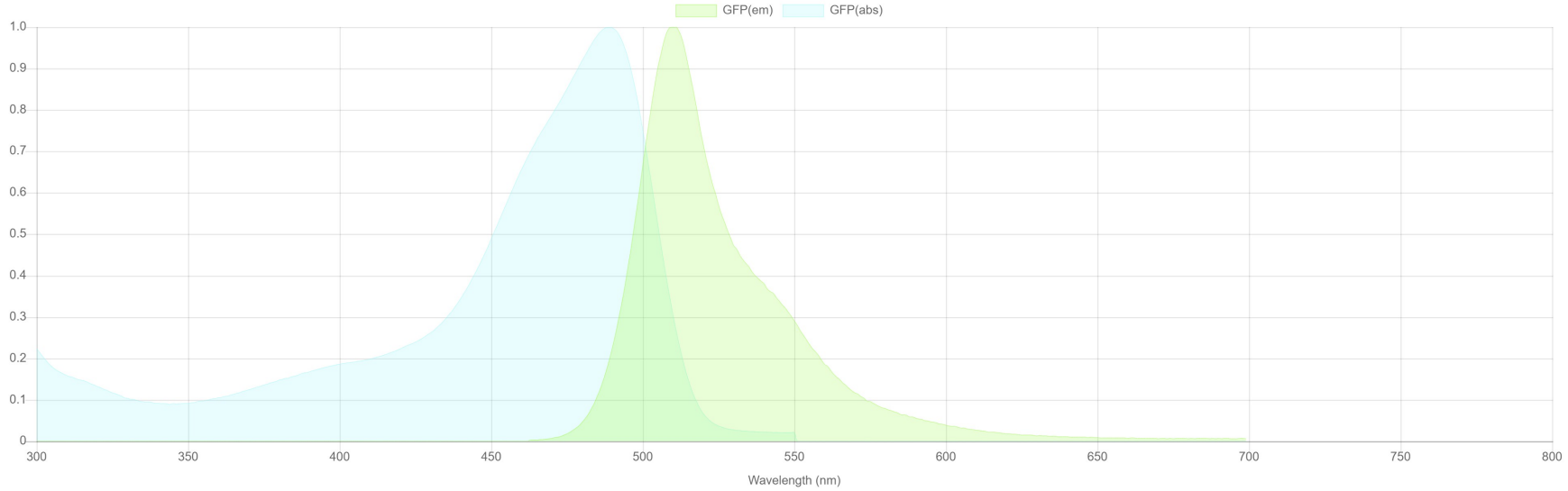


Figure 1.1: *Example excitation (blue) and emission (green) spectra for Green Fluorescent Protein. Generated with SpekCheck[10]*

discovery and cloning of *Aequorea Victoria* GFP, and the development of chromatic variants[15, 16]. This development was arguably more profound since previous fluorophores were synthetic molecules which, despite better photostability and a higher fluorescence quantum yield, proved ill-suited to cell imaging due to difficulties establishing a specific linkage between them and a target protein, and their toxic effects inside the cell.[17] The development of organic fluorescent tags such as GFP allowed for specific proteins of interest to be individually labelled enabling, for example, biologists to monitor *in vivo* processes such as gene-expression[18]. Since then, additional properties of fluorescent proteins, such as their conformational changes in response to binding events, environmental changes, or enzymatic activity, have been utilised to great effect[19]. Fluorescence microscopy has allowed biologists to visualise dynamic biological processes in real time.

1.1.2 Resolution

A fundamental property of all microscopes and microscopy images is that of resolution - the minimum separation between two objects where they can still be observed as two distinct objects. This should not be confused with either magnification or contrast. Magnification is the ratio between the apparent object size (i.e. the size of an object in the image taken of it) and its true size. Contrast, in this context, is a measure of the confidence that the observed signal corresponds the presence of the molecules/proteins of interest to which the fluorophores are conjugated. For example, a fluorophore with highly non-specific binding may be imaged by a microscope with both high magnification and resolution. However, since much of the observed signal might originate from binding sites other than the one of interest, such an image would still be said to have low contrast.

Consider an optical plane, **O**, where a biological specimen is placed - the 'sample plane'. Also consider a separate optical plane, **O'**, where the image of the specimen is formed - the 'image plane'. The microscope, with circular entrance and exit pupils, maps the field distributions between **O** and **O'**. Figure 1.2 shows a schematic of this simplified system.

Consider a point source located at **O** in a media of refractive index, n, isotropically emitting monochromatic light of wavelength λ. Every ray forms an angle, θ, with the optical axis **OO'**. The highest angle collected by the entrance pupil is α. A point source can be considered an infinitely narrow aperture and α determines the highest diffraction order which the entrance pupil - i.e. the microscope objective aperture - can collect[20]. Considering this and, more generally, the diffraction of

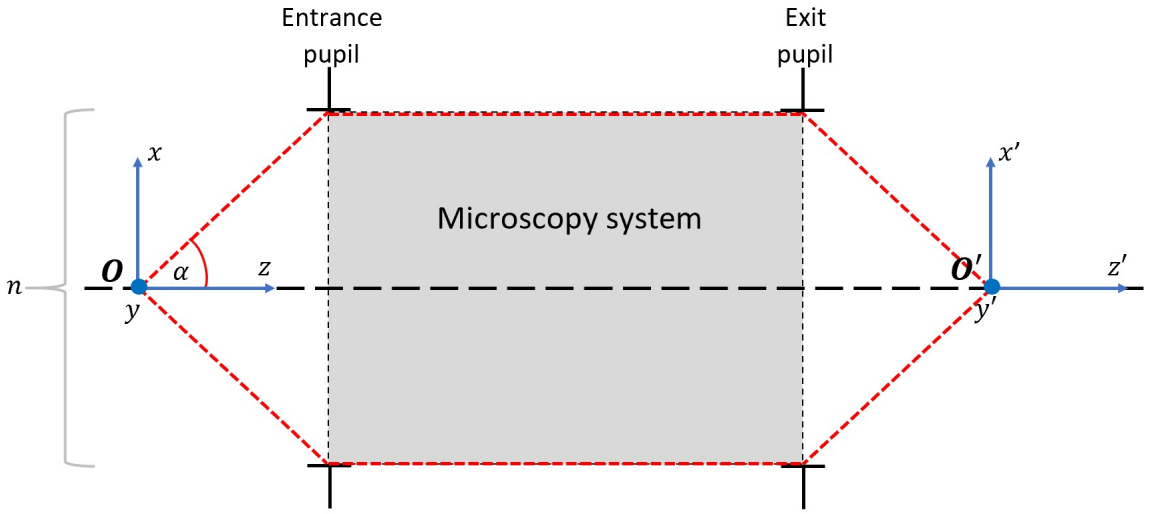


Figure 1.2: *A simplified schematic of a light microscope. A specimen is placed at the sample plane,* ***O****, in refractive index, n. Light rays emerging from* ***O*** *are collected by the entrance pupil. These rays process through the microscope system before emerging at the exit pupil and being focused at the image plane,* ***O′****. The light rays which form an angle with the optical axis,* ***OO′****, of α are called marginal rays. Marginal rays are the highest angle of light collectable by the entrance pupil and therefore the microscope system as a whole.*

light through a circular aperture it is possible to obtain that the field intensity at **O′** is proportional to[21, 22]:

$$\mathcal{I}_w(v) = \left| \frac{2\mathcal{J}_1(v)}{v} \right|^2, \tag{1.1}$$

where $\mathcal{J}_1(v)$ is the first-order Bessel function of the first kind of the variable v[23]. v is the normalised lateral co-ordinate given by[24]:

$$v = \frac{2\pi}{\lambda} rn \sin(\alpha). \tag{1.2}$$

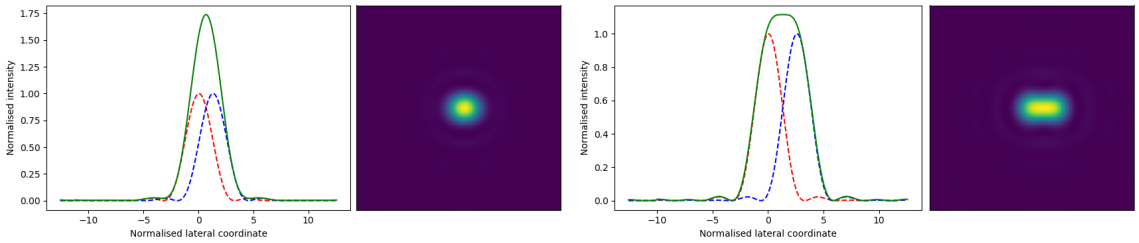
r is the radial displacement in the image plane **O′**, $r = \sqrt{x'^2 + y'^2}$. A useful quantity, and one often cited by microscope objective manufacturers, is the numerical aperture, $NA = n \sin(\alpha)$. The Rayleigh criterion determines that the limit at which two point objects can be meaningfully separated is when the central maxima of one diffraction pattern lies in the first minimal of the other[25, 26]. For a first order Bessel function, this occurs at $v \approx 1.22\pi$. Therefore, the lateral resolution limit, r_l is often quoted as:

$$r_l \approx \frac{1.22\lambda}{2NA} \tag{1.3}$$

otherwise known as the Rayleigh criterion[25]. Through a similar process and considering the field intensity along the z' axis, the axial resolution, r_a, is given as[27]:

$$r_a \approx \frac{2\lambda n}{NA^2}. \tag{1.4}$$

Figure 1.3 shows two diffraction limited point objects at variable lateral separations. For lateral separations less than r_l the field intensities resemble a single point source in the image plane. For lateral separation at or above r_l the intensity contributions from the two objects are distinguishable as separate.



(a) *Object separation* = $0.41r_l$ **(b)** *Object separation* = $0.82r_l$

(c) *Object separation* = $1.0r_l$ **(d)** *Object separation* = $1.23r_l$

Figure 1.3: *Illustration of the resolution limit as determined by the Rayleigh criterion. Each subfigure shows a line profile and 2D plot of the field intensity distributions of both of the two diffraction limited point objects. For two point objects separated by* $< r_l$, ***(a)*** *&* ***(b)****, they are not separable as individual objects. At a separation* $\geq r_l$, ***(c)*** *&* ***(d)****, the two point objects are separable. These figures were generated using the code presented in Appendix B.1*

Several approximations had to be made to obtain Equations 1.3 and 1.4. Firstly, the Fraunhofer and paraxial approximations are assumed to hold[21]. The Fraunhofer, or far-field, approximation is given as[28]:

$$r \gg \frac{\pi a^2}{\lambda}, \tag{1.5}$$

Where a is aperture or slit size (in this case the diameter of a circular aperture), r is the distance from the aperture, and λ is the wavelength of light as before. The paraxial, or small angle, approximation is given as[29]:

$$\sin(\theta) \approx \tan(\theta) \approx \theta \qquad \cos(\theta) \approx 1. \tag{1.6}$$

Where θ is the angle a ray makes with the optical axis. Additionally, the microscope system has been greatly simplified to essentially just the entrance and exit pupils. More complex but accurate models for modern microscopy set-ups have been demonstrated[30, 31]. Finally, this idealised system only considers the shape of the apertures - i.e. the entrance and exit pupils - and the wavelength of light. If one were to observe objects such as these, with these field distributions corresponding to well-specified models, there would be no resolution limit at all[32]. In practice, the field distributions of objects are not precisely known, therefore determining the location of the first minima is not as simple as it has been presented here. The first minima may not even be radially symmetric.

Furthermore, the 'true' resolution achievable by a microscopy system is affected by other factors such as the signal-to-noise ratio of an image, coherence conditions of illumination, apodization, discretisation errors for digital cameras, to name a few[32]. An alternative formulation of the lateral resolution limit in Equation 1.3 is known as the Abbe diffraction limit[33]:

$$r_l = \frac{\lambda}{2NA} \tag{1.7}$$

One of the key distinctions between the Abbe diffraction limit and the Rayleigh criterion is that the Rayleigh based his criterion on the sensitivity of the human eye to intensity variations[34]. There have been attempts to develop alternative resolution measurements for point objects[35]. Unfortunately, the actual resolution achieved in biological samples varies across the image plane, determined by factors such as the labelling density of the underlying biological specimen[36]. The 'true' resolution of a system for a given sample is therefore a quantity which is impossible to determine analytically. The ideal lateral and axial resolutions in Equations 1.3 and 1.4 are nonetheless useful quantities as the theoretical, ideal resolution limit of a microscopy system.

Returning to the concept of a point object as an infinitely narrow aperture allows for a more complete understanding of the resolution limit. A spatially structured object can be described by a superposition of spatial frequencies in the same manner in which a temporally structured object can be described by a superposition of temporal frequencies, which is the basis for Fourier optics[21]. A point object can be described as a Dirac delta function, the Fourier transform of

which is a uniform distribution across all spatial frequencies. The addition of an aperture, such as a microscope objective, effectively imposes a low-pass filter on the spatial frequency domain. Figure 1.4c shows the projection of the observable region onto the lateral spatial frequency plane $k_x k_y$ i.e. the low-pass filter. The radius of this low-pass filter is:

$$\omega_l = \frac{1}{r_l}, \tag{1.8}$$

where r_l is the lateral resolution limit. The bounds of the observable region in k_z differs since the intensity spectrum - the power spectrum of the field intensity - in k_z is independent of the object nature and the point spread function[37]. The bounds of the observable region in k_z can be shown to be:

$$k_z = \pm \frac{\left\|\mathbf{k}_{xy}\right\|}{2\lambda_k}(\omega_l - \left\|\mathbf{k}_{xy}\right\|), \tag{1.9}$$

for $\left\|\mathbf{k}_{xy}\right\| \leq \omega_l$ where $\left\|\mathbf{k}_{xy}\right\|$ is the length of the vector denoting the lateral spatial frequencies, (k_x, k_y) and $\lambda_k = \frac{2\pi}{\lambda}$[37]. Figure 1.4b shows the projection of the observable region onto the axial spatial frequency plane $k_x k_z$. The maximum extension of this observable region, k_a, is given by:

$$\omega_a = \frac{\omega_l^2}{8\lambda_k}, \tag{1.10}$$

From Equation 1.9, the observable region in k_z is bandpass limited at both high and low spatial frequencies. This results in the "missing cone" phenomenon which limits the axial spatial frequencies which are able to be collected, in turn limiting the axial resolution[38, 39]. This, coupled with the fact that for all practical cases $\omega_a \ll \omega_l$, explains why the axial resolution is always worse than the lateral resolution of a system. Figure 1.4c shows the complete 3D observable region, obtained by rotating Figure 1.4b around the k_z axis. Only spatial frequencies within this observable region contribute to the observed sample structure. The observable region can be described as:

$$O_0(\mathbf{k}) = \begin{cases} 1, & if \ \left\|\mathbf{k}_{xy}\right\| < \omega_l \ and \ \|k_z\| < \frac{\left\|\mathbf{k}_{xy}\right\|}{2\lambda_k}(\omega_l - \left\|\mathbf{k}_{xy}\right\|) \\ 0, & otherwise \end{cases}. \tag{1.11}$$

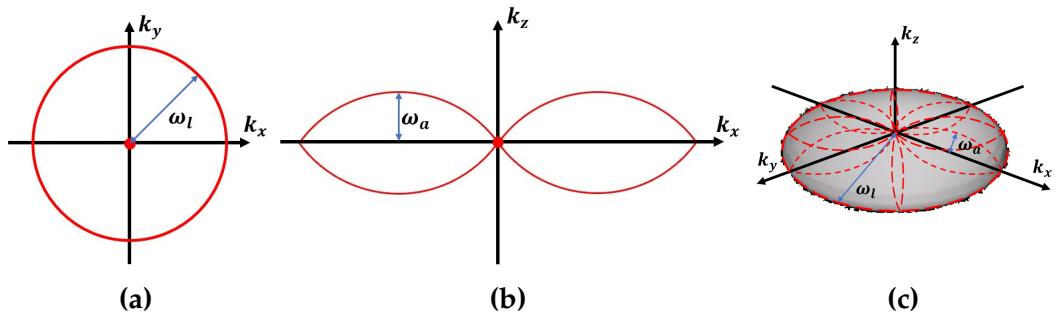


Figure 1.4: *Widefield observable region visualisation.* ***(a)*** *The projection of the observable region onto the k_xk_y plane.* ***(b)*** *The projection of the observable region onto the k_xk_z plane.* ***(c)*** *The full observable region for a conventional widefield microscope in reciprocal space.*

1.2 Super-resolution Microscopy

For some time, the diffraction limit represented a kind of practical resolution asymptote - a point to be approached but never reached. Two 'gold standard' techniques for optical bioimaging emerged thanks to their ease of implementation and how close they were able to get to the diffraction limit; deconvolution[40, 41] and confocal laser scanning microscopy[42, 43]. Nonetheless, the instant one defines a limit it is practically human nature to attempt to surpass it. Therefore, a number of 'super-resolution' techniques have emerged capable of surpassing even the ideal diffraction limit. These can be broadly divided into two categories: near-field and far-field methods. Near-field methods, whilst capable of achieving resolutions of $\sim 20nm$, are only suitable for surface structure imaging[44]. Far-field techniques fall into 4 broad categories: structured illumination microscopy (SIM), stimulated emission depletion (STED) microscopy, single-molecule localisation microscopy (SMLM) and interferometric-based techniques. There are some implementations which combine several techniques. Table 1.1 shows the typical lateral and axial resolution limits of the conventional and far-field super-resolution techniques, as well as whether these resolutions are primarily affected by the numerical aperture of the imaging system[44, 45, 46, 47, 48, 49]:

Imaging technique	Typical lateral resolution	Typical axial resolution	Resolution affected by NA?
Widefield (with deconvolution)	180-250 nm	600-800 nm	Yes
Confocal	180-250 nm	500-700 nm	Yes
3D SIM	100-130 nm	250-400 nm	Yes
3D STED	20-100 nm	20-100 nm	No
SMLM	10-50 nm	20-100 nm	No

Table 1.1: *Typical lateral and axial resolutions of the imaging technique categories and whether those resolutions are affected by numerical aperture.*

Each super-resolution technique has benefits and drawbacks which need to be considered when employing them including; the resolution (laterally and axially) required and the resolution achievable with each technique, acquisition speed, photodamage incurred, depth of imaging and multi-colour capability[50, 45] Although it has a modest resolution improvement, SIM is the most widely utilised super-resolution technique for biological imaging thanks to its multi-colour capability, high temporal resolution and low photodamage impact[51].

1.2.1 Structured Illumination Microscopy

There are a number of microscopy techniques which fall under the structured illumination microscopy umbrella: Re-scan[52], Airyscan[53], iSIM[54, 55], and SIMFlux[56] to name a few. Whilst all these can be considered 'structured illumination' techniques since they do rely on spatially structured excitation light, for the duration of this thesis the term 'structured illumination microscopy' or SIM refers to the form of interference-based microscopy pioneered by Mats Gustafsson[57, 58, 49, 59]. This implementation of SIM is best understood through the moiré effect. Two patterns, such as those shown in Figure 1.5a and 1.5b, which are multiplicatively superimposed on one another will produce a beat pattern - moiré fringes - such as those shown in Figure 1.5c. Using the convolution theorem, the Fourier transform of this superposition is equivalent to the convolution of the Fourier transforms of the two original patterns[60], as shown in Figures 1.5d-1.5f.

For SIM, one of the patterns is the underlying biological structure - or more specifically the spatial distribution of fluorophores - and the other is the spatially structured excitation illumination. The moiré fringes arising from the superposition of these two structures can be coarser than either of the original patterns, meaning

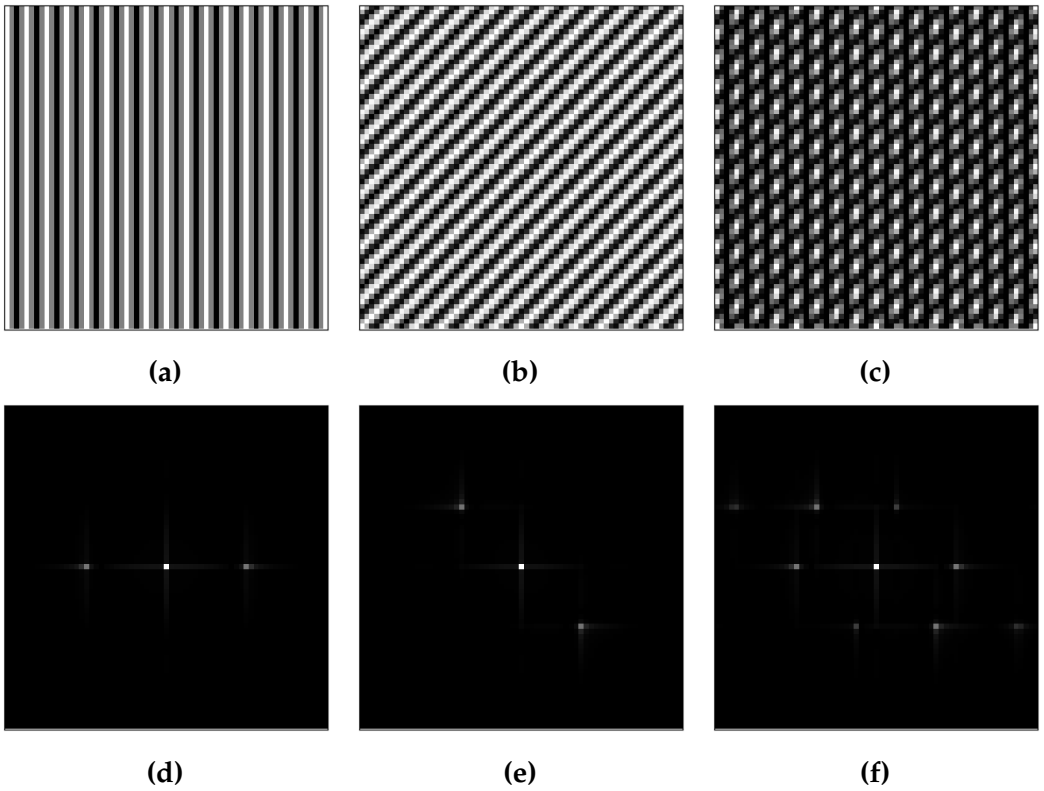


Figure 1.5: *Visualisation of moiré fringes.* ***(a)-(b)*** *shows two spatially structured images.* ***(c)*** *shows the resultant moiré fringes arising from the interference of* ***(a)*** *and* ***(b)****.* ***(d)-(f)*** *shows the respective Fourier transforms of* ***(a)-(c)****. Note that* ***(f)*** *is a convolution of* ***(d)*** *and* ***(e)***

that moiré fringes arising from the superposition of biological structures beyond the resolution limit of the microscope and a known illumination pattern can be observed. These moiré fringes contain information about these super-resolution structures and the super-resolution information can be extracted from the moiré fringes, effectively extending the observable region of a microscope beyond the diffraction limit[49].

A single fluorescent image, $F(\mathbf{r})$, is defined by:

$$\begin{aligned} F(\mathbf{r}) &= (E \circledast H)(\mathbf{r}) \\ F(\mathbf{r}) &= [D(\mathbf{r})I(\mathbf{r})] \circledast H(\mathbf{r}), \end{aligned} \tag{1.12}$$

where $D(\mathbf{r})$ is the sample fluorescence distribution, $I(\mathbf{r})$ is the illumination pattern, $E(\mathbf{r})$ is the resultant emission signal, $H(\mathbf{r})$ is the system point spread function (PSF) and $\circledast$ represents the convolution operation. Applying the convolution theorem and a Fourier transform yields:

$$\begin{aligned}\mathcal{F}\left[F(\mathbf{r})\right] &= \mathcal{F}\left[\left[D(\mathbf{r})I(\mathbf{r})\right] \circledast H(\mathbf{r})\right] \\ \tilde{\mathbf{F}}(\mathbf{k}) &= \left[\tilde{\mathbf{D}}(\mathbf{k}) \circledast \tilde{\mathbf{I}}(\mathbf{k})\right] \tilde{\mathbf{H}}(\mathbf{k}) \quad , \\ \tilde{\mathbf{F}}(\mathbf{k}) &= \left[\tilde{\mathbf{D}}(\mathbf{k}) \circledast \tilde{\mathbf{I}}(\mathbf{k})\right] O(\mathbf{k}),\end{aligned} \tag{1.13}$$

where bold text and $\sim$ indicates the Fourier transform of the respective real-space functions. $O(\mathbf{k}) = \tilde{\mathbf{H}}(\mathbf{k})$ is the optical transfer function (OTF) of the imaging system. The complex values of $O(\mathbf{k})$ describe the attenuation of the spatial frequencies within the observable region described by Equation 1.11. For uniform illumination - i.e. widefield imaging - $\tilde{\mathbf{I}}(\mathbf{k}) = \delta(0)$ where δ is the Dirac delta function, and therefore only the spatial frequencies within the observable region contribute to the image formation as previously noted. However, if $I(\mathbf{r})$ is spatially structured then the convolution $\tilde{\mathbf{D}}(\mathbf{k}) \circledast \tilde{\mathbf{I}}(\mathbf{k})$ is non-local and the data within the observable region contains contributions from spatial frequencies which are normally outside the observable region.

For a general illumination pattern, extracting these super-resolution contributions from the diffraction limited contributions is non-trivial. However, imposing some conditions on the illumination structure simplifies this process[59]. Firstly, the illumination pattern should consist of the sum of a finite number, m, of components and these components should be separable into axial and lateral components. The illumination pattern, $I(\mathbf{r}_{xy}, z)$, is therefore:

$$I(\mathbf{r}_{xy}, z) = \sum_m I_m(z) J_m(\mathbf{r}_{xy}), \tag{1.14}$$

where $\mathbf{r}_{xy}$ the vector denoting the lateral coordinates, (x, y). Secondly, the lateral functions, $J_m(\mathbf{r}_{xy})$, should be purely harmonic functions meaning they contain only one spatial frequency. Note that the lateral functions, J_m, should not be confused with the first-order Bessel functions, $\mathcal{J}_1$, from before. Finally, the axial functions, $I_m(z)$, should either:

1. also be purely harmonic functions.

2. in instances where 3D data is acquired as a series of 2D images with different focus - as in microscopy - the illumination pattern is maintained fixed relative to the focal plane of the microscope and not relative to the objecting being imaged.

The first and third conditions allow Equation 1.12 to be written as:

$$\begin{aligned} F(\mathbf{r}) &= [D(\mathbf{r})I(\mathbf{r})] \circledast H(\mathbf{r}) \\ F(\mathbf{r}) &= \sum_m \int H(\mathbf{r}-\mathbf{r}')I_m(z-z')D(\mathbf{r}')J_m(\mathbf{r}'_{xy})d\mathbf{r}' \\ F(\mathbf{r}) &= \sum_m \left[HI_m \circledast DJ_m\right](\mathbf{r}) \end{aligned}, \tag{1.15}$$

where $\mathbf{r}'$ denotes the sample reference frame, $\mathbf{r}$ denotes the data-set reference frame and $\mathbf{r}-\mathbf{r}'$ denotes the reference frame of the objective. Taking the Fourier transform of the m-th term, $F_m(\mathbf{r})$, yields:

$$\tilde{\mathbf{F}}_m(\mathbf{k}) = \tilde{\mathbf{O}}_m \left[\tilde{\mathbf{D}}(\mathbf{k}) \circledast \tilde{\mathbf{J}}_m(\mathbf{k}_{xy})\right], \tag{1.16}$$

where $\tilde{\mathbf{O}}_m = O \circledast \tilde{\mathbf{I}}_m = \mathcal{F}[HI_m]$. Here the second condition of the lateral functions being purely harmonic allows $J_m(\mathbf{r}_{xy})$ to be written as:

$$J_m(\mathbf{r}_{xy}) = e^{i\left(2\pi\mathbf{p}_m\cdot\mathbf{r}_{xy}+\phi_m\right)}, \tag{1.17}$$

$$\Rightarrow \tilde{\mathbf{J}}_m(\mathbf{k}_{xy}) = \delta\left(\mathbf{k}_{xy}-\mathbf{p}_m\right)e^{i\phi_m}, \tag{1.18}$$

Substituting Equation 1.18 into Equation 1.16 and summing over all m components, the observed data can be written as:

$$\tilde{\mathbf{F}}(\mathbf{k}) = \sum_m \tilde{\mathbf{O}}_m(\mathbf{k})e^{i\phi_m}\tilde{\mathbf{D}}\left(\mathbf{k}-\mathbf{p}_m\right). \tag{1.19}$$

Therefore, each image is a sum of a finite number, M, copies of the object information, $\tilde{\mathbf{D}}$, each shifted laterally in reciprocal space by $\mathbf{p}_m$, filtered by the OTF, O, and phase shifted by ϕ_m. Acquiring M images with different values of ϕ_m gives a system of linear equations with as many equations as unknowns. The frequency components can therefore be separated by applying an $M \times M$ separation matrix. The values of ϕ_m are generally chosen to be evenly spaced between $[0, 2\pi]$ radians to ensure a well-conditioned separation matrix such that $\phi_m = m\phi$[59].

Considering the practical implications further simplifies the situation. Firstly, the intensity distribution of light is a real-valued function and therefore the exponentials in Equation 1.18 must occur in pairs with $\pm\mathbf{p}_m$. Since the Fourier transform of a real-valued function has the symmetry property $\tilde{\mathbf{a}}(-\mathbf{k}) = \tilde{\mathbf{a}}^*(\mathbf{k})$ (where $\tilde{\mathbf{a}}^*$ is the complex conjugate of $\tilde{\mathbf{a}}$) only one component need be calculated and the other can be determined by symmetry. Secondly, if the $\mathbf{p}_m$ are chosen

such that they are all either the fundamental frequency or higher harmonics of the same frequency then $\mathbf{p}_m = m\mathbf{p}$ where $\mathbf{p}$ is the fundamental frequency Taking these effects into account, Equation 1.19 becomes:

$$\tilde{\mathbf{F}}(\mathbf{k}) = \sum_m \tilde{\mathbf{O}}_m(\mathbf{k}) e^{im\phi} \tilde{\mathbf{D}}\left(\mathbf{k} - m\mathbf{p}\right). \tag{1.20}$$

Since O_m and $\mathbf{p}_m$ are known, the information components can be separated and moved by $\mathbf{p}_m$ back to their correct position in reciprocal space, combined to a single extended resolution spatial frequency dataset, and finally Fourier transformed back into a single super-resolution image. From Equation 1.19 it is clear that this image is equivalent to an image taken with an observable region equal to the convolution of the original system OTF, O, and the illumination structure Fourier transform, $\tilde{\mathbf{I}}$.

Consider an illumination pattern formed by the interference of two beams of light such that $I(\mathbf{r}) \propto 1 + \cos(\mathbf{r} \cdot \mathbf{p} + \phi)$. Figure 1.6a shows the amplitude wave vectors for these beams, both with the same length $\frac{1}{\lambda_{ex}}$ where λ_{ex} is the wavelength of the excitation illumination light. The angle between the two beams determines the position of $\mathbf{p}$. If $\mathbf{p}$ is chosen to be close to k_l then the spatial frequency components are close to the bounds of the observable region, as shown in Figure 1.6c. The convolution of this illumination pattern with the system OTF is shown in Figure 1.6d. The projection of this extended observable region on the $k_x k_z$ plane is shown in Figure 1.6e. The observable region is laterally extended by a factor, α_l, given by:

$$\alpha_l = \frac{\left(\frac{1}{\lambda_{ex}} + \frac{1}{\lambda_{em}}\right)}{\frac{1}{\lambda_{em}}} = 1 + \frac{\lambda_{em}}{\lambda_{ex}}, \tag{1.21}$$

where λ_{ex} and λ_{em} are the excitation and emission wavelengths respectively. However, this extension factor only applied in the direction $\overrightarrow{\mathbf{p}}$. To achieve isotropic resolution enhancement, a number of pattern directions are required. Rotating the illumination pattern through the three stripe angles shown in Figure 1.6b yields the close to isotropic extended observable region in Figure 1.6f, the projection of which in the $k_x k_y$ plane is shown in Figure 1.6g.

Figure 1.6g shows that whilst there is an expansion of the observable region in all directions in the $k_x k_y$ plane, it is not a lateral isotropic extension by α_l. Nonetheless, it is still sufficient to yield a doubling of the lateral resolution[49].

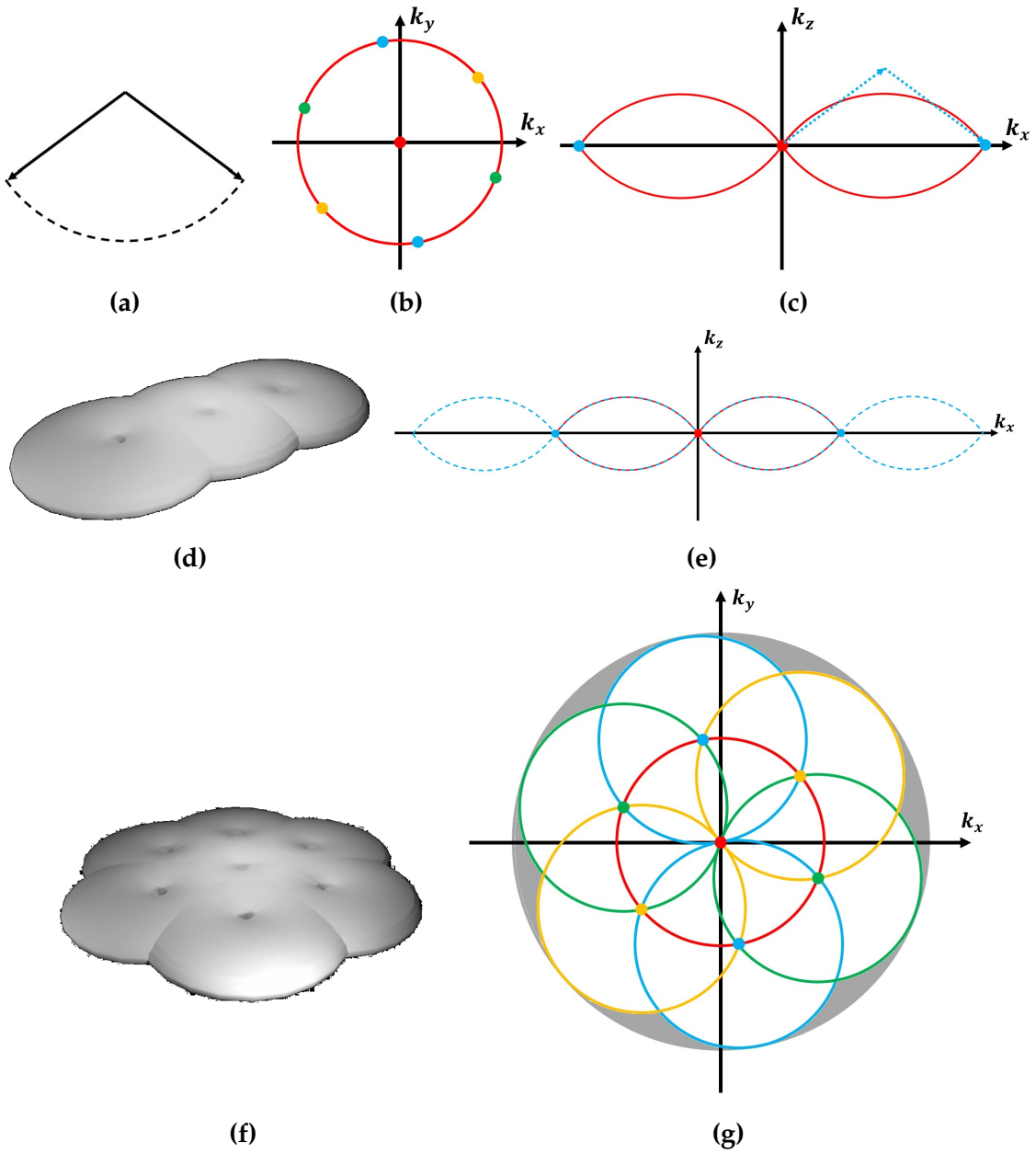


Figure 1.6: *Resolution enhancement with 2D SIM imaging.* ***(a)*** *The amplitude wave vectors corresponding to the 2 illumination beams. Both vectors have the same magnitude,* $\frac{1}{\lambda}$ ***(b)*** *The projection of the observable region onto the* $k_x k_y$ *plane with the stripe angles shown* ***(c)*** *The projection of the observable region onto the* $k_x k_z$ *plane with the spatial frequency component locations for two-beam interference pattern shown.* ***(d)*** *The full observable region extension for one angle in reciprocal space.* ***(e)*** *The projection of the extended observable region in* ***(d)*** *onto the* $k_x k_z$ *plane.* ***(f)*** *The full observable region extension for all three angles in reciprocal space.* ***(g)*** *The projection of the extended observable region in* ***(f)*** *onto the* $k_x k_y$ *plane. The shaded grey area shows the reciprocal components missing for an isotropic observable region extension factor* α_l.

This choice of illumination structure still suffers from the missing cone problem noted in Section 1.1.2, meaning there is no improvement in axial resolution.

Now consider an illumination pattern formed by three light beams with wave vectors, $\mathbf{k}_j$, such as those shown in Figure 1.7a. The 3D interference pattern, $I(\mathbf{r})$ generated by the superposition of these waves:

$$\begin{aligned} I(\mathbf{r}) \propto \left| \sum_j \mathbf{E}_j e^{i\mathbf{k}_j \cdot \mathbf{r}} \right|^2 &= \left(\sum_j \mathbf{E}_j^* e^{-i\mathbf{k}_j \cdot \mathbf{r}} \right) \left(\sum_q \mathbf{E}_q e^{i\mathbf{k}_q \cdot \mathbf{r}} \right) \\ &= \sum_{j,q} \mathbf{E}_j^* \cdot \mathbf{E}_q e^{-i\left(\mathbf{k}_q - \mathbf{k}_j\right) \cdot \mathbf{r}}, \end{aligned} \tag{1.22}$$

therefore has 7 Fourier components located at each of the pairwise difference vectors, $\left(\mathbf{k}_q - \mathbf{k}_j\right)$, between any two of the beam wave vectors. The location of these Fourier components is shown in Figure 1.7b. The convolution of this interference pattern, rotated through the stripe angles shown in Figure 1.6b, yields the extended observable region shown in Figure 1.7c. The projection of the extended observable region for one of these stripe angles onto the $k_x k_z$ plane is shown in Figure 1.7d. The addition of the Fourier component off the k_x axis has the effect of filling in the missing cone. From this plot it may appear that there are now two missing cones above and below the off-k_x-axis components. However, as Figure 1.7c shows, since these Fourier components are closer together than the on-axis components, much of these missing cones is filled out by the rotation of the interference pattern through several stripe angles. Taken together, the extension of the observable region yields a super-resolution image with a near isotropic resolution doubling compared to a diffraction limited system[59].

As previously mentioned, SIM is the most widely accepted super-resolution technique for biology for a number of reasons. The number of images required in order to reconstruct a super-resolution SIM image are determined by the number of lateral Fourier components in the illumination pattern - 3 for 2D SIM and 5 for 3D SIM - and the number of stripe angles used to rotate the illumination pattern through - typically 3. Therefore, only 9 or 15 images are required to reconstruct a 2D or 3D super-resolution SIM image respectively. This has a number of benefits. Firstly, the temporal resolution is considerably higher for SIM than for point-scanning super-resolution techniques, such as STED, or SMLM techniques which require a great deal more images per reconstruction[45, 51]. Secondly, each of these images is fundamentally still a widefield-style image and therefore

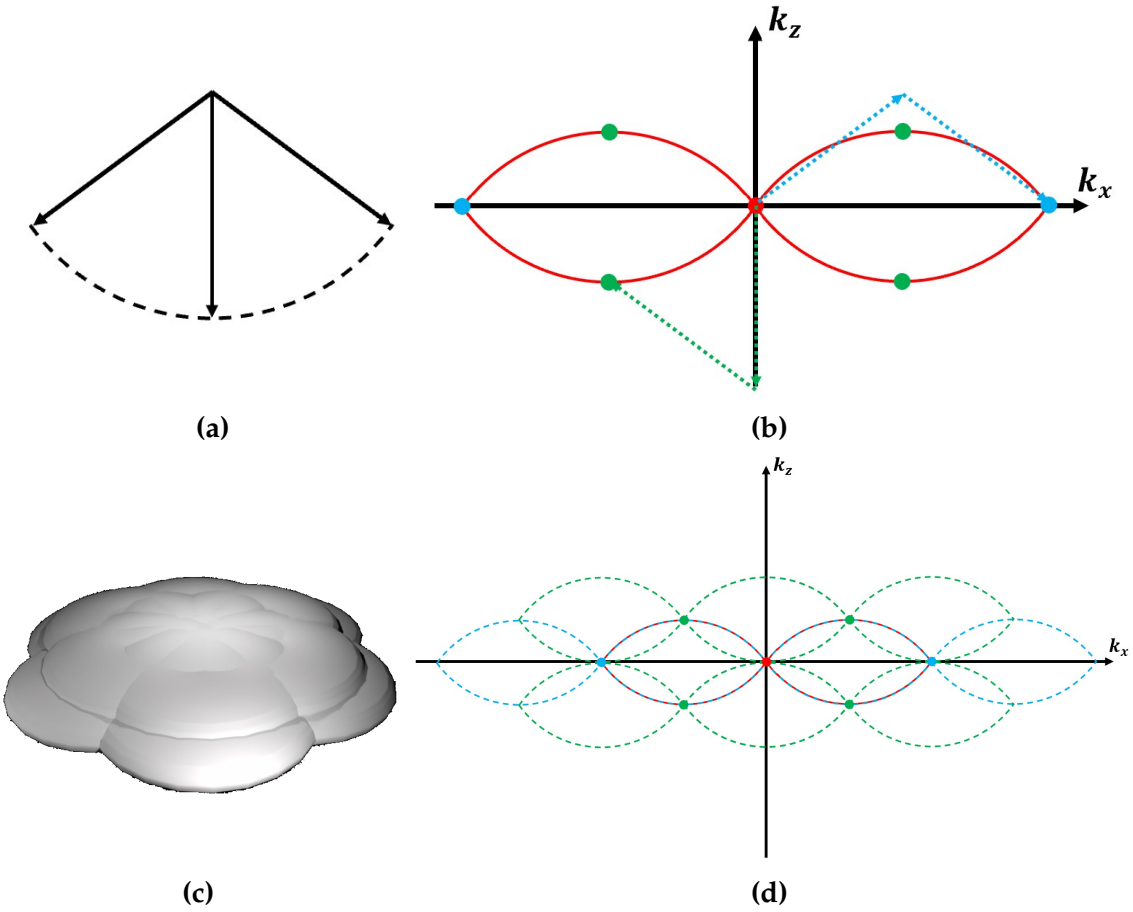


Figure 1.7: *Resolution enhancement with 3D SIM imaging.* ***(a)*** *The amplitude wave vectors corresponding to the 3 illumination beams. All vectors have the same magnitude,* $\frac{1}{\lambda}$ ***(b)*** *The projection of the observable region onto the* $k_x k_z$ *plane with the spatial frequency component locations for three-beam interference patterns shown.* ***(c)*** *The full observable region extension for all three angles in reciprocal space.* ***(d)*** *The projection of the extended observable region for one stripe angle onto the* $k_x k_z$ *plane.*

has a lower light-dosage than per image than STED or SMLM techniques. The lower light-dosage per image combined with fewer total images required per reconstruction contributes to a low photodamage impact. Finally, SIM is easily expandable to multi-colour imaging, even using the same optical setup[61, 62]. Overall, SIM is a super-resolution technique well suited to biological imaging, particularly imaging dynamic biological processes.

1.3 Optical Aberrations

One factor preventing microscopes from achieving the ideal diffraction limited resolution is the presence of optical aberrations[21, 63, 64]. These aberrations describe the deviation of the light wavefront from the ideal Gaussian surface. They have numerous sources, but the most common are those arising from system imperfections - i.e. manufacturing errors in components, placement of lenses off the optical axis, etc - and those arising refractive index variances across the wavefront[65, 66]. In biological samples, these variances arise from sample heterogeneities since different biological structures possess varied refractive indices[67, 68, 69, 70]. These refractive index variances introduce path differences between different sections of the light wavefront. A generalised pupil function (GPF) defined as[71]:

$$P\left(\mathbf{r}_{xy}\right) = A\left(\mathbf{r}_{xy}\right) e^{i\Phi\left(\mathbf{r}_{xy}\right)}, \tag{1.23}$$

is a complex-valued function. Defining the GPF on the normalised system pupil, with $\rho = [0, 1]$ and $\theta = [0, 2\pi]$, and assuming the pupil is circular simplifies the following analysis and is generally more intuitive. In such a system, the GPF has the form:

$$P\left(\rho, \theta\right) = A\left(\rho, \theta\right) e^{i\Phi(\rho,\theta)}. \tag{1.24}$$

The real-valued function $A\left(\rho, \theta\right)$ accounts for amplitude variations and the real-valued function $\Phi\left(\rho, \theta\right)$ accounts for the phase variations. Revisiting the simplified optical system in Figure 1.2, assuming a point source a **O** and that the exit pupil of the system is the unit disk, the field intensity at the $x'y'$ plane is proportional to[21, 22]:

$$\mathcal{I}(v, \phi) = \frac{1}{\pi} \left| \int_0^1 \int_0^{2\pi} P\left(\rho, \theta\right) e^{iv\rho\cos(\theta-\phi)} \rho d\rho d\theta \right|^2. \tag{1.25}$$

For an aberration free system, $A(\rho,\theta) = 1$ and $\Phi(\rho,\theta) = 0$ which makes the integral in Equation 1.25 analytically computable. From this it is possible to recover $\mathcal{I}(v,\phi) = \mathcal{I}_w(v)$ from Equation 1.1.

1.3.1 Zernike Polynomials

Whilst the phase distortions can be treated in their native form, it is useful for a number of reasons to represent them as an expansion in orthogonal functions, and Zernike polynomials are typically chosen for this expansion[72, 73, 74]. Zernike modes are not suitable to represent phase distortions arising from all sources, such as air turbulence or fabrication errors in the single-point diamond turning process[63]. However, the sources of phase distortions for which a Zernike representation is not appropriate, such as phase distortions with discontinuities, do not generally arise in a biological context. Additionally, Zernike modes are not sufficient to represent the phase distortions arising in certain imaging configurations, such as in high NA or 4π imaging systems[75, 76, 77]. These types of systems are not the focus of the work presented in this thesis, and they are not the most common types of imaging systems. This complication is therefore not considered in this work. Nonetheless, it is worth noting that there do exist imaging modalities which are useful for biological imaging for which using Zernike modes is not appropriate.

The Zernike modes have a number of useful mathematical properties, and low order Zernike modes correspond to well-known optical aberrations e.g. defocus, astigmatism, coma, spherical aberration[22, 66, 72, 78]. Using the Zernike polynomials, the phase distortions, $\Phi(\rho,\theta)$ can be written as:

$$\Phi(\rho,\theta) = \sum_{n,m} \alpha_n^m \mathcal{Z}_n^m(\rho,\theta), \tag{1.26}$$

where indices $n \in \mathbb{N}_0$ and $m \in \mathbb{Z}$ denote the radial order and azimuthal frequency respectively of the Zernike polynomial, $\mathcal{Z}_n^m$, and are such that $n - |m| \geq 0$ and even. The coefficients of each Zernike polynomial are represented by $\alpha_n^m \in \mathbb{R}$. Each Zernike polynomial is the product of a radial polynomial, $R_n^m(\rho)$, and an azimuthal polynomial, $\Theta_n^m(\theta)$:

$$\mathcal{Z}_n^m(\rho,\theta) = c_n^m R_n^m(\rho)\Theta_n^m(\theta), \tag{1.27}$$

where c_n^m, $R_n^m(\rho)$, and $\Theta_n^m(\theta)$ have the following definitions:

$$c_n^m = \begin{cases} \sqrt{n+1} & m = 0 \\ \sqrt{2(n+1)} & m \neq 0 \end{cases}, \tag{1.28}$$

$$R_n^m(\rho) = \sum_{s=0}^{\frac{n-m}{2}} \frac{(-1)^s (n-s)!}{s!\left(\frac{n+m}{2}-s\right)!\left(\frac{n-m}{2}-s\right)!} \rho^{n-2s}, \tag{1.29}$$

$$\Theta_n^m(\theta) = \begin{cases} \cos(m\theta) & m \geq 0 \\ -\sin(m\theta) & m < 0 \end{cases}. \tag{1.30}$$

This formulation of Zernike modes is normalised in that the RMS phase variation across the pupil is 1 for each mode. Throughout this thesis the Noll index ordering convention is used[73]. Appendix A describes this ordering convention and contains the algebraic expansion for the Zernike polynomials up to radial order $n = 7$. Other modal bases and ordering conventions do exist[79, 80, 81, 82].

It is useful to be able to compare phase distortions to one another to measure their severity. In order to do so, scalar indicators are required. Typically, the root mean squared (rms) and variance of $\Phi(\rho, \theta)$ are used:

$$rms(\Phi) = \left(E_2[\Phi]\right)^{\frac{1}{2}} \qquad var(\Phi) = E_2[\Phi] - \left(E_1[\Phi]\right)^2, \tag{1.31}$$

where $E_k[\Phi]$ are the functionals[71, 74]:

$$E_k[\Phi] = \frac{1}{\pi} \int_0^1 \int_0^{2\pi} \Phi(\rho, \theta)^k \rho d\rho d\theta. \tag{1.32}$$

Using the normalisation factors, c_n^m, and the orthogonality properties of the Zernike modes, it is apparent that $E_1[\Phi] = \alpha_0^0$ and $E_2[\Phi] = \sum_{n,m} (\alpha_n^m)^2$. Substituting these values back into Equations 1.31 yields:

$$rms(\Phi) = \left(\sum_{n,m} (\alpha_n^m)^2\right)^{\frac{1}{2}} \qquad var(\Phi) = \sum_{n\neq 0, m\neq 0} (\alpha_n^m)^2, \tag{1.33}$$

Since $\mathcal{Z}_0^0$ - i.e. piston - does not affect image formation, often its corresponding amplitude α_0^0 is simply not included. In this case, $rms(\Phi) = \sqrt{var(\Phi)}$

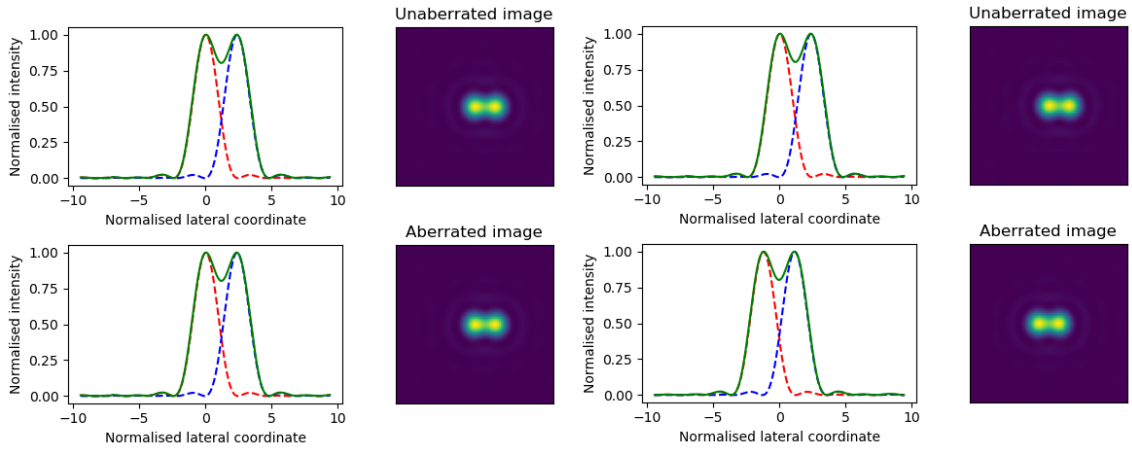
1.3.2 Aberrations and Resolution

Not all Zernike modes affect the resolution of the system. Figures 1.8a- 1.8c show the effect of the first 3 Zernike modes, $\mathcal{Z}_0^0$, $\mathcal{Z}_1^{-1}$, and $\mathcal{Z}_1^1$ - i.e. piston, tip and tilt - on two point objects separated by the diffraction limit determined by the Rayleigh criterion, r_l. Clearly piston has no effect on the image intensity or resolving power. Additionally, assuming an incoherent, shift invariant imaging system, the only effect of the tip and tilt aberrations is a lateral shift in the x and y axis respectively. The overall image intensity and resolving power remains unaffected. For this reason piston (and often tip and tilt) are considered "non-optical" aberrations. Figure 1.8d shows the same two point objects aberrated with a phase deformation of $rms(\Phi) = 1$ composed of a number of Zernike modes of varying amplitudes. The image intensity is severely degraded and the resolving power is significantly less than the diffraction limited case. Evidently, the presence of phase distortions is a limiting factor to imaging systems from achieving the ideal diffraction limited resolution[71, 83].

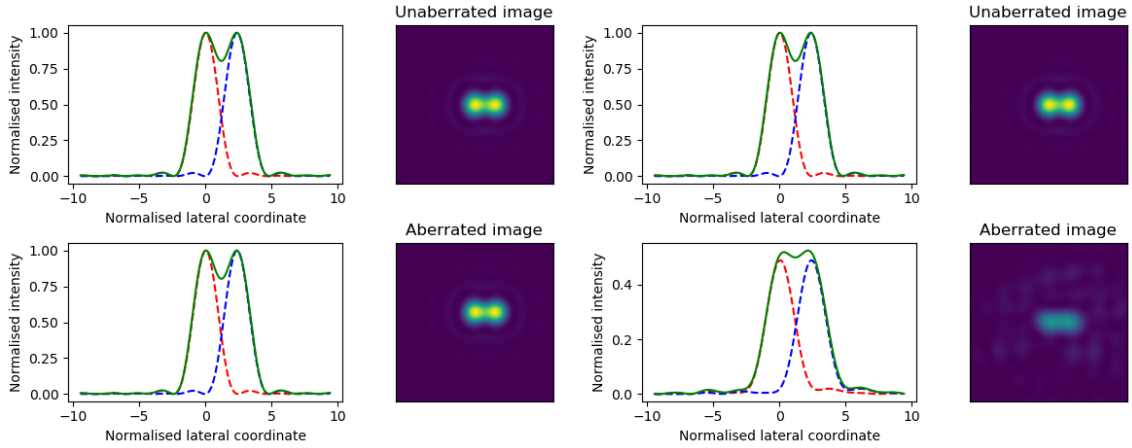
1.4 Adaptive Optics

As previously mentioned, phase aberrations arise in microscopy primarily due to heterogeneities in the structure of the biological sample being imaged. Consider the objective lens of a microscope, in the absence of optical aberrations, as in Figure 1.9a, a flat wavefront propagating through a linear medium is focused to a single diffraction limited spot. Introducing a heterogeneous - but still linear - media distorts the phase wavefront and leads to an extended, non-diffraction limited focal spot as seen in Figure 1.9b. However, if, as in Figure 1.9c, the wavefront is not flat when it enters the microscope objective but instead shaped to compensate for the phase distortion then an ideal, diffraction limited focal spot is recovered. Since the phase distortions encountered are not only sample dependent, but spatially and (for live samples) temporally dependent an adaptive method for pre-shaping the optical wavefront is required[76, 84, 85]. The branch of technologies and methods for doing this is referred to as adaptive optics (AO).

Similar to how the telescope and microscope have a shared historical origin, the concept of using AO to correct for optical aberrations has it is origin in correcting for phase distortions in astronomical telescopes[86]. The principle of an AO system for microscopy is shown in Figure 1.10. Here, only the emission path is considered.



(a) $rms(\Phi) = 1, \alpha_0^0 = 1$ **(b)** $rms(\Phi) = 1, \alpha_1^{-1} = 1$



(c) $rms(\Phi) = 1, \alpha_1^1 = 1$ **(d)** $rms(\Phi) = 1$

Figure 1.8: *A visualisation of the effect of optical aberrations on image resolution* ***(a)-(c)*** *Ideal diffraction limited point sources at separation r_l aberrated with $rms(\Phi) = 1$ of purely piston, tip, and tilt respectively.* ***(d)*** *Ideal diffraction limited point sources at separation r_l aberrated with a random phase distortion with $rms(\Phi) = 1$. These figures were generated using the code presented in Appendix B.2*

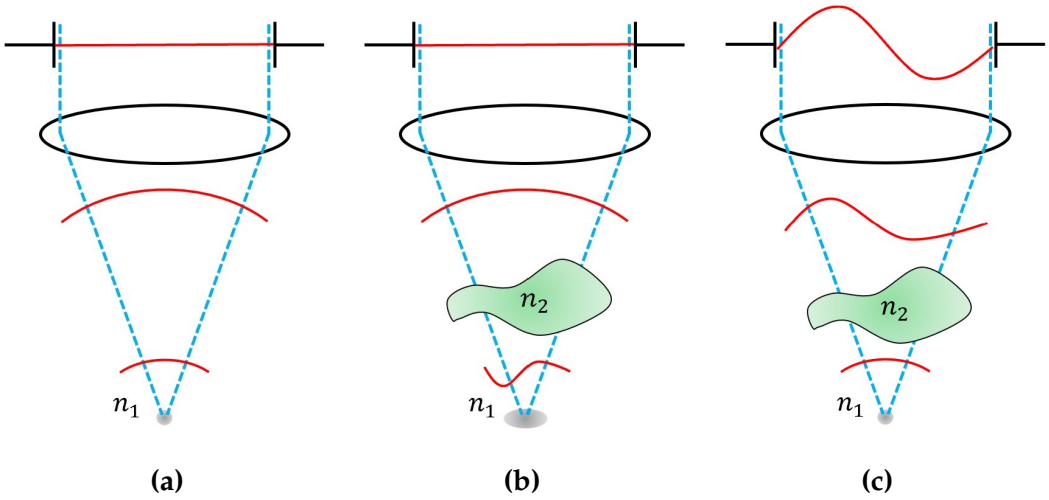


Figure 1.9: *Illustration of aberrations affecting a microscope objective focus.* ***(a)*** *The media between the microscope objective and the sample has a homogeneous refractive index, n_1 and the microscope objective forms a diffraction limited focal spot.* ***(b)*** *The media the wavefront passes through is heterogeneous. This causes a phase distortion in the wavefront and leads to an expanded focal spot.* ***(c)*** *Prior to the objective aperture, the wavefront is pre-shaped to the opposite shape to the expected distortion. Once the wavefront passes though the heterogeneous media, an ideal wavefront is recovered and thus the focal spot is diffraction limited again.*

A distorted wavefront Φ_I, arrives at the aperture of the microscope. The wavefront is then imaged onto an adaptive element capable of applying a variable phase distortion, Φ_{AO}. Once the wavefront has interacted with the adaptive element, there is a residual phase aberration $\Phi_R = \Phi_I - \Phi_{AO}$. Figure 1.10 has the wavefront passing through a beamsplitter and both being focused onto an imaging device and being directed to a wavefront sensor. In the latter case, Φ_R is calculated directly while in the former case Φ_R is inferred through some indirect measurement. Typically only one of these options is employed. The calculation of Φ_R is then passed to a controller which adjusts Φ_{AO} in order to minimise some measure of error such as $rms(\Phi_R)$. Figure 1.10 assumes a reflective adaptive element such as a deformable mirror (DM) or a spatial light modulator (SLM), but the principles also apply for a transmissive adaptive element placed in the beam path, such as an opto-acoustic lens.

Implementing AO in microscopy has already been shown to be highly effective at reducing optical aberrations and yielding significant improvements to image quality[83, 85, 87, 88, 89]. Designing an AO enabled system follows a predicable workflow outlined in Figure 1.11 consisting of four phases:

1. *System Design Phase*: A potential user should consider the needs of their

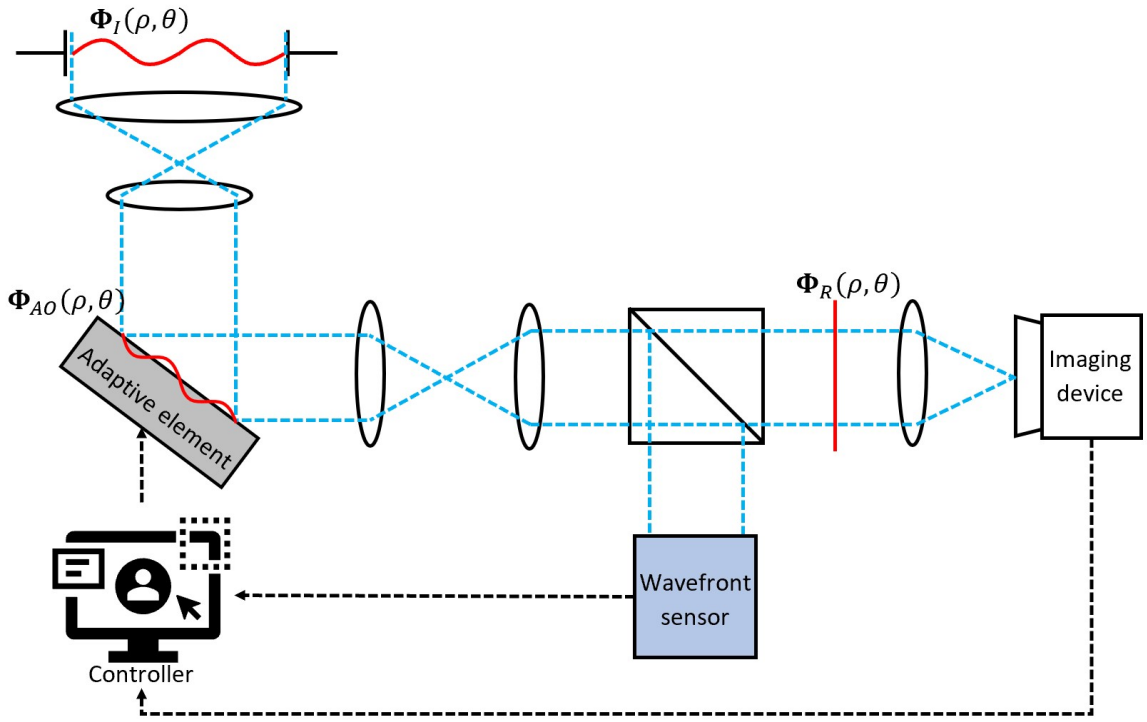


Figure 1.10: *Schematic of the emission path of an adaptive optics system. The emitted wavefront of a point in the fluorescent sample, Φ_I, arrives at the aperture of the microscope. It is reimaged onto the adaptive element. The adaptive element has some phase, Φ_{AO}, on its surface. The light then passes through a beamsplitter and is focused onto an imaging device. The residual phase aberration, $\Phi_R = \Phi_I - \Phi_{AO}$, is either calculated directly by the wavefront sensor or inferred indirectly from the data acquired by the imaging device. This information is passed to a controller which applies a phase aberration to the adaptive element, Φ_{AO}, in order to minimise a metric like $rms(\Phi_R)$.*

imaging modality, system constraints, desired sample types before deciding on the appropriate AO element to implement.

2. *Installation Phase*: The user installs the chosen AO element into their beam path.

3. *Set-up Phase*: The AO element is calibrated to correct for optical aberrations. This calibration is checked and the system aberrations are corrected.

4. *Sample Correction Phase*: The sample correction routine is designed. This will typically fall into one of two categories; sensorless AO or direct wavefront sensing.

However, there are a number of adaptive elements[90], a plethora of direct wavefront sensing techniques[71, 91, 92], and wide array of sensorless correction

methodologies[93, 94, 95, 96, 97]. Considering AO within super-resolution imaging techniques further complicates the situation[98, 99, 100]. Since there is no universally agreed upon AO implementation, each implementation has to go through the entire design process from scratch, creating a bespoke but brittle implementation which is not easily transferable to any other system, imaging modality, sample type, etc.

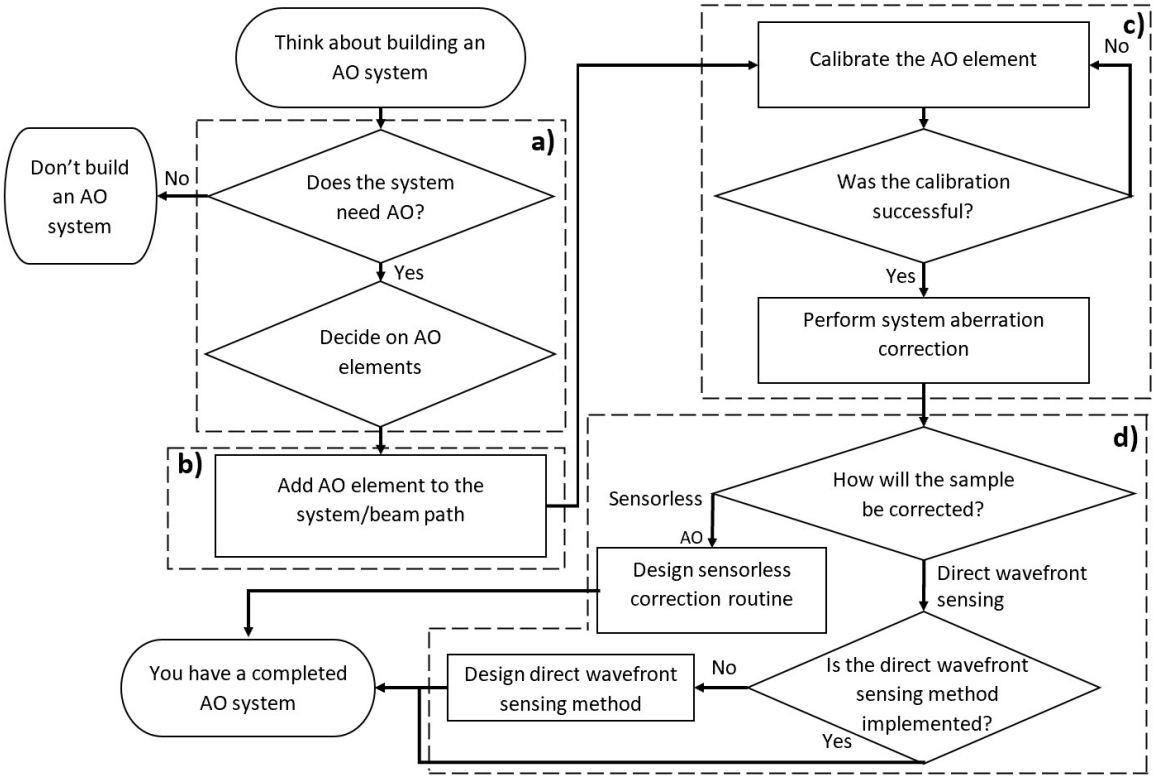


Figure 1.11: *Flowchart depicting the general process for building a system utilising AO.* ***a)*** *System Design Phase. User decides whether the system needs AO and, if so, what type.* ***b)*** *Installation Phase. The chosen AO elements are added to the system.* ***c)*** *Set-up Phase. The chosen AO element is calibrated. Typically, this involves mapping the variable elements of the AO element (e.g. deformable mirror actuators) to a useful set of basis functions which represent optical aberrations.* ***d)*** *Sample Correction Phase. Here the user designs the methods to be used for correcting their desired sample.*

1.5 Overview and Aims of the Thesis

There is a need for a robust, accurate, easy-to-use, general implementation of AO for microscopy[101, 102]. This implementation should be accessible to users in order to ensure its adoption amongst the microscopy community and therefore the widespread adoption of AO technology. This thesis demonstrates just such

an implementation - Microscope-AOtools - deployed successfully on two separate systems. The contributions of the thesis are collected into four chapters and is laid out as follows:

- Chapter 2 discusses the two systems which Microscope-AOtools has been deployed on: Aurox Clarity and DeepSIM. It discusses their optical layout and contains a brief discussion of the optical alignment procedure as well as an alignment tool developed during the course of this thesis; "Hall, Nicholas J., David Miguel Susano Pinto, and Ian M. Dobbie. "BeamDelta: simple alignment tool for optical systems." *Wellcome Open Research* 4.194 (2019): 194."[103] The hardware control software - Python Microscope[104] - used to synchronise the disparate hardware elements of each microscope setup and the graphical user interface (GUI) software - Microscope-Cockpit[105] - which is used to operate the microscopes are also discussed.
- Chapter 3 corresponds to scientific publication: "Hall, Nicholas, et al. "Microscope-AOtools: A generalised adaptive optics implementation." *Optics Express* 28.20 (2020): 28987-29003."[106] The generalised implementations of all the methods required by the Set-up and Sample Correction phases detailed in Section 1.4 are discussed. It also contains discussion of the integration of Microscope-AOtools with Microscope-Cockpit in order to enable accessibility for users.
- Chapter 4 corresponds to the scientific publication: "Hussain, Syed Asad, et al. "Wavefront-sensorless adaptive optics with a laser-free spinning disk confocal microscope." *Journal of Microscopy* (2020)." on which the author is a co-first author[107]. It details the successful implementation of Microscope-AOtools on the Aurox Clarity system.
- Chapter 5 details the successful implementation of Microscope-AOtools on the DeepSIM system. The results and implementation presented here will contribute significantly to a future publication of the DeepSIM system.

Discussions of existing limitations and areas for further development to the presented AO implementation are presented in Chapter 6. Conclusions are drawn in Chapter 7. The Aurox Clarity system was built by Dr Syed Hussain of the Dynamic Optics and Photonics Group, University of Oxford and Mr Toshiki Kubo of the Department of Applied Physics, Osaka University. The design and original implementation of the DeepSIM system was built by Dr Ian Dobbie, Dr Mick Philips, Dr Antonia Göhler and Dr Mantas Žurauskas, all members of the

Micron Advanced Imaging Consortium at the time. The author implemented a number of modifications, improvements, and realignments in order to produce the demonstrations shown in this thesis.

Chapter 2

Systems and Implementations

2.1 Aurox Clarity System

Confocal laser scanning microscopy (CLSM) is, traditionally, a point-scanning microscopy technique pioneered with the objective of discarding the scattered illumination light and the out-of-focus excited fluorescence when imaging biological samples[43]. Discarding the out-of-focus light yields images with high contrast and good optical sectioning[108]. The original Minsky design struggled with a low-frame rate. Advances in technology have led to improved scanning speeds and therefore improved image frame rates which, for modern CLSM set-ups, is generally on the order of milliseconds per 2D frame[44, 109]. For many dynamic biological processes this is still insufficient, which lead to the development of (among other things) the Nipkow-Petran spinning disk setup which allows for video rate confocal imaging[110, 111, 112]. Hence, spinning disk confocal microscopes are frequently used for imaging live biological processes.

The Nipkow-Petran design does have disadvantage in that it discards $\sim 99\%$ of both excitation and emission light in order to achieve good optical sectioning and xy-resolution[113]. This can lead to poor signal-to-noise ratio (SNR) in fluorescence imaging if sufficiently strong fluorophores aren't used[114]. This disadvantage is somewhat mitigated - but not entirely overcome - in systems employing microlens arrays such as the Yokogawa systems[115]. Another design exists called a Correlation Disk which uses light emitting diodes (LEDs) as the illumination light source in conjunction with a patterned disk which is placed in a location shared by both the excitation and emission beam paths[116, 117, 118]. The Aurox Clarity module employs just such an approach to achieve real-time confocal imaging with a significantly increased light budget (only $50\% - 75\%$ of the emitted light is discarded compared the typical $\sim 99\%$). This approach relies on good

correlation between the grid patterns present in both the excitation and emission paths, which is degraded by optical aberrations[107]. Therefore, the Aurox Clarity System incorporates both the Aurox Clarity module for fast, laser-free confocal imaging and a deformable mirror (DM) for aberration correction.

2.1.1 Aurox Clarity System Optical Set-up

Figure 2.1a shows the complete optical schematic of the Aurox Clarity system. Its base is an iX71 Olympus microscope body with a AMEP4694 60×, 1.42 NA oil objective and P-736.ZR1S PI-nano Z Microscope Scanner piezo Z-stage. Ordinarily, the Clarity module would be attached to the side port of the microscope body. The Mirao52e, a 52-actuator DM, must be placed in a plane conjugate to the back pupil plane in order to correct for the aberrations. To achieve this, the Clarity module was separated from the main microscopy body by a 4f, unity magnification telescope. The 4f telescope re-images the image plane close to the side port onto input port of the Clarity module and the DM was placed at the intermediate pupil plane. The Mirao52e DM was calibrated using a separate set-up not shown which uses a technique based on deflectometry[91, 119]. A Photometrics PrimeBSI camera was attached to the Camera port of the Aurox Clarity module. A pE-300 Ultra CoolLED was attached to the Illumination light input port.

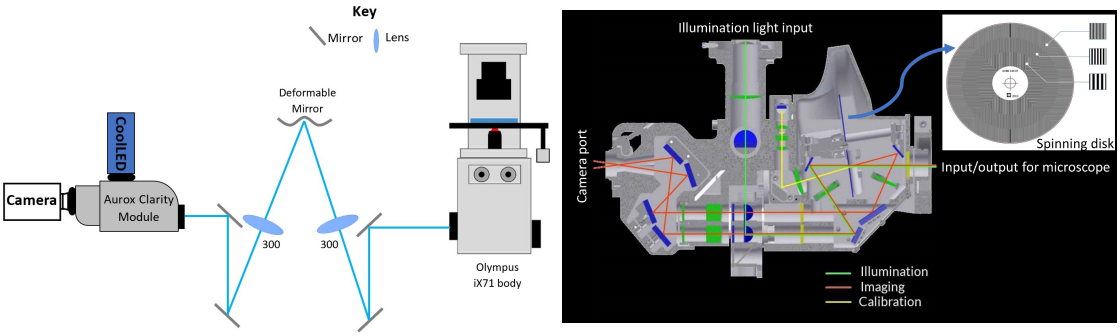


Figure 2.1: *Aurox system beam path layout* ***(a)*** *The complete imaging beam path for the Aurox Clarity System. The excitation and emission beam paths are identical up to the Aurox Clarity module* ***(b)*** *The internal beam paths for the Aurox Clarity module (Modified with permission from Aurox Ltd., Copyright Aurox Ltd.)*

The excitation and emission beam paths are identical from the input/output microscope port to the focal plane of the objective. The differing beam paths for the excitation and emission light within the Clarity module are shown in Figure 2.1b.

The excitation light impinges on the spinning disk and is either transmitted by the disk or discarded. The emission light impinges on the spinning disk in the opposite direction. The emission light from the focal plane of the objective is transmitted by the disk and is directed to one half of the PrimeBSI camera chip. The rest of the emission light is reflected off the disk and directed to the opposite half of the PrimeBSI camera chip. The Calibration light source generated within the Clarity module is used to align the two halves of the PrimeBSI camera chip to one another. A set of dichroic filter cubes are used to select both the excitation and emission wavelengths. There are four available dichroic filter cubes which can be selected:

1. Dichroic filter 1: Excitation 466nm/FWHM 40nm, Emission 525nm /FWHM 45nm
2. Dichroic filter 2: Excitation 554nm /FWHM 23nm, Emission 609nm /FWHM 54nm
3. Dichroic filter 3: Excitation 578nm /FWHM 21nm, Emission 641nm /FWHM 75nm
4. Dichroic filter 4: Excitation 392nm /FWHM 23nm, Emission 447nm /FWHM 60nm

The Aurox Clarity system was built by Dr Syed Hussain and Mr Toshiki Kubo. The innovation which this thesis presents is the successful implementation of Microscope-AOtools to provide control of the deformable mirror and therefore system and sample aberration correction which enabled high-quality imaging at depth.

2.1.2 Image Formation in Aurox Clarity Module

Figure 2.2 shows a simplified schematic for a Nipkow-Petran spinning disk confocal microscope. The excitation illumination passes through an aperture mask, which is then imaged onto the sample. This aperture mask consists of a number of pinholes packed closely together, illuminating a number of focal spots at once. The excitation light then passes back through the aperture mask where the out-of-focus light is discarded by the pinhole array[110, 111].

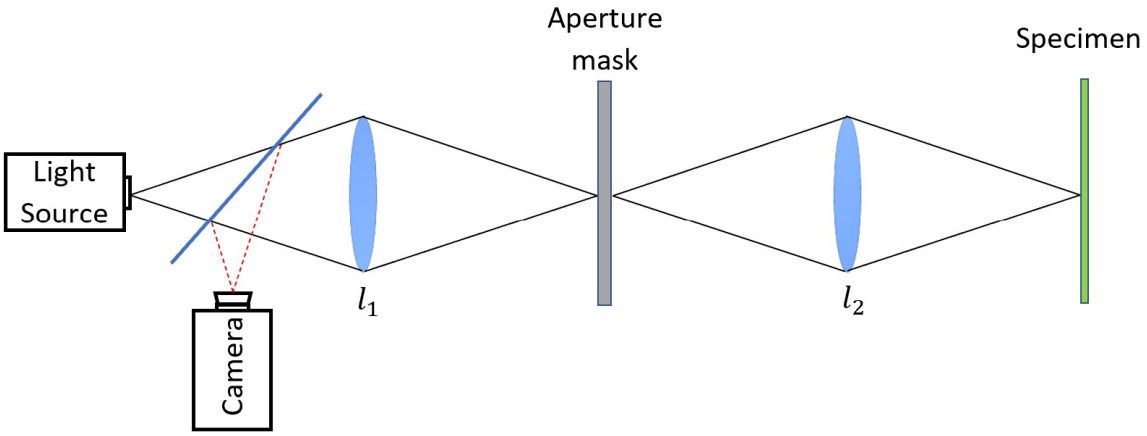


Figure 2.2: *A schematic diagram showing a simplified layout for a Nipkow-Petran spinning disk confocal microscope*

Consider a transmissive optical system as shown in Figure 2.3. For an incoherent light source, immediately after the detector mask the intensity, $I(\mathbf{x}_2)$, is given by:

$$I(\mathbf{x}_2) = \int S(\mathbf{x}_1) D(\mathbf{x}_2) \left| \int h_1\left(\mathbf{x}_0 + \frac{\mathbf{x}_1}{M}\right) \tau(\mathbf{x}_0) h_2\left(\mathbf{x}_0 + \frac{\mathbf{x}_2}{M}\right) d\mathbf{x}_0 \right|^2 d\mathbf{x}_1, \qquad (2.1)$$

where $S(\mathbf{x}_1)$ is the intensity sensitivity of the source mask, $D(\mathbf{x}_2)$ is the detector mask, $\tau(\mathbf{x}_0)$ is the amplitude transmittance function of the aperture mask, h_1 and h_2 are the amplitude point spread functions (PSFs) of the two imaging lenses respectively, and M is the magnification factor.

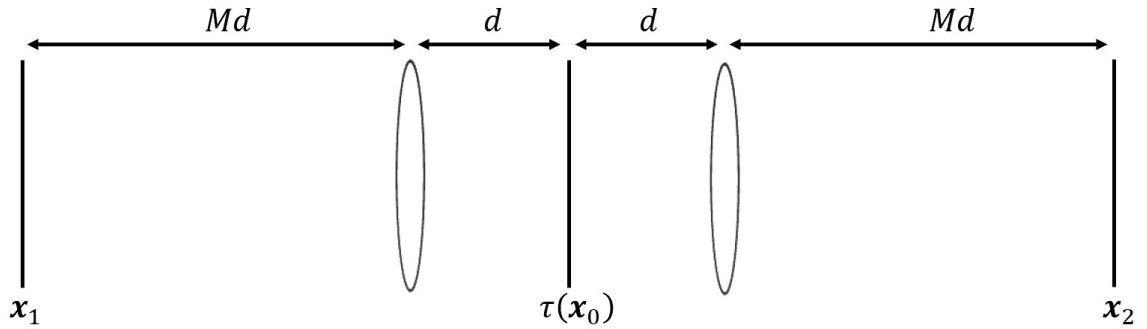


Figure 2.3: *A simple schematic diagram of a transmissive optical system. An aperture mask with amplitude transmittance, $\tau(\boldsymbol{x})$, is placed at $\boldsymbol{x}_0$. A source with intensity sensitivity described by $S(\boldsymbol{x})$ is placed at x_1. A detector with a mask profile described by $D(\boldsymbol{x})$ is placed at $\boldsymbol{x}_2$. $\boldsymbol{x}_1$ and $\boldsymbol{x}_2$ are conjugate planes.*

Consider the case of reflection just after the detector mask and with the detector aperture positioned at some $\mathbf{x}_i$ such that $S(\mathbf{x}) = D(\mathbf{x}) = \delta(\mathbf{x} - \mathbf{x}_i)$, where here δ

denotes the Dirac delta function. In this case, assuming an ideal point source, the intensity at $\mathbf{x}_i$ from Equation 2.1 becomes:

$$I(\mathbf{x}_i) = \left| \int h_1(\mathbf{x})\, h_2(\mathbf{x})\, \tau\left(\mathbf{x} - \frac{\mathbf{x}_i}{M}\right) d\mathbf{x} \right|^2, \tag{2.2}$$

which is the equation which describes image formation in conventional confocal microscopes[120]. This describes the image formation from a single point source and hence requires scanning in $\mathbf{x}_i$ to form a complete image of the field of view of the object. To remove the need for scanning, the source and detector masks should instead be composed of an array of pixels with variable transmittance where each pixel's transmittance is time dependent, $b_i(t)$. The source and detector masks can then be described by:

$$S(\mathbf{x}) = D(\mathbf{x}) = \sum_{i=0}^{N} b_i(t)\, \delta(\mathbf{x} - \mathbf{x}_i) \tag{2.3}$$

Where N is the number of pixels and each pixel has a coordinate $\mathbf{x}_1, \mathbf{x}_2, ..., \mathbf{x}_N$. The resultant image is given by the time average of Equation 2.1:

$$\langle I(\mathbf{x}_2) \rangle = \left\langle \int S(\mathbf{x}_1)\, D(\mathbf{x}_2) \left| \int h_1\left(\mathbf{x}_0 + \frac{\mathbf{x}_1}{M}\right) \tau(\mathbf{x}_0)\, h_2\left(\mathbf{x}_0 + \frac{\mathbf{x}_2}{M}\right) d\mathbf{x}_0 \right|^2 d\mathbf{x}_1 \right\rangle, \tag{2.4}$$

where $\langle . \rangle$ is the time average. Since the only time-dependent components are $S(\mathbf{x}_1)$ and $D(\mathbf{x}_2)$ only the time average of $S(\mathbf{x}_1)\, D(\mathbf{x}_2)$ need be considered:

$$\langle S(\mathbf{x}_1)\, D(\mathbf{x}_2) \rangle = \sum_{i=0}^{N} \sum_{j=0}^{N} \langle b_i(t)\, b_j(t) \rangle\, \delta(\mathbf{x}_1 - \mathbf{x}_i)\, \delta(\mathbf{x}_2 - \mathbf{x}_j). \tag{2.5}$$

The transmittance of each pixel should be entirely uncorrelated with the transmittance of any other pixel. Therefore, a sequence of transmittances is chosen such that:

$$\langle b_i(t)\, b_j(t) \rangle = \delta_{ij}, \tag{2.6}$$

where δ_{ij} is the Kronecker delta. $b_i(t)$ can therefore be any orthonormal sequence, such as an infinite, random sequence of ± 1 or finite-length complementary Golay sequence[121]. Unfortunately, such sequences require negative transmittance values which is not optically achievable. By adding a DC shift this limitation can be overcome and the pixel transmissivities become:

$$S(\mathbf{x}) = D(\mathbf{x}) = \frac{1}{2}\sum_{i=0}^{N}\left[b_i(t)+1\right]\delta(\mathbf{x}-\mathbf{x}_i). \tag{2.7}$$

So, the pixel transmissivities, $\frac{1}{2}\left[1+b_i(t)\right]$, alternate between 0 and 1 as $b_i(t)$ varies between ± 1. Imposing the additional requirement that $\langle b_i(t)\rangle = 0$, then Equation 2.5 becomes:

$$\begin{aligned}\langle S(\mathbf{x}_1) D(\mathbf{x}_2)\rangle &= \frac{1}{4}\sum_{i=0}^{N}\sum_{j=0}^{N}\left\langle\left[b_i(t)+1\right]\left[b_j(t)+1\right]\right\rangle\delta(\mathbf{x}_1-\mathbf{x}_i)\,\delta\left(\mathbf{x}_2-\mathbf{x}_j\right)\\ &= \frac{1}{4}\left[\sum_{i=0}^{N}\delta(\mathbf{x}_1-\mathbf{x}_i)\,\delta(\mathbf{x}_2-\mathbf{x}_i)+\sum_{i=0}^{N}\sum_{j=0}^{N}\delta(\mathbf{x}_1-\mathbf{x}_i)\,\delta\left(\mathbf{x}_2-\mathbf{x}_j\right)\right].\end{aligned} \tag{2.8}$$

Substituting Equation 2.8 into Equation 2.4 yields two terms. The first term is the same form as Equation 2.2 i.e. a conventional confocal image. The second term is a non-confocal image where all the pixel transmissivities are the same. At the limit, where all pixels are adjacent and there is no space in between them, then $S(\mathbf{x}) = D(\mathbf{x}) = \Sigma_{i=1}^{N}\delta(\mathbf{x}-\mathbf{x}_i) = 1$ i.e. a purely conventional image[116, 117]. Therefore, the image formed by the transmitted light, I_T, is a composite of a conventional and confocal image:

$$I_T = I_{conf} + I_{conv}, \tag{2.9}$$

where I_{conf} and I_{conv} are the confocal and conventional images respectively. Instead of an array of pixels with programmable transmissivity, the Aurox Clarity module implements a disk with a photolithographed transmittance sequence. In this case, the transmittance pattern presented to a given fixed pixel is equivalent to the transmittance pattern along the corresponding arc of the disk[117]. Equation 2.7 should therefore be modified to:

$$S(\mathbf{x}) = D(\mathbf{x}) = \frac{1}{2}\sum_{i=0}^{N}\left[b_i(\mathbf{x}_r)+1\right]\delta(\mathbf{x}-\mathbf{x}_i), \tag{2.10}$$

where $\mathbf{x}_r$ is the rotation coordinate. In this case, the final image is obtained by averaging over $\mathbf{x}_r$ rather than over time, but the result is still Equation 2.9. Previous implementations of this approach acquired two images, the second of which had $b_i(\mathbf{x}_r) = 1$ i.e. no aperture mask. As Figure 2.1b shows, the Aurox clarity module images both the light transmitted through the spinning disk and the light reflected

off the disk where the transmissivity is 0. In this case, the detector mask is defined as:

$$D(\mathbf{x}) = \frac{1}{2}\sum_{i=0}^{N}\left[1 - b_i(\mathbf{x}_r)\right]\delta(\mathbf{x} - \mathbf{x}_i). \tag{2.11}$$

Applying the same average over $\mathbf{x}_r$ as before, the image formed by the reflected light, I_R, is:

$$I_R = I_{conv} - I_{conf}. \tag{2.12}$$

Therefore, both the confocal and conventional images can be recovered by:

$$I_{conf} = \frac{1}{2}(I_T - I_R), \tag{2.13}$$

$$I_{conv} = \frac{1}{2}(I_T + I_R). \tag{2.14}$$

This has the benefits of only requiring one exposure for the sample to acquire a confocal image and using all of the emitted fluorescence light. The spinning disk in the Clarity module has three different grid patterns with different spacing. The spacing of the grid pattern determines the degree of optical sectioning and so these grid patterns represent low, medium and high optical sectioning[118]. Low sectioning uses the coarsest disk pattern and leads to a thicker optical section (2.5 μm, as specified by the manufacturer); the medium spaced pattern has a slightly smaller section (1.7 μm); the finest spacing corresponds to a thinner optical section (0.9 μm)[107].

2.2 DeepSIM

As discussed in Section 1.2.1, 3D structured illumination microscopy (3D-SIM) is a super-resolution microscopy technique which is well suited to imaging live biological samples due to the relatively few images required to reconstruct a super-resolution image, millisecond temporal resolution, medium energy load, true multi-colour imaging and fast volume acquisition[44, 45, 122]. However, to date this application has not been extensively exploited for all live sample preparations, namely those requiring dissection and bathing, and those requiring dynamic sample manipulation such as electrophysiology experiments. This is for two principle reasons. Firstly, these biological samples have to be suspended in usually

aqueous media to sustain them, which necessitates an upright configuration. To date, no upright 3D-SIM system exists since this configuration is more challenging to achieve and it is only required for specific biological applications. The aqueous nature of the suspension media also precludes the use of oil objectives, reducing the available NA and hence resolution. Secondly, imaging at depths $> 20\mu m$ remains a challenge for traditional 3D-SIM methods due to limited background rejection and optical aberrations degrading the stripe contrast necessary for successful SIM imaging[61]. Aberrations pose a larger issue in live sample imaging compared to fixed sample imaging, not least of all because live samples cannot be cleared of the extraneous biological structures. Therefore, most 3D-SIM imaging has been limited to thin specimens[123]. DeepSIM is a bespoke microscope designed to address these issues. It is an open and flexible upright microscope platform to enable imaging in live samples requiring dynamic manipulation. Incorporating a spatial light modulator (SLM) to generate the structured illumination pattern enables rapid 3D, multi-colour SIM data acquisition. Finally, incorporating adaptive optics allows for SIM imaging at unprecedented depths in live samples, as well as remote focusing which further increases the speed of image acquisition whilst minimising motion artifacts. The DeepSIM optical design inherits elements and insights from both the OMX system[124, 125] and, later, the CryoSIM system[126].

2.2.1 DeepSIM Optical Set-up

Figure 2.4 shows the complete optical schematic of the DeepSIM microscope. There are multiple possible beam paths which can be altered by raising/lowering certain optics and/or pairs of mirrors. The solid green path denotes the primary 3D-SIM excitation path. The laser beams are combined at a single exit port, magnified and then reflected onto SLM at a shallow angle ($< 10^{\circ}$). The SLM acts as a programable phase grating imposing the structure to the illumination pattern required for SIM imaging. The beam is then magnified and reimaged onto the Alpao 69-actuator DM. The SLM and DM are in reciprocal planes to one another. The SLM is placed in a plane conjugate to the imaging plane in order to create the structured illumination pattern as the imaging plane. The DM is placed in a plane conjugate to the pupil plane since, as discussed in Section 1.3, the aberrations present are described by a pupil function. The beam is then demagnified and imaged on the LUMFLN60XW $60\times$ water dipping objective. The emission beam path follows the same path in reverse up until past the DM. At this point the emission beam path is redirected by a dichroic mirror (Chroma Technology ZT405/488/561/640rpc),

magnified and then reimaged onto the Andor iXon Ultra EMCCD cameras. There is a secondary dichroic (Chroma Technology ZT561rdc-xr) which separates the "red" colour channel (562nm-800nm) from the "green" colour channel (390nm-562nm). Since the DM is in both the excitation and emission paths it is able to correct for aberrations in both paths.

Raising the (1) pair of flip mirrors bypasses the SLM and changes the excitation beam path to a widefield configuration. Raising the (2) pair of flip mirrors bypasses the DM. This is a useful configuration when the DM has not yet been calibrated since the neutral position of the DM actuators have a worse flatness profile than that of a plane mirror. Without calibration, the DM surface cannot be flattened and may contribute to the aberrations present in the imaging system. Raising the (3) flip mirror directs the excitation beam path through the 10× air objective. This beam path is used for large field of view (FOV) mapping.

Raising both the (1) pair of flip mirrors and the (4) flip mounted pellicle beamsplitter and lens changes both the excitation and emission beam paths to create an interferometer. Half of the excitation beam is picked off by the 50:50 beamsplitter and directed straight into the Ximea XiQ camera. This is the interferometer reference arm. The sample beam arm proceeds through the regular excitation beam path. Placing a mirror in the focal plane of the 60× objective reflects the beam back through the emission beam path until it is reflected by the pellicle into the Ximea XiQ camera. The interference pattern produce by the two beams can be interrogated to yield an image of the wavefront phase. Since the DM is in the sample arm, varying the shape of the DM surface will change the shape of the phase wavefront. Measuring how the movement of the DM's actuators influences the shape of the phase wavefront allows the DM to be calibrated and subsequently used to correct for aberrations in the optical system or sample.

2.2.2 Optical Alignment

Being a bespoke microscopy system, DeepSIM was assembled from individual components and aligned by hand. This alignment process is critical for ensuring the microscopy system itself introduces the smallest possible aberrations. Aberrations in the imaging system disrupt image formation and degrade image quality[63]. This affects both the excitation and emission paths of any fluorescent microscope. For a SIM microscope such as DeepSIM the most noticeable effect in the excitation path is the degradation of the structured illumination pattern, particularly the

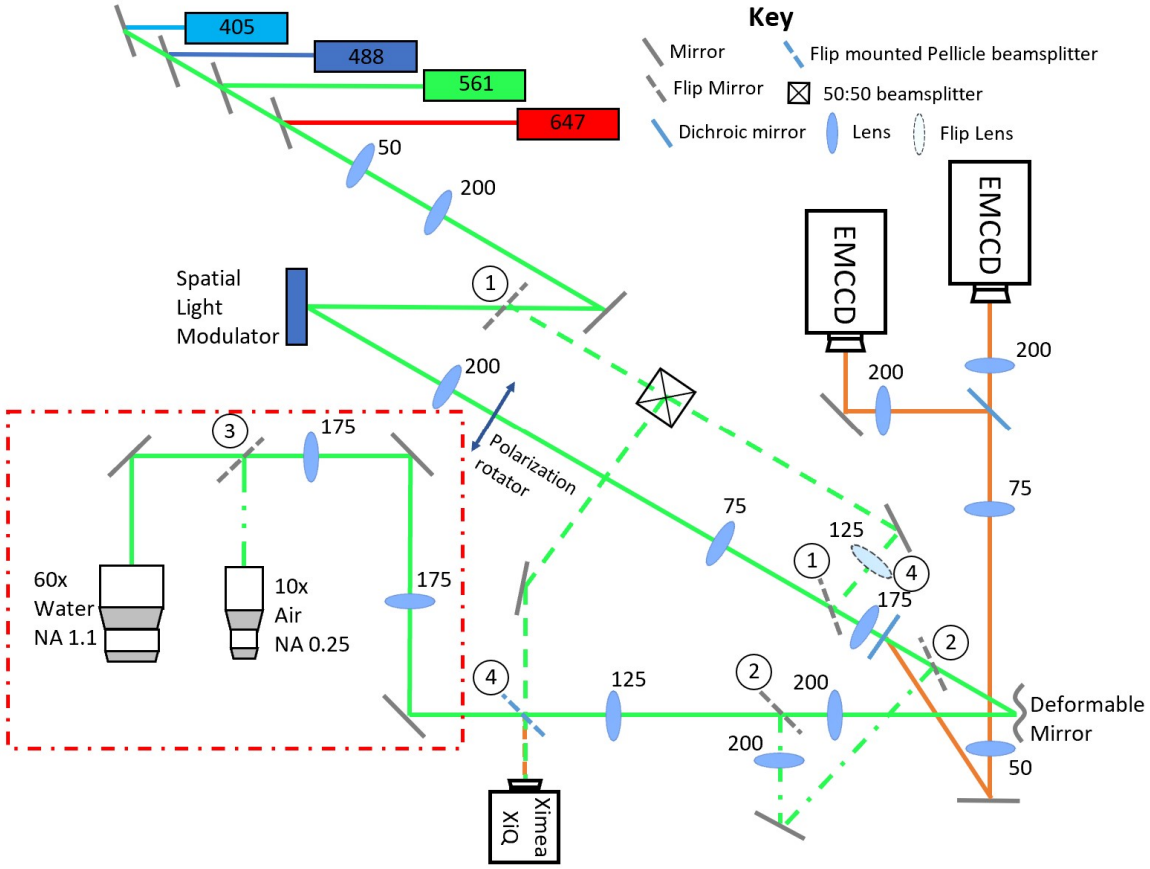


Figure 2.4: *Complete beam path layout for DeepSIM. DeepSIM has multiple paths that can be selected by flipping the numbered pairs/individual mirrors. The green paths denotes the excitation beam paths. The solid green path shows the structured illumination (SI) beam path. The dashed green path shows the widefield beam path. This is changed to the interference beam path by flipping up the lens and pellicle pair. The dot-dashed green path shows the excitation path which bypasses the deformable mirror. The dot-dot-dashed green path shows the excitation path going through the* $10\times$ *air objective for low magnification sample mapping. The orange path denotes the emission beam path. The area denoted by the red dot-dash outline is mounted perpendicular to the optical table.*

high spatial frequency components[98, 99]. In the emission path, these aberrations prevent correct image formation on the camera's sensors. Whilst DeepSIM incorporates a DM for performing aberration correction, every DM has a limited stroke and the actuator response is often non-linear at the limits of this stroke. Correcting for relatively large system aberrations due to a poorly aligned system is likely to lead to insufficient remaining stroke to correct for sample induced aberrations. Therefore, having a well aligned system is still critical even for AO-enabled microscopy systems such as DeepSIM.

Firstly, the upright bridge to hold the objectives and the stage in their upright configuration was constructed and installed on the optical table. One of the lasers was then installed and the beam paths shown in Figure 2.4 was constructed without the lenses. The beam was kept either parallel or perpendicular to the optical table where appropriate and passing through the centre of the objective aperture. The beam was kept parallel to the table by positioning an iris at the beam height of the laser and 'walking' this iris down the beam path, ensuring that after each reflection the beam remains at the same height. Once this beam path was established, the lenses were added sequentially and aligned. Finally, the other lasers were coaligned to this beam path. The result is the complete optical setup shown in Figure 2.5.

The alignment of the lenses and the coalignment of the lasers is typically done by eye. Typically, systems are initially aligned with a small beam and no lenses. Pinholes or irises are placed at critical points in the optical system and then a light beam, usually a laser with a low divergence angle, is aligned to these points. Lenses are then added one at a time. Once a lens is added, propagation of the beam is checked further along the optical path to ensure the beam is passing through the centre of the lens and the lens angle is judged by ensuring the back reflections are centred on the incident beam. This process is repeated for each lens. The quality of the alignment depends upon significant expertise and subjective judgement to both see how well aligned the beam is and to decide when it is sufficiently well aligned to move on to the next element in the system.

This approach has two obvious problems. The first is that the human eye has limited resolving power of approximately 3 to 6 arcseconds [127]. At a distance of 50μm, this is a resolution limit of approximately 10μm. This doesn't account for parallax errors which can further reduce the resolution and introduce systematic errors, nor does is account for the user's ability to accurately judge the comparison between where a laser spot currently is and where it was at some point in the past

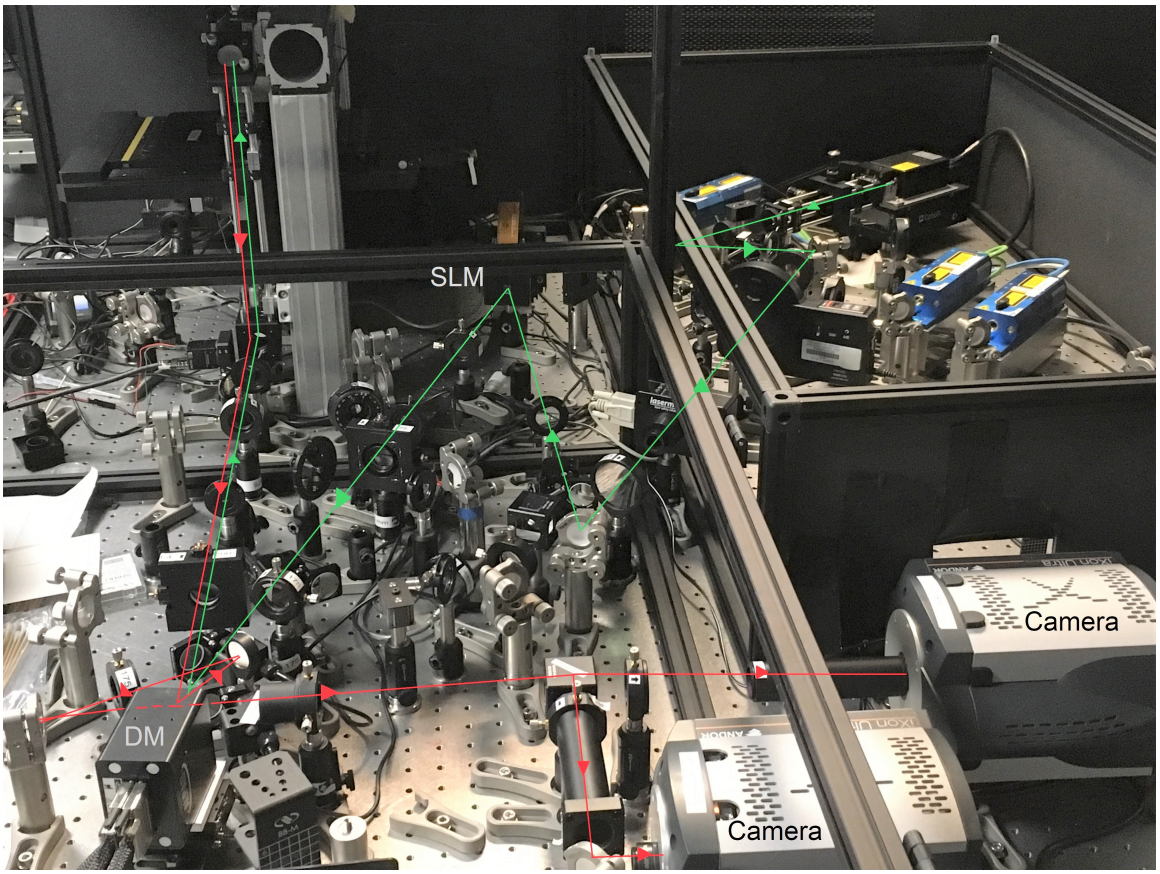


Figure 2.5: *The aligned DeepSIM optical set-up. The 3D-SIM excitation (green) and emission (red) beam paths are annotated.*

[128]. The second problem is that this method of alignment requires users to stare at diffuse laser reflections for extended periods of time which carries an inherent safety risk [129]. Again, this problem can be exacerbated if a user tries to minimise the parallax errors and get level with the optical axis as they then run the risk of accidentally observing collimated laser light or specular reflections.

Errors introduced during alignment contribute optical aberrations even before any heterogeneous sample is imaged. This leads to lower quality imaging in systems without adaptive elements. For systems such as DeepSIM with adaptive elements, these aberrations can be corrected for by the adaptive elements. However, since adaptive elements such as deformable mirrors have a finite stroke length, utilising a portion of these elements corrective capacities correcting for the system aberrations present means less corrective power can be levelled against the aberrations caused by the samples of interest. This is a needless expenditure of corrective power when these system aberrations can be minimised by improving the alignment quality by other means.

BeamDelta is an optical alignment tool designed to address both of the problems with the traditional approach to optical alignment. The laser is imaged directly on two cameras at different positions and the beam centroid positions are calculated for each camera image. These centroid positions can be stored and then subsequent centroid positions - such as those of other lasers which are being coaligned or the original beam after the addition of a lens - can be measured relative to these reference positions. This allows for optical alignment which is several orders of magnitude more accurate and considerably safer than the traditional method of aligning components by eye[103]. It also has the benefit of making the whole process considerably more efficient. DeepSIM required multiple realignments which prior to the development of BeamDelta would take at least a week. With BeamDelta, a complete realignment of the system took only a couple of days.

2.3 Control Software

2.3.1 *Python Microscope*

There is a requirement for control over all the hardware elements of an optical system. This can pose a problem since each hardware component has its own low-level software libraries and the physical hardware is connected to several different computers. Additionally, in order to ensure rapid imaging of 3D widefield and SIM Z-data stacks there is a requirement for precise timing control of the electronic hardware, such as laser, cameras, etc, which must act in concert. To solve these challenges, hardware on both the Aurox Clarity and DeepSIM systems are controlled via Python Microscope, an open source Python package which allows the various elements to be synchronised with hardware triggers.[104] For this, a RedPitaya, a commodity single board computer, is used on each system and functions as a dedicated hardware timing controller.

2.3.2 *Microscope-Cockpit*

Modern complex optical systems require a bespoke graphical user interface (GUI) which is accessible to users. For this purpose, Microscope-Cockpit, a highly flexible and adaptable open source Python-base GUI environment, is utilised for both systems.[105] Figure 2.6 shows the GUI used to control both systems. In the main window, Figure 2.6a, a user can enable and disable the various hardware elements. They can also swap between the various beam paths shown in Figure 2.4. A

user also has access to the automated AO methods, the specifics of which will be discussed later. Figure 2.6c shows the window which can be used to control the XY stage, and the coarse mechanical and fine piezo Z stages as well as display the location of each. The step control and step size for each of these are assigned to keyboard shortcuts.

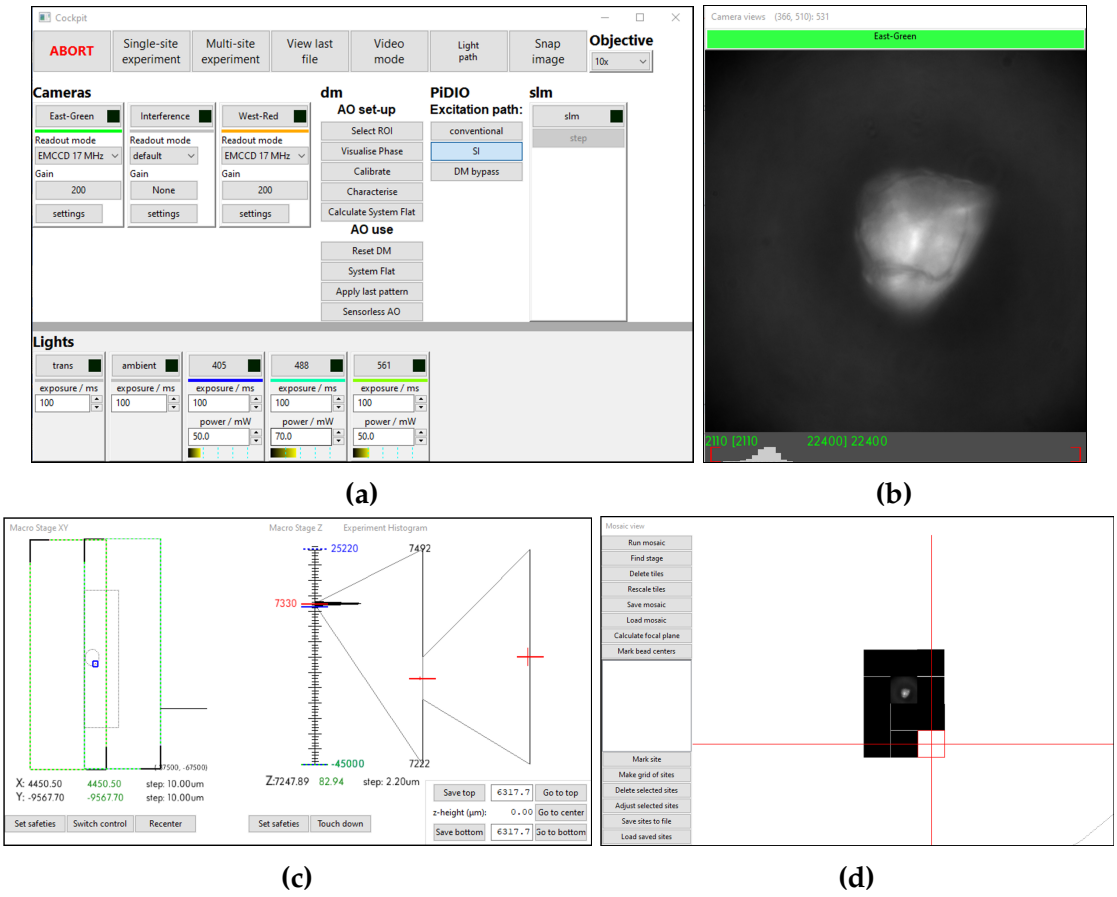


Figure 2.6: *Microscope-Cockpit GUI for controlling DeepSIM* ***(a)*** *Microscope-Cockpit main window. Contains buttons to enable all the hardware, set laser powers and change beam paths* ***(b)*** *Camera view window. Shows the most recent readout from all the enabled cameras* ***(c)*** *Stage control window. Allows the user to control the position of the XY piezo-stage, coarse mechanical Z stage and fine Z piezo-stage* ***(d)*** *Mosaic window. Used by the user to scan the field of view for structures of interest and mark them.*

Unlike most commercial microscopes, DeepSIM does not have any eyepieces. Ordinarily this would present a problem for simply locating the sample, let alone locating a specific region or structure of interest within the sample. To overcome this limitation, Microscope-Cockpit implements a Mosaic window shown in Figure 2.6d. When the mosaic is run, Microscope-Cockpit moves the stage in an anti-clockwise spiral pattern and takes a widefield image at each position.

These images are stored on the main machine's graphics card to enable real-time navigation and site-of-interest marking. Since the images are stored, a user can revisit and investigate areas of the sample which have already been imaged without re-imaging them, decreasing the light exposure and limiting photodamage. The user is able to take an initial mosaic using the 10× objective to find the sample, create a specimen guide map and identify regions of interest. They then swap to the 60× objective and laterally shift the stage to the location of the previous field of view for a more detailed mosaic in the previously identified regions, locate specific sites of interest which they can then mark. The marked sites can then be visited by the user individually and have data collected manually using the "Single-site experiment" option or each site can be visited and data collected in an automated fashion using the "Multi-site experiment" option. In this way DeepSIM can function well without eyepieces and is easily controlled by a potential user.

Although the bulk of the Microscope-Cockpit UI was developed by others, the integration of the adaptive optics functionality for both set-up and use was entirely novel. It was designed to be robust and easy to operate by non-specialist users, primarily the biologists using DeepSIM. A complete exploration of the available functionality appears in Chapter 3.

Chapter 3

Adaptive Optics Control Software

Implementing adaptive optics (AO) in microscopy has already been shown to be highly effective at removing optical aberrations and yielding significantly improvements to image quality[83, 85]. However, AO technology has not been widely adopted due to a number of barriers. Firstly, it is not trivial to set-up an AO element such as the deformable mirrors (DMs) present in the Aurox Clarity system and DeepSIM optical paths. The DM must be calibrated to meaningfully recreate and correct aberrations. Performing this calibration step is not something non-specialist user may know how to do, or how to assess if the process has been successful. Secondly, measuring the wavefront deformations (and therefore the aberrations) present in a sample is complicated. While techniques to directly measure the wavefront do exits, they carry additional complications and are only applicable in certain samples or techniques where sharp foci are present, such as 2-photon microscopy or samples with "guide stars" present[101, 130, 131]. Therefore, indirect wavefront sensing is generally preferred which requires inferring the aberrations present from the variance of a measure of the image quality[102]. This adds an additional complication since there is no universal image quality metric. Indeed, there is unlikely to be a universal image quality metric due to the difference in optics and image formation between imaging modalities, not to mention the whims of individual microscopists and what measure of image quality they deem to be most important for their application. As such, the best metric often varies with sample type and imaging modality[93, 94, 95, 98]. So far, a robust, easy-to-use implementation which incorporates multiple AO methods for multiple sample types/imaging modalities has yet to be presented[101].

Microscope-AOtools provides such an implementation, utilising Python-Microscope to control the physical hardware. Microscope-AOtools has the following Python package dependencies: numpy[132], scipy[133], scikit-image[134], sympy[135],

and AOtools[136]. It incorporates methods for calibrating a DM, evaluating the success of the calibration in recreating aberrations and performing both direct wavefront sensing and sensorless adaptive optics corrections. The methods for sensorless adaptive optics correction can utilise one of a number from a suite of image quality metrics that can be easily extended to include additional sample or imaging method-specific metrics. These methods are automated, require minimal user involvement and setup and are tied to simple, descriptive buttons on the Microscope-Cockpit UI allowing for greater accessibility to users, shown in Figure 3.1. The functions specific to the DM are shown in Figure 3.1a. These methods are divided into two categories: Set-up methods and Sample Correction methods. Figures 3.1b - 3.1d are optional windows that can be used by advanced users to change certain parameters used in the correction routines. How these parameters affect the correction routines will be explained in the relevant sections.

3.1 Set-up Methods

As previously described in Section 2.2.1, DeepSIM has multiple beam paths; interferometric, widefield and SIM. The interferometric beam path described in Figure 2.4 is used for calibrating the deformable mirror. An image is formed by the interference between the reference beam arm and the system beam arm. The size of the reference beam is larger than that of the system beam to ensure easy alignment between the two arms. It is therefore necessary to have a method for selecting the interferometric region of interest (ROI) i.e. the region where the reference and system beam arms interfere. Microscope-Cockpit implements such a method as the functionality of the "Select RO" button shown in Figure 3.1a. This spawns the window shown in Figure 3.2 where the user can draw a circle which will define the interferometric ROI. The coordinates of this ROI are saved to the Microscope-Cockpit configuration files with the "Save ROI" button.

3.1.1 Direct wavefront sensing

The two most common methods for direct wavefront sensing are Shack-Hartmann and interferometric methods. Shack-Hartmann wavefront sensing is useful for instances where accuracy is less important than the speed of wavefront recovery. While these situations do exist, the current use-cases for direct wavefront sensing within DeepSIM and Microscope-AOtools are calibration and system aberration

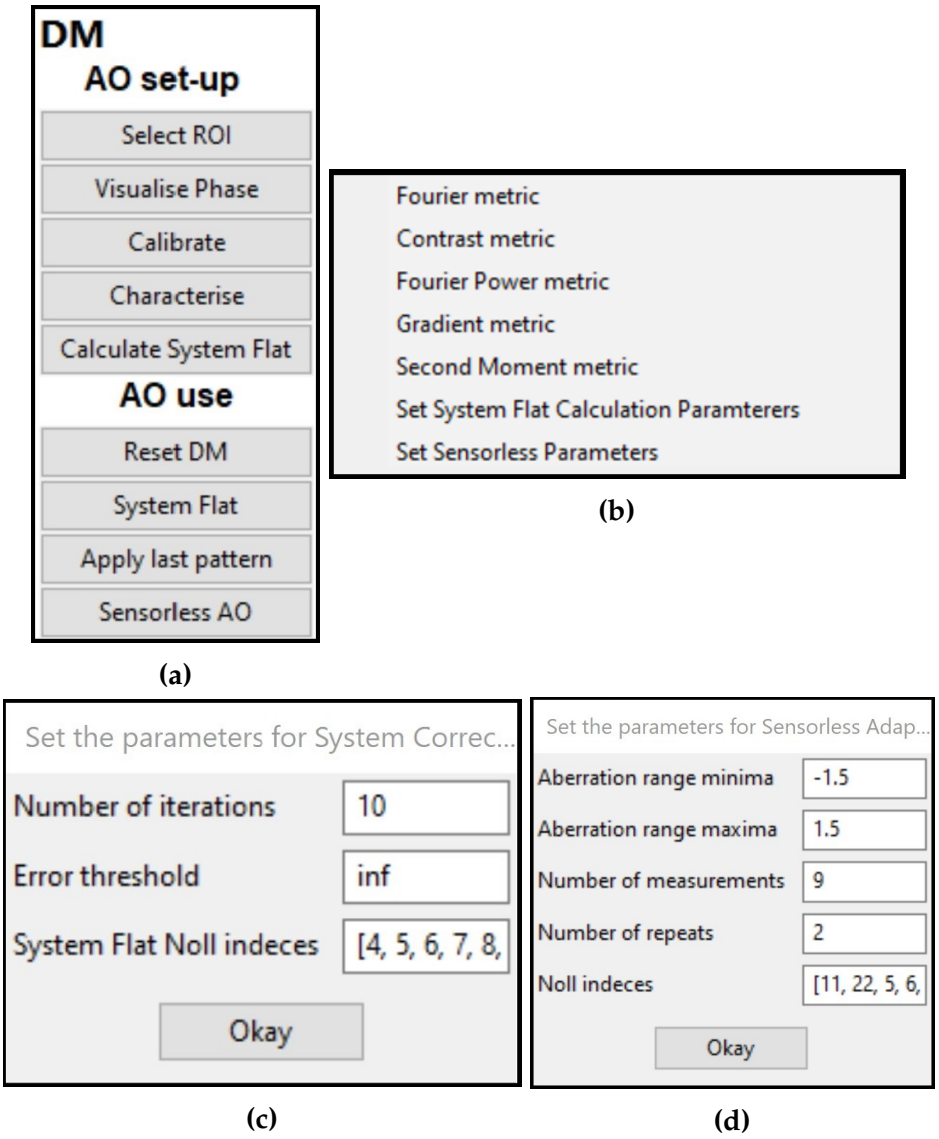
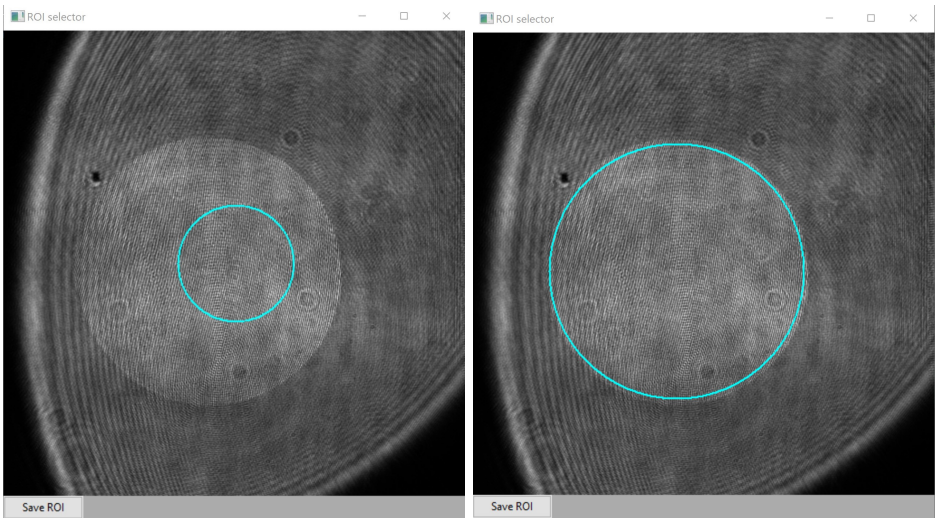


Figure 3.1: *Microscope-Cockpit GUI DM specific functionality.* ***(a)*** *Deformable mirror specific functions on the Microscope-Cockpit UI* ***(b)*** *Options window used for changing the image quality metric used in the sensorless AO routine and to spawn additional parameter varying windows* ***(c)*** *Options window for varying the parameters used in the system aberration correction routine.* ***(d)*** *Options window for varying the parameters used in the sensorless AO routine.*



(a) **(b)**

Figure 3.2: *User interface for selecting the interferometric region of interest. The bright circular region is the interference pattern generated by the overlap of the reference beam arm and the circular DM aperture. The reference beam profile is larger than the DM aperture in order to obtain a sufficient angular offset between the two arms to ensure a good separation of the amplitude and phase components.* ***(a)*** *The ROI selector UI when it is first initialised* ***(b)*** *UI with the ROI selected*

correction. These are both situations where accuracy is considerably more important than speed, and therefore a Shack-Hartmann wavefront extraction method has not yet been implemented. Additionally, implementing phase extraction from interferometric data has proven more challenging to automate than from Shack-Hartmann sensor data. Interferometric data can be defined as:

$$I(x,y,t) = a(x,y) + b(x,y)cos[\phi(x,y) + \Phi_R(x,y,t)], \tag{3.1}$$

where $a(x,y)$ describes the variation of the background illumination, $b(x,y)$ describes the noise and contrast variations, $\phi(x,y)$ describes the phase imparted by the DM surface and $\Phi_R(x,y,t)$ is the reference phase at time t. $\Phi_R(x,y,t)$ is an offset in the measured phase position, and any variation in this term shifts the lateral position of the entire interference pattern. The relevant phase information is encoded in the $\phi(x,y)$ term and this term specifies shape and spacing of the interference pattern. $\Phi_R(x,y,t)$ can therefore be arbitrarily set to 0, simplifying the cosine term in Equation 3.1 to $cos[\phi(x,y)]$. Expanding this simplified cosine term using Euler's formula, as well as the definition that $c(x,y) = \frac{1}{2}b(x,y)e^{i\phi(x,y)}$, leads to:

$$I(x,y) = a(x,y) + c(x,y) + c^*(x,y), \tag{3.2}$$

where $c^*(x,y)$ is the complex conjugate of $c(x,y)$. Applying the 2-D Fourier transform Equation 3.2 becomes:

$$\tilde{\boldsymbol{I}}(u,v) = \tilde{\boldsymbol{A}}(u,v) + \tilde{\boldsymbol{C}}(u,v) + \tilde{\boldsymbol{C}}^*(u,v), \tag{3.3}$$

where bold text and $\sim$ indicates the Fourier transform of the respective real-space functions. It can be shown that the Fourier transform of a real-valued function is Hermitian. A Hermitian function, $f(x)$ is a complex function with the property that $f^*(x) = f(-x)$, where $f^*(x)$ is the complex conjugate of $f(x)$. Given that $I(x,y)$ is real valued, it follows that $\tilde{\boldsymbol{I}}(u,v)$ is Hermitian. The amplitude spectrum is symmetric around the zero position (i.e. $u = 0$, $v = 0$). It follows then that $\tilde{\boldsymbol{C}}(u,v)$ and $\tilde{\boldsymbol{C}}^*(u,v)$ must contain the same information, only centred on different spatial frequencies. One can apply a bandpass filter in the spatial frequency domain to remove both $\tilde{\boldsymbol{A}}(u,v)$ and $\tilde{\boldsymbol{C}}^*(u,v)$ to leave only $\tilde{\boldsymbol{C}}(u,v)$[137]. Applying the inverse Fourier transform yields $c(x,y)$, which is now complex. The phase of the wavefront can then be recovered by:

$$\phi(x,y) = \arctan\left(\frac{\Im\{c(x,y)\}}{\Re\{c(x,y)\}}\right), \tag{3.4}$$

where $\Re\{c(x,y)\}$ and $\Im\{c(x,y)\}$ are the real and imaginary components of $c(x,y)$ respectively. In the phase acquisition workflow shown in Figure 3.3, these mathematical steps are implemented in a practical way. The interferogram (3.3a) is cropped (3.3b) and the ROI, that is the area described by Equation 3.1, is isolated by masking out all the information outside the ROI. The desired ROI is provided by the user using the ROI selector shown in Figure 3.2b. Quadrant shifting the image (3.3e) and applying a tukey (or cosine-tapered) window mask (3.3f) is done to minimise the spurious spatial frequencies which arise from performing a fast Fourier transform (FFT) on an image with sharp discontinuities at the quadrant edges.

Having performed the FFT (3.3h), an array described by Equation 3.3 is obtained. A selection of the central spatial frequencies are masked (3.3i), primarily to mask out the central spatial frequency which represents the mean intensity and has an amplitude orders of magnitude larger than any other spatial frequency. The spatial frequencies which now have the highest amplitudes correspond to both $\tilde{\boldsymbol{C}}(u,v)$ and $\tilde{\boldsymbol{C}}^*(u,v)$. One of the aforementioned amplitude peaks is located and a bandpass filter described by $\sin^2(x,y)$ is constructed (3.3j) centred on the spatial frequency location of this amplitude peak. As previously noted, the Fourier transform of

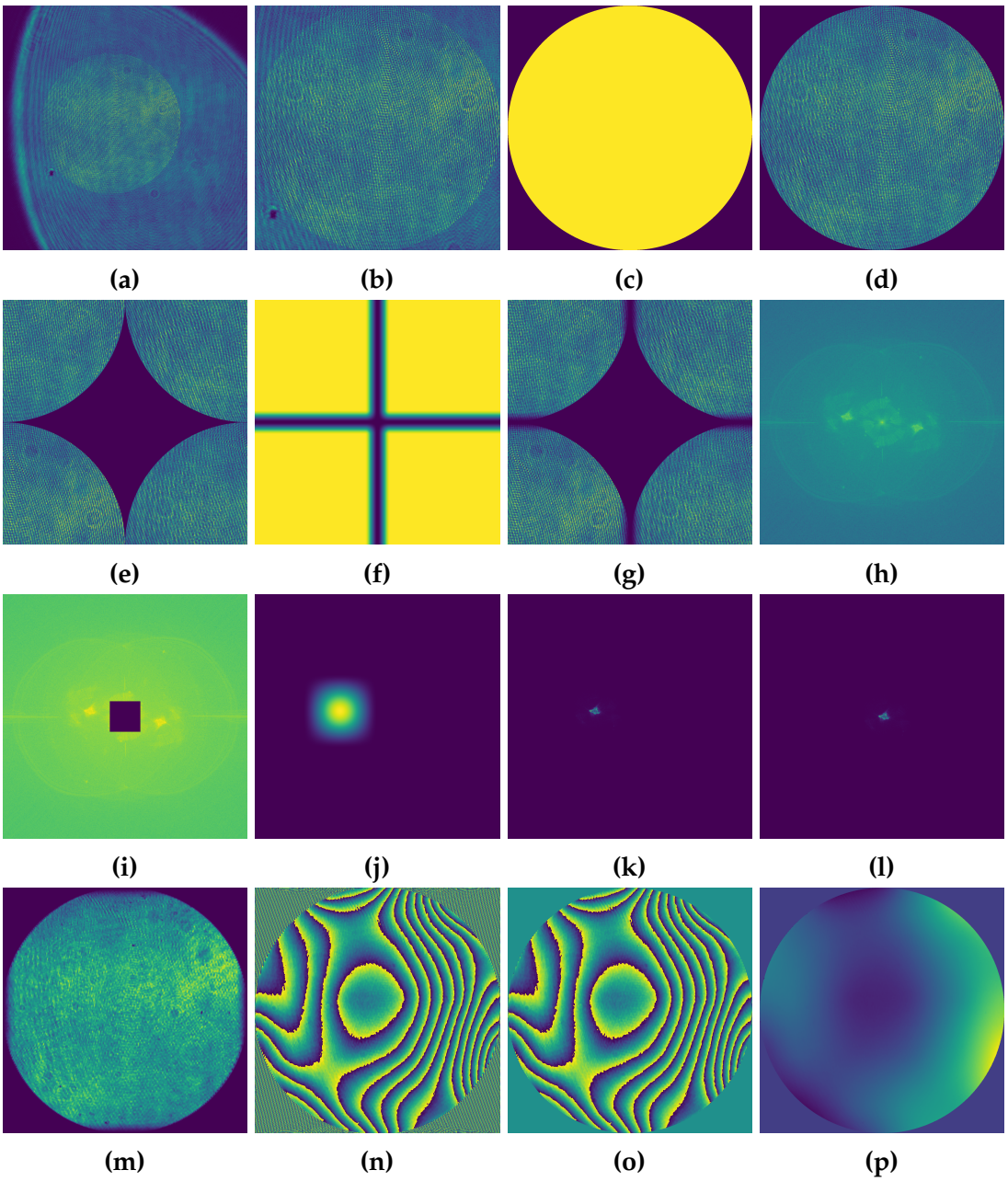


Figure 3.3: *Visualisation of the stages of the phase acquisition workflow.* ***(a)*** *Captured interferogram* ***(b)*** *Interferogram cropped to region of interest (ROI)* ***(c)*** *Circular mask* ***(d)*** *ROI isolated* ***(e)*** *ROI quadrant shifted (ROI-qs)* ***(f)*** *2-D tukey window mask* ***(g)*** *ROI-qs with tukey mask applied* ***(h)*** *Fast Fourier transform (FFT) of* ***(g)****, log scaled* ***(i)*** *Fourier transform with the central spatial frequencies masked, log scaled* ***(j)*** *2-D sine squared mask centred on the position of spatial frequencies encoding the phase information* ***(k)*** *The original Fourier transform,* ***(h)****, with the sine squared mask applied* ***(l)*** *Phase encoding spatial frequencies rolled to the central position* ***(m)*** *Inverse FFT of the phase encoding spatial frequencies* ***(n)*** *Inverse FFT transformed into a phase map* ***(o)*** *Phase map masked to isolate ROI* ***(p)*** *Phase map unwrapped to remove 2π discontinuities*

the interferogram is symmetrical around the central spatial frequency. Although which peak is selected will affect the sign of the phase in realspace, the two peaks otherwise encode the same information. Since the same peak is selected for all future phase extractions, the sign convention is preserved throughout and therefore it doesn't matter which of the two peaks this filter is centred. The aforementioned $\sin^2(x,y)$ bandpass filter is then applied to the FFT of the interferogram (3.3k). The spatial frequencies within this bandpass filter are then translated to the central spatial frequency position (3.3l). Applying this successfully filters $\tilde{\boldsymbol{A}}(u,v)$ and $\tilde{\boldsymbol{C}}^*(u,v)$, isolating $\tilde{\boldsymbol{C}}(u,v)$ as desired.

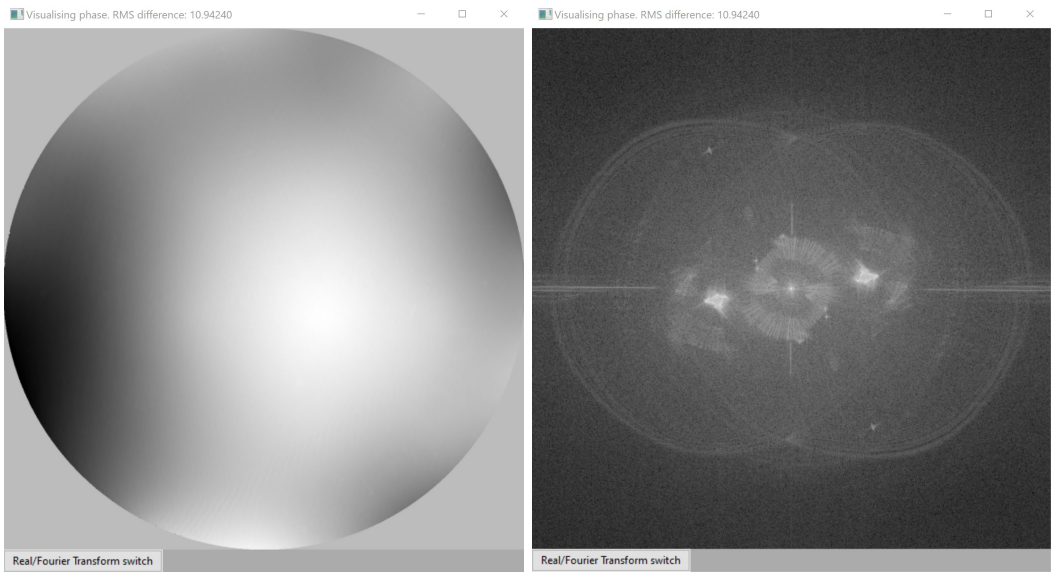
The array corresponding to $\tilde{\boldsymbol{C}}(u,v)$ is inverse Fourier transformed to yield $c(x,y)$ (3.3m). This is then converted to a phase map by performing the calculation in Equation 3.4 (3.3n) and the mask in Figure 3.3c is applied again to mask out any spurious noise outside the ROI. Due to the periodic nature of trigonometric functions, this phase map is wrapped around $-\pi$ and π radians. A 2D algorithm is used to unwrap the phase map and yield a continuous wavefront similar to Figure 3.3p[138]. Other than determining the appropriate ROI, this workflow is entirely automated and requires no user input.

Automation does have a drawback. The location of the phase component of the Fourier transform is determined by finding the maximum intensity in the data represented by Figure 3.3i and then performing a number of centre of mass calculations to find the 'true' centre of the phase component. However, this 'true' centre may still be incorrect by a few pixels. This offset leads to an artificial introduction of tip and/or tilt in the final wavefront and this artificial tip/tilt cannot be separated from the true tip/tilt. Therefore, the described phase acquisition implementation is not sensitive to tip or tilt. However, since tip and tilt (along with piston) are not generally considered to be true optical aberrations, this is a small price to pay for a fully automated phase acquisition workflow.

This phase extraction technique is used as part of other methods, but it is also useful for a user to be able to visualise the wavefront phase map. Principally visualising the wavefront phase map is useful because if the interferogram is not well focused on the camera it can result in the wavefront being heavily distorted by the Zernike mode corresponding to the defocus optical aberration (Noll Index 4). This can mask smaller wavefront deformations caused by the movement of the DM actuators and therefore bias calibration measurements. This distortion is obvious by viewing either the wavefront phase map (since the wavefront will look similar to the defocus optical aberration) or the power spectrum (where the phase

information will be spread over a large region in Fourier space). For sufficiently poor focus, the phase information is spread over a sufficiently large area in Fourier space that not all of it is captured by the $\sin^2(x, y)$ bandpass filter, which results in discontinuities in the wavefront phase map. This is immediately apparent by visualising the wavefront phase map and is a useful check to be able to perform

It can also be useful to view the system aberrations present, to check the difference applying the system aberration correction makes to the wavefront shape and to manually check for discontinuities. Microscope-Cockpit implements such a method as the functionality of the "Visualise Phase" button shown in Figure 3.1a. This spawns the window shown in Figure 3.4a, displaying the phase wavefront acquired from the interferogram. The display can be changed to the power spectrum of the interferogram, Figure 3.4b, and back by pressing the "Real/Fourier Transform switch" button.



(a) **(b)**

Figure 3.4: *User interface for viewing the phase wavefront* ***(a)*** *Phase viewer window showing the unwrapped phase acquired from the interferogram* ***(b)*** *Phase viewer window showing the power spectrum of the interferogram.*

3.1.2 Zernike Mode Amplitude Measurement

Recall from Section 1.3.1 that a phase wavefront can be represented by a linear combination of Zernike polynomials:

$$\Phi(\rho,\theta) = \sum_{n,m} \alpha_n^m \mathcal{Z}_n^m(\rho,\theta), \tag{1.26}$$

where indices $n \in \mathbb{N}_0$ and $m \in \mathbb{Z}$ denote the radial order and azimuthal frequency respectively of the Zernike polynomial, $\mathcal{Z}_n^m$, and are such that $n - |m| \geq 0$ and even. The coefficients of each Zernike polynomial are represented by $\alpha_n^m \in \mathbb{R}$. For simplicity, we switch the notation convention of the Zernike modes and the corresponding amplitudes to $\mathcal{Z}_j(\rho,\theta)$ and α_j where j is the Noll index of the Zernike mode with n radial order and m azimuthal frequency.

Now, the Zernike polynomials are an orthogonal set of polynomials, and the orthonormality of Zernike polynomials is expressed by[78]:

$$\frac{\int_0^1 \int_0^{2\pi} \mathcal{Z}_j(\rho,\theta)\, \mathcal{Z}_{j'}(\rho,\theta)\, \rho d\rho d\theta}{\int_0^1 \int_0^{2\pi} \rho d\rho d\theta} = \delta_{jj'}, \tag{3.5}$$

where:

$$\delta_{jj'} = \begin{cases} 1, & j = j' \\ 0, & j \neq j' \end{cases}. \tag{3.6}$$

Therefore, performing the operation:

$$\frac{\int_0^1 \int_0^{2\pi} \Phi(\rho,\theta)\, \mathcal{Z}_j(\rho,\theta)\, \rho d\rho d\theta}{\int_0^1 \int_0^{2\pi} \rho d\rho d\theta} = \alpha_j, \tag{3.7}$$

allows the j-th Zernike mode coefficient, α_j, present in the phase wavefront $\Phi(\rho,\theta)$ to be determined. Microscope-AOtools uses this calculation to determine the Zernike mode amplitudes present in the measured phase wavefront. However, this takes a discrete form:

$$\frac{trapz\left[trapz\left[\Phi(x,y)\, \mathcal{Z}_j(x,y)\right]\right]}{N} = \alpha_j, \tag{3.8}$$

where $trapz[]$ is *scipy*'s implementation of integration using the composite trapezoidal rule, N is the total number of pupil pixels, and x, y are the pixel coordinates of the phase wavefront image, and the Zernike mode with a unit amplitude is simulated using AOtools[133, 136]. This process is repeated for M Zernike modes to obtain a row vector, z, containing the M computed Zernike mode amplitudes present.

Unfortunately, this method of measuring the Zernike mode amplitudes is not perfect. The limitations of this method are explored more fully in Section 6.1.1, but

at this point it should be noted that for a wavefront resized to $\sim 128 \times 128$, the accuracy of Zernike mode amplitude measurements is $\sim 80\% - 90\%$ for the first 7 radial orders of Zernike modes. This is sufficient to achieve a good calibration and aberration correction as will be shown.

3.1.3 Calibration

For aberration correction, one could attempt to measure the overall aberration of the optical wavefront and apply the opposite shape to the DM. For direct wavefront sensing, this would appear as simple as measuring the phase distortion and shaping the DM to cancel this distortion. However, for continuous membrane DMs (which the majority of commercially available DMs are) the response of mirror shape to the actuators which control the mirror shape is not entirely linear (primarily at close to the minimum and maximum extensions of the actuators), due to the membrane's mechanical elasticity, electrostatic forces, and the coupling between actuators[139]. For indirect wavefront sensing this presents an even greater problem since any minimisation of the wavefront aberration would involve N degrees of freedom, where N is the number of actuators. Assuming that the overall mirror shape is the linear superposition of all the individual actuator deflections, we can define the overall mirror shape, $S(x, y)$ as:

$$S(x, y) = \sum_{h=1}^{N} d_h \phi_h(x, y), \tag{3.9}$$

where $S(x, y)$ is the change in the deformable mirror shape from its original position, d_h is the h-th actuator control signal (an arbitrary value related to applied voltage which determines the position of the h-th actuator in its overall movement range) and $\phi_h(x, y)$ is the h-th influence function, so called as they describe how the elements of the device influence the phase wavefront across the whole pupil. We can convert this set of basis functions to a different basis set. Since $\phi_h(x, y)$ describes the effect of the device elements affect the phase wavefront, an obvious choice of alternative basis set is the Zernike polynomials from before. Describing $\phi_h(x, y)$ in terms of Zernike polynomials we obtain:

$$\phi_h(x, y) = \sum_{g=1}^{M} b_{g,h} z_g(x, y), \tag{3.10}$$

where $b_{g,h}$ is the coefficient corresponding to the g-th Zernike polynomial due to d_h, the h-th actuator control signal (i.e. the relationship between how the h-th actuator position affects the g-th Zernike mode amplitude). This leads to:

$$\begin{aligned} S(x,y) &= \sum_{h=1}^{N} d_h \left[\sum_{g=1}^{M} b_{g,h} z_g(x,y) \right] \\ &= \sum_{g=1}^{M} \left(\sum_{h=1}^{N} d_h b_{g,h} \right) z_g(x,y) \\ &= \sum_{g=1}^{M} a_g z_g(x,y), \end{aligned} \tag{3.11}$$

where the new Zernike coefficients, a_g, are defined as:

$$a_g = \sum_{h=1}^{N} b_{g,h} d_h \text{ for } g = 1, 2, ..., M. \tag{3.12}$$

Converting this to a matrix form yields:

$$\begin{aligned} \bar{a} &= \boldsymbol{B}\bar{d} \\ \Rightarrow \bar{d} &= \boldsymbol{C}\bar{a}, \end{aligned} \tag{3.13}$$

where $\bar{d}$ is a length N vector of the actuator control signals, $\bar{a}$ is the length M vector of the Zernike polynomial amplitudes and $\boldsymbol{B}$ is the $M \times N$ matrix representing the response characteristics of the deformable mirror. However, we actually want its inverse, $\boldsymbol{B}^{-1} = \boldsymbol{C}$, otherwise called the control matrix, in order to convert from Zernike polynomial amplitudes to actuator control signals.

Microscope-AOtools implements an automated calibration routine to obtain $\boldsymbol{C}$. Each actuator is moved through p set positions and a wavefront is extracted at each position. Figure 3.5a shows an observed wavefront during the calibration routine. The wavefront is then decomposed into M Zernike modes[136]. A row vector $\boldsymbol{z}$ is obtained for each actuator position containing the computed Zernike mode amplitudes:

$$\boldsymbol{z} = \begin{bmatrix} z_1 & z_2 & \cdots & z_g & \cdots & z_M \end{bmatrix}, \tag{3.14}$$

Where the g-th element is the amplitude of the g-th Zernike mode. Figure 3.5d shows a plot of the row vector containing the amplitudes of the M Zernike modes measured for Figure 3.5a using the method described in Section 3.1.2. Figure 3.5b

show a simulated wavefront constructed using these Zernike mode amplitudes. As previously mentioned, any continuous phase wavefront can be constructed from an infinite linear combination of Zernike modes[73]. However, using a finite number of Zernike modes produces an approximation of the original wavefront. Figure 3.5c show the difference between the two. A "ringing" analogous to the Gibbs phenomena when recreating periodic signals using a truncated Fourier series is present[140].

By collecting the row vectors of each position for the h-th actuator we can obtain:

$$A_h = \begin{bmatrix} \boldsymbol{z_1} \\ \boldsymbol{z_2} \\ \vdots \\ \boldsymbol{z_p} \end{bmatrix} = \begin{bmatrix} z_{1,1} & z_{1,2} & \cdots & z_{1,M} \\ z_{2,1} & z_{2,2} & \cdots & z_{2,M} \\ \vdots & \vdots & \ddots & \vdots \\ z_{p,1} & z_{p,2} & \cdots & z_{p,M} \end{bmatrix}. \tag{3.15}$$

The row vector shown in Figure 3.5d was obtained at the first of the p positions i.e. $\boldsymbol{z_1}$. Applying linear regression to each column, $\begin{bmatrix} z_{1,i} & z_{2,i} & \cdots & z_{p,i} \end{bmatrix}^T$, yields the response characteristics between the h-th actuator's position and the g-th Zernike mode, $b_{g,h}$. Figure 3.5e shows the influence function fitting for primary spherical aberrations (Noll index 11) for the 26$^{\text{th}}$ actuator. The gradient of the slope is, in this case, $b_{11,26}$. This gradient is acquired for each actuator, for each Zernike mode. In this way, we construct $\boldsymbol{B}$ and then calculate $\boldsymbol{C}$. Figure 3.6 shows a flowchart of this process as implemented in Microscope-AOtools.

In general, $\boldsymbol{B}$ is singular, or near singular, and therefore has no true inverse. So, we must use a pseudo-inverse, calculated using single value decomposition (SVD). Actuators that have little influence on particular Zernike modes will have small values in the $\boldsymbol{B}$ matrix. These small influence values occur due to a combination of the actuators being in physical positions where they have limited influence over certain Zernike modes and noise, which leads to small perturbations in the measured Zernike mode amplitudes and are unrelated to the actuator movement. A control matrix calculated without thresholding out these small values before inversion will quickly lead to a saturation of the deformable mirror actuators (i.e. actuators at their maximum stroke length) when corrections are calculated[141]. This occurs because small values in $\boldsymbol{B}$ become large values in the $\boldsymbol{C}$, which results in large actuator signals, d_i, even at low Zernike mode amplitudes for certain actuators which try to correct modes which they have minimal influence over. Therefore, the calibration method incorporates a threshold by default and the exact

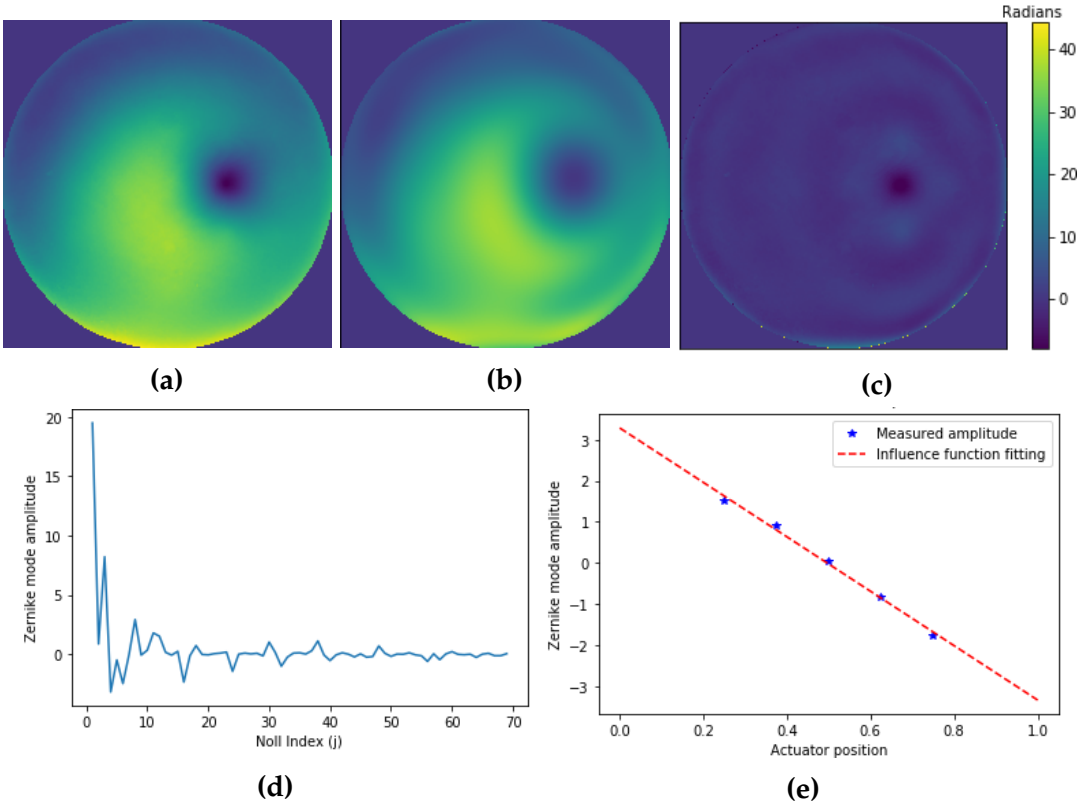


Figure 3.5: *Visualisation of the influence function fitting stage of the calibration routine* ***(a)*** *An example observed wavefront obtained during the calibration process for an Alpao-69 actuator deformable mirror. The* 26^{th} *actuator is at the first of the 5 positions.* ***(b)*** *A simulated wavefront created from the 69 Zernike mode amplitudes measured in the observed wavefront.* ***(c)*** *The difference in the observed and simulated wavefronts.* ***(d)*** *The 69 Zernike mode amplitudes measured for the observed wavefront* ***(e)*** *The influence function fitting for primary spherical aberrations (Noll index 11) for the* 26^{th} *actuator*

threshold can be varied by experienced users. The calibration routine is initiated by pressing the "Calibrate" button shown in Figure 3.1a.

3.1.4 Characterisation

Feedback on the quality of the calibration process is essential. Ideally, once the deformable mirror is calibrated we have a linear map which allows known quantities of Zernike modes to be applied exactly. This linear map is never exact in practice due to a number of issues; the fact that some parameters, such as the number of steps used to calibrate each actuator and the threshold used in the SVD pseudo-inversion, are chosen empirically, the approximate nature of the pseudo-inverse, discretisation errors (due to discrete sampling of a continuous functions) in the measuring of Zernike modes, etc. It is therefore necessary to have

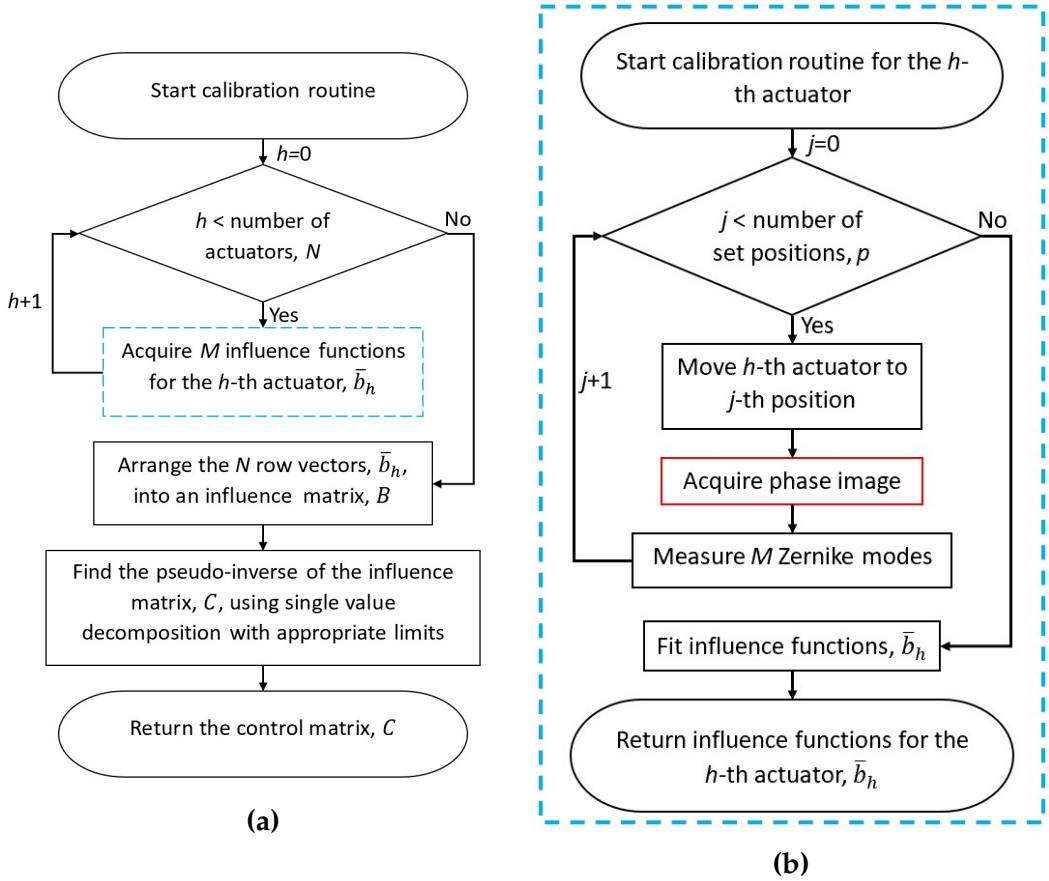


Figure 3.6: ***(a)*** *Flowchart depicting the generalised calibration routine implemented in Microscope-AOtools* ***(b)*** *Flowchart depicting the process for calibrating the h-th actuator of the deformable mirror, the dashed blue process in* ***(a)****. The influence functions returned are $b_{g,h}$ described in Equation 3.10. This process is performed for each N actuators and used to obtain* ***C*** *described in Equation 3.13.*

some measure of how well the adaptive element is able to recreate desired Zernike modes. This process is called characterisation. The process involves applying a fixed amplitude of single Zernike modes to the adaptive element, measuring the Zernike modes present and comparing the amplitude to that supposedly applied. An automated implementation of this process is present in Microscope-AOtools with the results returned to the user for interrogation. Figure 3.7 shows a flowchart of this method in Microscope-AOtools.

In an ideal situation, where the control matrix provided a perfect linear map from Zernike mode amplitudes to the adaptive elements degrees of freedom, a characterisation assay like Figure 3.8a is expected, where only the Zernike mode applied is measured. In practice, the adaptive element is better at recreating particular Zernike modes and some Zernike mode coupling is observed i.e. Zernike

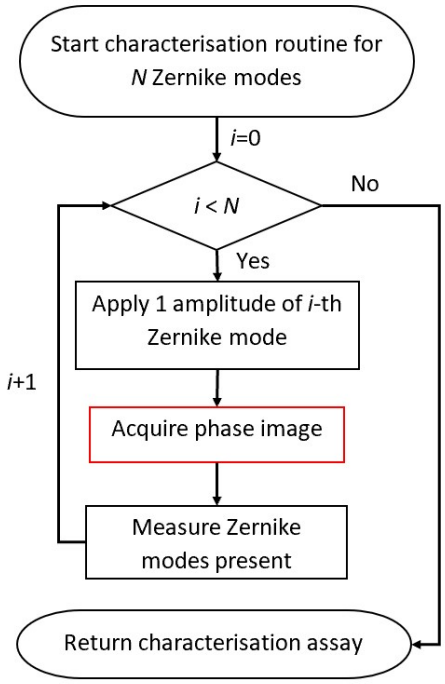


Figure 3.7: *Flowchart depicting the process for characterising a deformable mirror as implemented in Microscope-AOtools*

modes which were not applied to the adaptive element are measured. This leads to characterisation assays like Figure 3.8b. Here we present a characterisation assay obtained for an Alpao-69 actuator deformable mirror. We define a recreation accuracy metric, α_i, for each mode:

$$\begin{aligned} \alpha_i &= \frac{Z'_i - \boldsymbol{RMS}(Z'_j)}{Z_i} \\ &= \frac{Z'_i - \sqrt{\frac{1}{N-1}\sum_{j=0, j\neq i}^{N} Z'^2_j}}{Z_i} \end{aligned} \tag{3.16}$$

Where Z_i is the applied Zernike mode amplitude, Z'_i and Z'_j are the measured Zernike mode amplitudes for the current mode and all other modes respectively and N is the number of Zernike modes being assessed. Figure 3.8c shows a plot of this metric for the characterisation assay in Figure 3.8b. The errorbars are determined by the standard deviation of $\boldsymbol{RMS}(Z'_j)$

Clearly not all Zernike modes are recreated equally well and different modes exhibit varying degrees of mode coupling. As previously mentioned, this arises from mathematical approximations, computational errors and the physical characteristics of the adaptive element. Microscope-AOtools provides the tools to assess

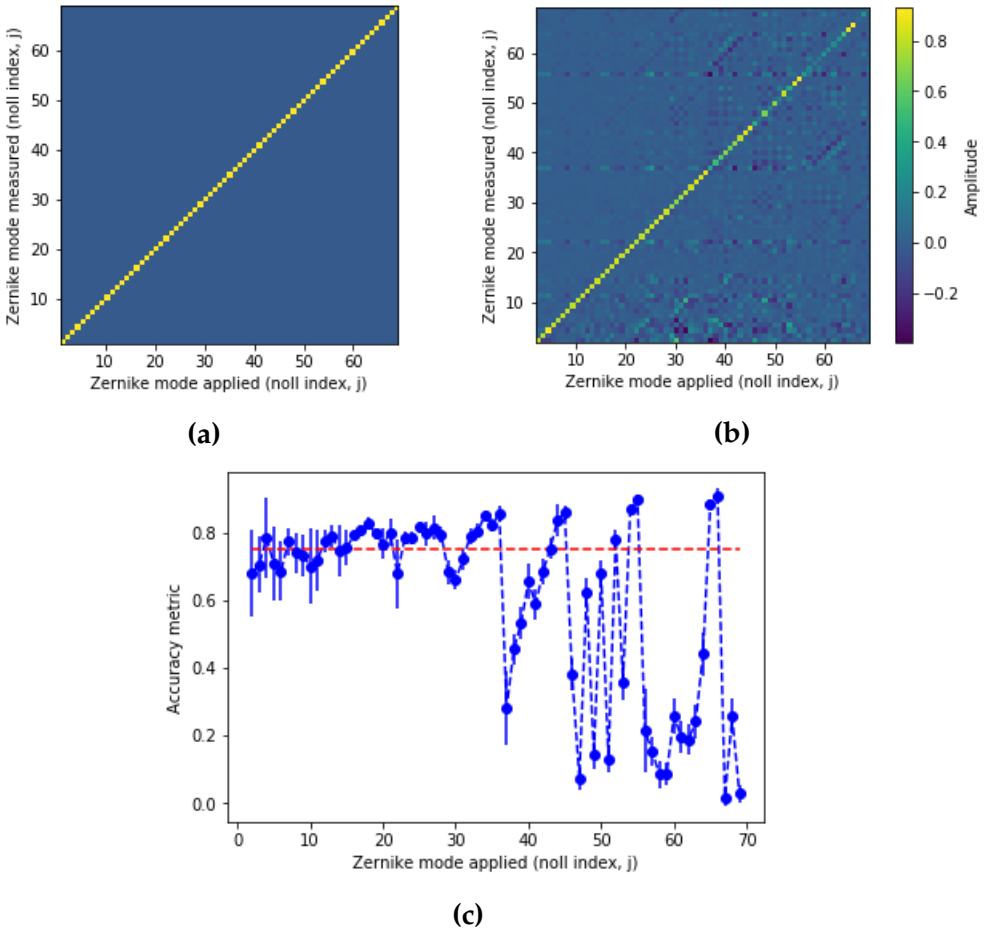


Figure 3.8: *Example characterisation routine results* ***(a)*** *An ideal characterisation assay, measuring the recreation accuracy of 68 Zernike modes with applied amplitude of 1 for each* ***(b)*** *A realistic characterisation assay obtained from a calibrated Alpao-69 actuator deformable mirror, measuring the recreation accuracy of 68 Zernike modes with applied amplitude of 1 for each* ***(c)*** *Plot of the recreation accuracy metric for the real characterisation assay shown in* ***(b)****. The threshold (red dashed line) is set at 0.75*

the accuracy of Zernike mode recreation, which can be used to inform which modes should be included in the aberration correction algorithms. In general, correcting up to the third order spherical ($\mathcal{Z}_8^0$) is sufficient to recover a diffraction limited image and so a good reconstruction accuracy is only necessary for the first 29 Zernike modes[71].

The characterisation routine relies on the same generalised phase acquisition method used in the calibration workflow. Recall that this is a user selected method from a suite of phase acquisition methods. The number of Zernike modes assessed, N, is the number of modes that have been measured in the calibration step by default, but this can be varied by the user. Once again, this preserves

generalisability and allows the characterisation method to be used on any arbitrary adaptive element, calibrated for any number of modes and utilising any desired wavefront sensing technique.

3.1.5 System Aberration Correction

The applications for aberration correction using direct wavefront sensing have been well documented. The wavefront is measured via interferometry, Shack-Hartmann wavefront sensor, fluorescent guide star, etc and decomposed into Zernike modes. Correction can then be calculated and applied for both system and sample induced aberrations. Microscope-AOtools implements a correction method for situations where the wavefront is directly observed. The workflow is shown in Figure 3.9. The wavefront is obtained through whatever direct wavefront sensing method has been implemented and selected, a number of Zernike modes determined by the user are fitted to the wavefront using the method described in Section 3.1.2, an equal and opposite magnitude of these modes are applied to the DM. The RMS wavefront error is then calculated. This process repeats until N iterations have been performed and the RMS wavefront error is below a user defined error threshold, δ.

In an ideal setup with a perfect control matrix, this process would only need to be performed once. However, as we have already discussed, the control matrices generated for any setup are never ideal due to non-linearities and inter-actuator coupling. Therefore, one iteration of this method would correct the aberrations to an extent, but it would leave residual aberrations. It is necessary to perform this process for a number of iterations to ensure the optimal wavefront is obtained.

Figure 3.10 shows the results of one such wavefront correction, performed using the same Alpao-69 actuator deformable mirror as shown in Figure 2.4. The wavefront was obtained by interferometry and Zernike modes 5-29 (using Noll indices) were corrected over 20 iterations. Figure 3.10c shows the Zernike mode amplitudes before and after correction. The dots visible are the physical location of the actuators on the deformable mirror and represent a limiting factor in how flat the deformable mirror surface can actually be.

For system aberration corrections it may be preferable to set a minimum wavefront error and continue to iterate until this threshold is reached. However, a user may wish to only spend N iterations correcting the wavefront. Microscope-AOtools implements both options to ensure generalisability and these parameters can be set by the user utilising the option window shown in Figure 3.1c. As with the calibration and characterisation methods, the wavefront flattening routine

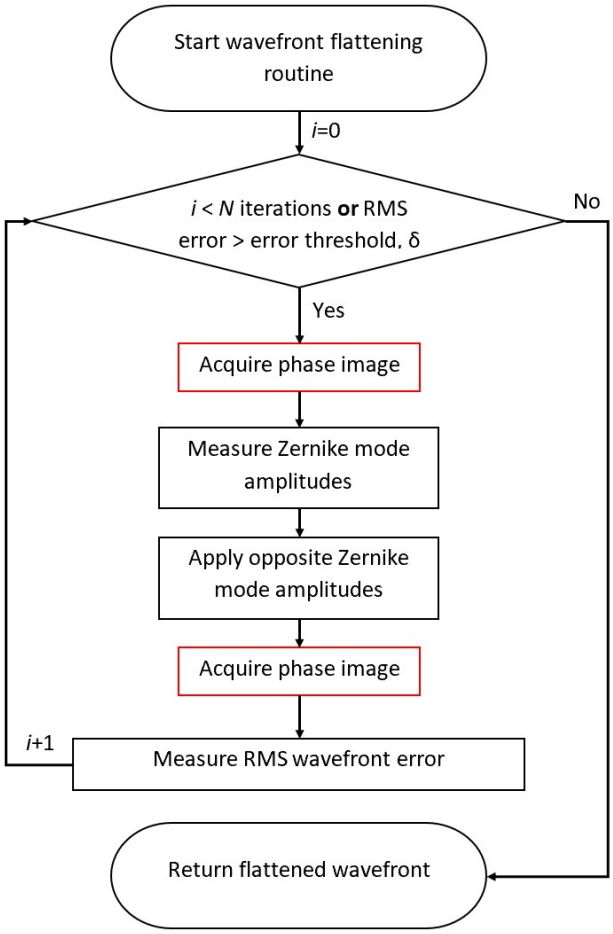


Figure 3.9: *Flowchart depicting the process for flattening directly measured wavefront as implemented in Microscope-AOtools*

relies on a user selected phase acquisition method selected from the suite of implemented phase acquisition methods. This generalised construction ensures that the applicability of Microscope-AOtools to any adaptive element with any wavefront sensing technique is preserved throughout all the set-up methods.

The system aberration correction routine is initiated by pressing the "Calculate System Flat" button shown in Figure 3.1a. Spawning the window shown in Figure 3.1c allows a user to vary the number of iterations and RMS error threshold used for the wavefront correction routine. By default, the routine runs for exactly 10 iterations, since the default error threshold is ∞ and so any wavefront deformation will yield an RMS value under this threshold. A user can also vary the Zernike modes the wavefront flatting routine will try to correct for. By default, the Zernike modes corrected for are all Zernike modes with Noll indices, j, greater than or equal to 4 (i.e. all the true optical aberrations) and less than the number of

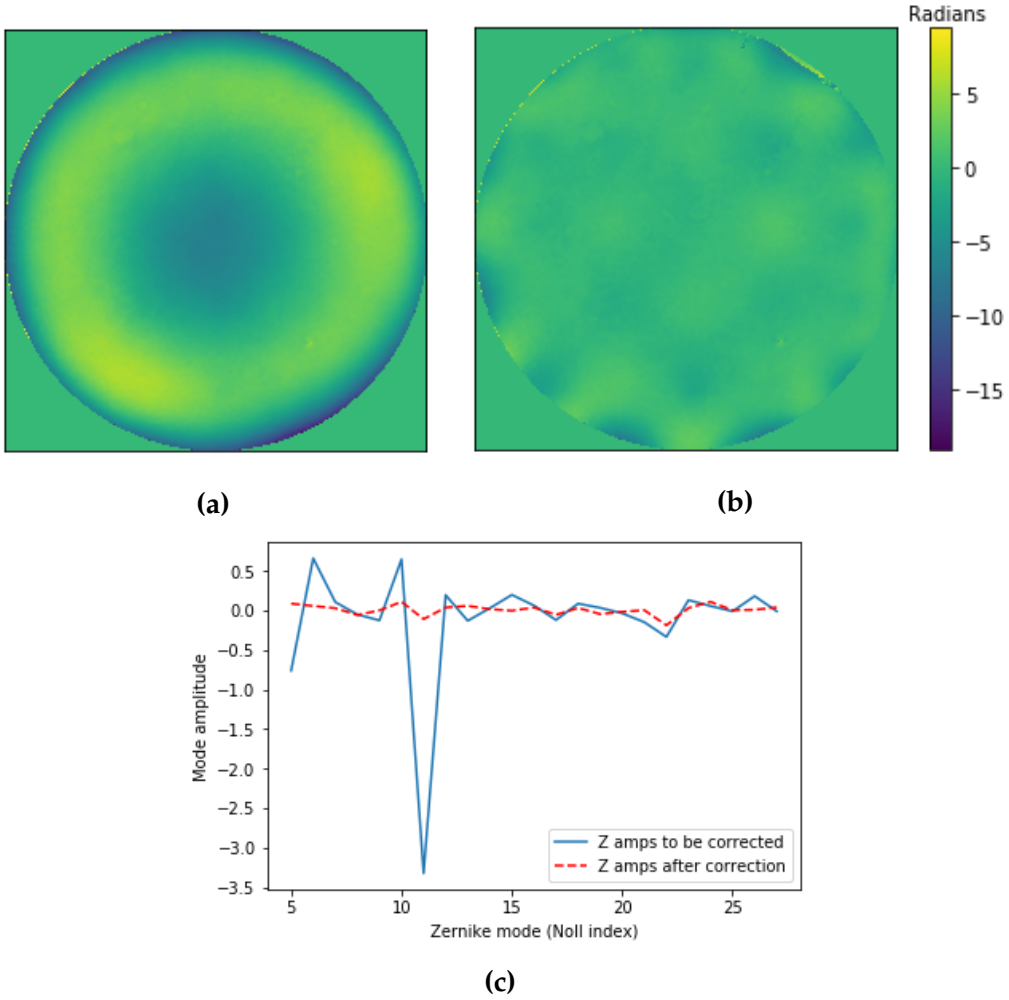


Figure 3.10: *Example direct wavefront correction results* ***(a)*** *An aberrated wavefront* ***(b)*** *A wavefront after 20 iterations of correction* ***(c)*** *The Zernike mode amplitudes measured in the aberrated (red) and corrected (blue) wavefronts* ***(a)*** *-* ***(b)*** *are all presented on the same colorscale (in radians of 543nm HeNe laser) and were obtains via interferometry*

actuators, N. Once the Characterisation routine has been performed this is changed to be all Zernike modes with $4 \leq j < N$ and with a recreation accuracy within 1 standard deviation of 0.75. Once the actuator values for correcting the system aberrations have been calculated they are stored in Microscope-Cockpit's internal configuration and can be applied at any time using the "System Flat" button shown in Figure 3.1a.

3.2 Sample Correction Methods

3.2.1 Sensorless Correction

Outside of imaging techniques where sharp foci are present - such as 2-photon microscopy or samples with "guide stars" present - or SMLM where the PSF is measured directly, direct wavefront sensing is not generally possible[101, 130, 131]. We therefore commonly rely on sensorless techniques to determine the best correction to apply. The generalised methodology for this is shown in Figure 3.11. Some metric, S, which gives a useful measure of the image quality is chosen. This metric should be a numerical value and should increase to a global maximum as the aberrations present decrease. Often these metrics are related to common measures of image quality, such as intensity or contrast. Some image quality metrics can be ignored for particular imaging modalities, such as overall intensity for widefield imaging systems. For each Zernike mode, Z_i, a number of amplitudes of that mode, α_j, are applied and an image of the sample obtained. The quality of each image, S_j is calculated. Assuming that S is a function of the Zernike mode amplitude applied, fitting a Gaussian function to the S_j values yields a Zernike mode amplitude, α_{max}, which theoretically yields the best image quality, S_{max}, for the current Zernike mode being corrected for.

The complexity of sensorless adaptive optics correction lies in selecting the best image quality metric. There have been numerous metrics developed which have been shown to be effective on certain sample types or imaging modalities[93, 94, 95, 98]. In order for an adaptive optics implementation to be considered generalised, it should not be tied to a particular sample type or imaging modality. For this reason, Microscope-AOtools offers a range of image quality metrics, all located in the program file *aoMetrics.py*.

Unlike the calibration, characterisation and direct wavefront sensing techniques, the sensorless adaptive optics routine is not a method implemented in Microscope-AOtools and simply called by Microscope-Cockpit. Instead, the sensorless correction routine relies on coordination between Microscope-Cockpit, Python Microscope and Microscope-AOtools. The biological sample is set up in the image plane. A known amplitude of the first Zernike mode to be corrected for is applied to the DM by Microscope-AOtools. Then the light sources and camera are triggered by Python Microscope and the image data is collected by Microscope-Cockpit. This is repeated for M measurements. Then, Microscope-Cockpit passes the M images to Microscope-AOtools where the image quality metric for each image is

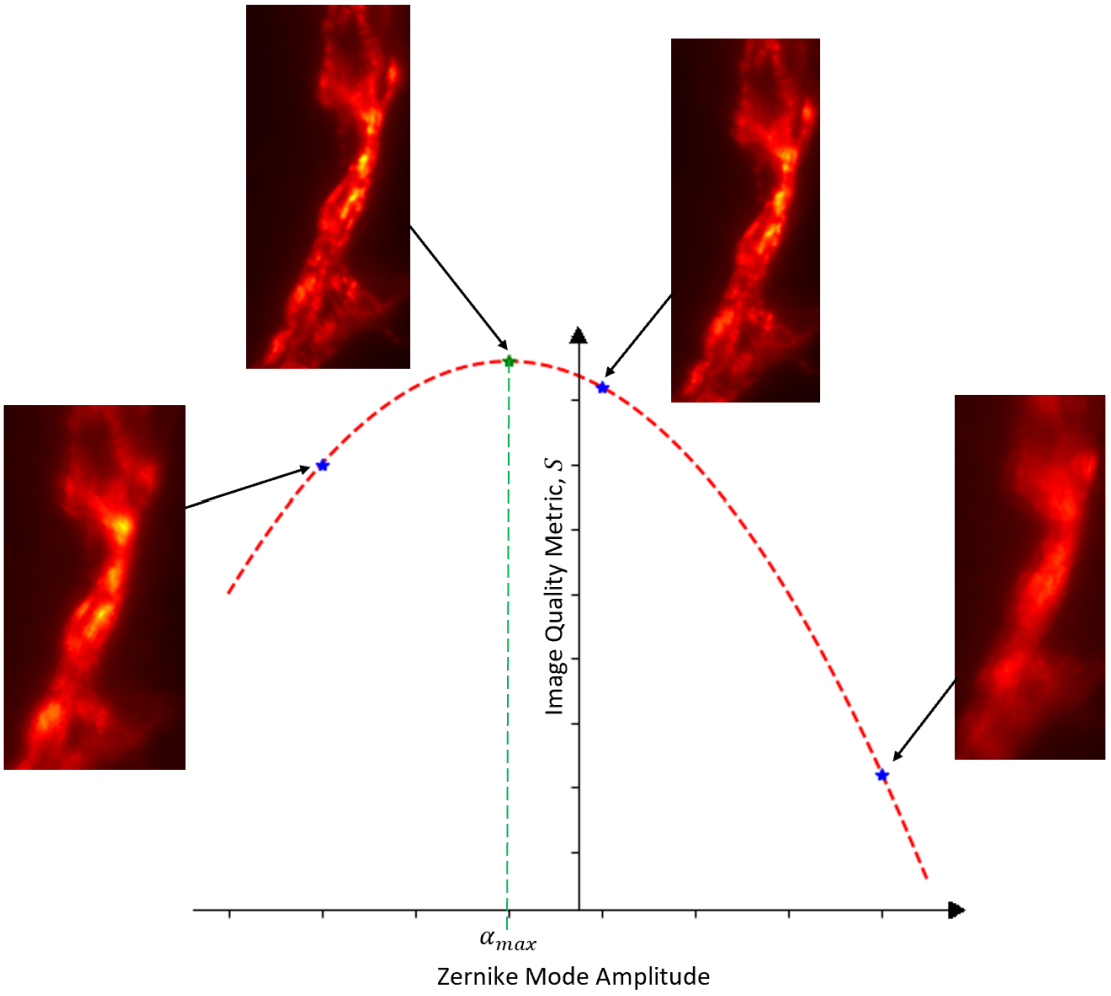


Figure 3.11: *Principle of sensorless adaptive optics correction. For each Zernike mode, Z_i, images of the sample with different amplitudes of the i-th Zernike mode are obtained. A value of the image quality metric, S, is obtained for each (blue dots). A Gaussian function is then fitted to these image quality metric values and the amplitude, α corresponding to the maximum image quality, S_{max}, is obtained (green dot). The inset images are Drosophila Neuro-muscular Junction with various amplitudes of spherical aberration present.*

evaluated. These values are then used to fit a Gaussian function and the mean of the Gaussian yields the Zernike mode amplitudes which should yield the maximum image quality, α_{max}. This amplitude is then applied to the DM and stored as the offset on top of which all further corrections should be applied. This process is then repeated for N Zernike modes. This whole process is further repeated for T iterations. Finally, the recorded Zernike mode amplitudes which have been corrected for and the actuator positions associated with that correction are stored in in Microscope-Cockpit's internal configuration. The sensorless adaptive optics routine is initiated by pressing the "Sensorless AO" button shown in Figure 3.1a. The workflow of this routine is shown in Figure 3.12

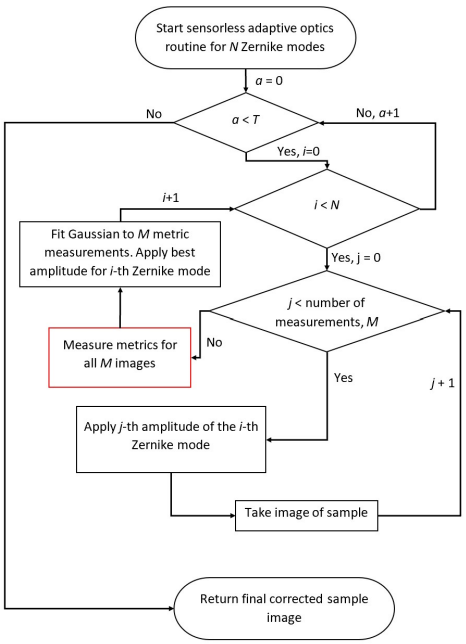


Figure 3.12: *Flowchart depicting the sensorless correction routine implemented on DeepSIM. All M images are taken, then the quality metric is obtained for all M images, the best Zernike amplitude is found and applied*

Clearly, this sensorless routine has multiple parameters and there is a limited degree to which these can be automatically selected. To this end, Figures 3.1 & 3.1b allow the user to vary these parameters. Figure 3.1b shows various options the user can select for the image quality metric to be used. As previously mentioned, different image quality metrics are optimised for different imaging modalities and sample types. Allowing the user to easily switch between metrics is critical for a generalised implementation of adaptive optics which is accessible to non-experts. Figure 3.1d shows a window which allows the user to vary the number of iterations,

T, the Zernike modes to be corrected, N and the number of measurements for each mode, M. By default, the Zernike modes corrected for are 1^{st} and 2^{nd} order spherical aberration, coma, astigmatism and trefoil (in that order) as in biological samples these are often the source of the most significant wavefront deformation, and therefore loss of image quality. The amplitudes applied to the DM are evenly spaced between the "Aberration range minima", z_{min} and "Aberration range maxima", z_{max}, in M intervals.

The values for z_{min} and z_{max} should ideally be chosen to scan a sufficient range of aberration amplitudes to ensure $z_{min} \leq \alpha_{max} \leq z_{max}$. α_{max} should at least be sufficiently close to z_{min} or z_{max} so that there is a clear increase in image quality as the aberration amplitude applied approaches one of these bounds. This range should not be too large otherwise a user risks either having sparse image quality data which only captures extreme aberrations and prevents an adequate fitting, or taking a sufficient number of measurements but introducing considerable photodamage. Like the image quality metrics, the $[z_{min}, z_{max}]$ range will vary with sample type and so some preliminary work is required before data collection proper to ascertain the correct range as well as the correct number of measurements and iterations, N and T, for a given sample type.

As previously mentioned, the $[z_{min}, z_{max}]$ range should ideally contain α_{max} or α_{max} should be close to one of these bounds. Allowing the Gaussian function to be fitted to the image quality metric values with no bounds (i.e. allowing α_{max} to take any value) becomes problematic when the image quality metric values remain largely constant over all the amplitudes applied. This phenomenon can occur for a number of reasons; α_{max} is found far outside the range of amplitudes scanned, the amplitudes sampled were sufficiently sparse that the central region of the Gaussian lies between two amplitudes, the aberration being sampled does not have a strong impact on the image quality measured, another, more significant aberration mode has not been corrected and the effect of this other mode is masking the effect of the current mode, etc. Whatever the reason, an unbounded fitting to a relatively flat profile of image quality metric measurements will lead to a large value of α_{max} which is unreliable and often results in an applying an aberration amplitude which severely damages the image quality. To ensure that the Gaussian fitting to find α_{max} yields a reasonable value, the fitting has bounds defined as $[z_{min} - 0.25(z_{max} - z_{min}), z_{max} + 0.25(z_{max} - z_{min})]$.

3.2.2 Image Quality Metric: Fourier Power

As mentioned in Section 3.2.1, sensorless AO correction requires an image quality metric which is well suited to both the imaging modality and the desired sample. Microscope-AOtools implements a suite of image quality metrics to choose from. Both the DeepSIM and the Aurox Clarity systems can be considered structured illumination systems i.e. the illumination of the sample has a spatially varying structure to it. The image quality of structured illumination systems is proportional to the amount of Fourier space information. Therefore, a sensible starting point for the image quality metric, S, is the total power of the Fourier spectrum:

$$S = \sum_{n,m} \left\| \tilde{\mathbf{D}}_{n,m} \right\|^2, \tag{3.17}$$

where $\tilde{\mathbf{D}}$ is the 2D discrete Fourier transform of the fluorescent signal (i.e. the camera image) and n and m are the pixel coordinates with ranges $[0, N-1]$ and $[0, M-1]$ respectively, where N and M are the number of pixels along each dimension of the image. $\|C\|$ is the modulus of a complex number, C, such that $\|C\| = \sqrt{CC^*}$ where C^* is the complex conjugate of C. From Parseval's Theorem, $\sum_{n,m} \left\| \tilde{\mathbf{D}}_{n,m} \right\|^2$ is the power of the observed signal. However, the Fourier spectrum obtained is not entirely composed of sample information. Recall from Section 1.2.1 that the fluorescent signal for a single image is the convolution of the distribution of fluorescent emission and the system point spread function (PSF):

$$\begin{aligned} F(\mathbf{r}) &= (E \circledast H)(\mathbf{r}) \\ F(\mathbf{r}) &= [D(\bar{x})I(\mathbf{r})] \circledast H(\mathbf{r}), \end{aligned}' \tag{1.12}$$

where $D(\mathbf{r})$ is the sample fluorescence distribution, $I(\mathbf{r})$ is the illumination pattern, $E(\mathbf{r})$ is the resultant emission signal and $H(\mathbf{r})$ is the system point spread function (PSF). For a widefield image, $I(\mathbf{r}) = 1$. Applying this substitution and a Fourier transform yields:

$$\begin{aligned} \mathcal{F}[\mathbf{F}(\mathbf{r})] &= \mathcal{F}[\mathbf{D}(\mathbf{r}) \circledast \mathbf{H}(\mathbf{r})] \\ \tilde{\mathbf{F}}(\mathbf{k}) &= \tilde{\mathbf{D}}(\mathbf{k})\tilde{\mathbf{H}}(\mathbf{k}) \\ &= \tilde{\mathbf{D}}(\mathbf{k})\mathbf{O}(\mathbf{k}) \end{aligned}, \tag{3.18}$$

where bold text and $\sim$ indicates the Fourier transform of the corresponding real-space function and $\mathbf{O}(\mathbf{k})$ is the system optical transfer function (OTF)[59].

The OTF both attenuates the sample fluorescence distribution spatial frequencies and acts as a lowpass filter. Since $\tilde{\mathbf{D}}_{n,m}$ is the 2D discrete Fourier transform of the observed data, this lowpass filter, $\mu_{n,m}$, is defined as:

$$\mu_{n,m} = \begin{cases} 1, & \sqrt{n'^2 + m'^2} \leq \omega_l \\ 0, & \sqrt{n'^2 + m'^2} > \omega_l \end{cases}, \tag{3.19}$$

where $n' = n - \frac{N-1}{2}$, $m' = m - \frac{M-1}{2}$ and ω_l is the lateral diffraction limit in reciprocal space as per Equation 1.8

Within the OTF lowpass limit, certain spatial frequencies will be dominated by noise contributions. As such, when attempting to quantify the power contribution from the fluorescence it is desirable to ignore the noise contributions. A thresholding mask, $\tau_{n,m}$ is created and defined as:

$$\tau_{n,m} = \begin{cases} 0, & \left\|\tilde{\mathbf{D}}_{n,m}\right\|^2 < \delta \\ 1, & \left\|\tilde{\mathbf{D}}_{n,m}\right\|^2 \geq \delta \end{cases}, \tag{3.20}$$

where δ is a noise threshold defined as:

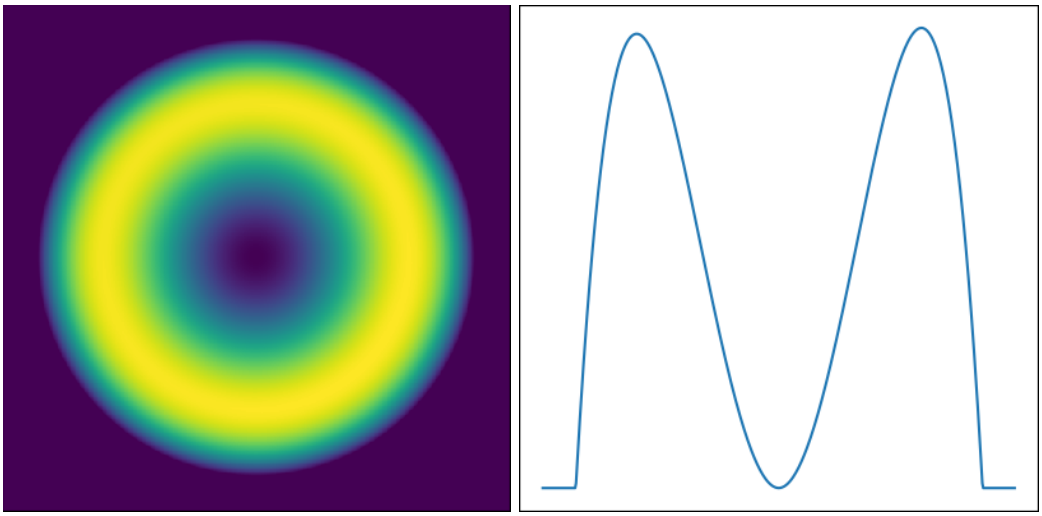
$$\delta = \frac{\alpha}{P_{noise}} \sum_{l,k} \left\|\tilde{\mathbf{D}}_{l,k}\right\|^2, \tag{3.21}$$

where $\left\|\tilde{\mathbf{D}}_{l,k}\right\|^2$ is the power in the l-th, k-th spatial frequency where l & k are the coordinates where $\mu_{n,m} = 0$, P_{noise} is the total number of pixels outside the OTF lowpass limit and α is a user defined amplification factor. In essence, the threshold is the mean of the power of the spatial frequencies consisting entirely of noise signals, scaled by α. The value of α must be chosen to threshold the spatial frequencies dominated by noise without losing the sensitivity to true, albeit low amplitude, spatial frequencies. Empirically, an $\alpha = 1.125$ offers a reasonable compromise between these traits. This approach assumed that the noise in the Fourier transform of the power spectrum is composed of Gaussian white noise. As such, it is very similar to several low cost scientific CMOS (sCMOS) noise reduction methods[142, 143].

Finally, the bulk of the improvement in spatial frequency content will occur in the mid to high frequencies (relative to ω_l). As such there is a desire for increased sensitivity to the power fluctuations in these spatial frequencies. A modulation mask, $\omega_{n,m}$, is constructed and defined as:

$$\omega_{n,m} = \beta \left| \left(1 - e^{\frac{\sqrt{n'^2+m'^2}}{\omega_l} - 1}\right) \left(n'^2 + m'^2\right) \right|, \tag{3.22}$$

Where ω_l, n' and m' are defined as before, $|...|$ is ... normalised to $[0, 1]$, and β is a user defined normalisation factor. In effect, this modulation mask amplifies the mid to high spatial frequencies while attenuating the low spatial frequencies and the high spatial frequency noise close to ω_l. Figure 3.13 shows a visualisation of this modulation mask, $\omega_{n,m}$, and the lowpass filter, $\mu_{n,m}$.



(a) **(b)**

Figure 3.13: ***(a)*** *Visualisation of the combination of the lowpass filter, $\mu_{n,m}$, and the modulation mask, $\omega_{n,m}$.* ***(b)*** *A line profile through the centre of combination mask, $\mu_{n,m}\omega_{n,m}$. These are presented as dimensionless masks since the exact size of the mask, $n \times m$ may vary, and the height of the line profile depends on the normalisation factor, β.*

Applying these modifications to Equation 3.17 yields the image quality metric:

$$S = \sum_{n,m} \mu_{n,m}\tau_{n,m}\omega_{n,m} \left\|\tilde{\mathbf{D}}_{n,m}\right\|^2, \tag{3.23}$$

Where $\mu_{n,m}$, $\tau_{n,m}$ and $\omega_{n,m}$ are defined as in Equations 3.19, 3.20 and 3.22 respectively and $\tilde{\mathbf{D}}_{n,m}$ is defined as before. In practice, S measures the total power of the sample spatial frequencies, with increased sensitivity to mid to high spatial frequency changes. As such, this image quality metric is called the Fourier Power metric. As previously mentioned, SIM imaging depends on high quality spatial frequency information[98, 100]. Since the Fourier Power imaging metric maximises the intensity of the mid-high spatial frequency content, this image quality metric is particularly well suited to correcting aberrations for SIM data.

Chapter 4

Aberration Correction for Spinning Disk Confocal Microscopy

4.1 Aberrations and Image Formation

Section 1.3 has already discussed the origin of optical aberrations and their effect on image formation for conventional imaging techniques. Such effects are still relevant and degrade the image quality in the Aurox Clarity system. In addition, in the excitation path aberrations have the effect of blurring the disk image on the sample which results in a loss of contrast and axial resolution due to reduction in spatial frequency information[120, 144]. In the emission path, the fluorescence signal of the sample is similarly degraded leading to a reduction of the signal in both I_T and I_R, hence a reduction in the SNR of I_{conf}.

4.2 Biological Exemplar

To demonstrate the improvement in image quality adaptive optics provides in the Aurox Clarity system, we utilise two samples from *Drosophila melanogaster*; neuro-muscular junctions, NMJ, and egg chambers.

4.2.1 Sample preparation

4.2.1.1 Neuro-muscular Junction

The *Drosophila melanogaster* neuro-muscular junction (NMJ) samples were prepared by Ms Dalia Sara Gala according to the following protocol. 3rd instar *Drosophila melanogaster* larvae (Oregon-R strain) were dissected in HL3 buffer with $0.3mM$ Ca^{2+} to prepare a larval fillet. After this, larvae were fixed with 4%

paraformaldehyde and blocked using 1% BSA.[145] Larvae were stained overnight with 1:100 Horseradish Peroxidase (HRP) conjugated to Alexa568 fluorophore to visualise the neurons, and primary mouse antibody against Discs large (DLG) to visualise the postsynaptic density. The next day, the larvae were counterstained with secondary antibody to detect the DLG (1:200 donkey anti-mouse conjugated to Alexa488 fluorophore was used), as well as 1:1000 from 1mg/mL stock DAPI to visualise the nuclei. The larvae were then washed and mounted in 65% vectashield[145]. This dilution of vectashield is compatible with the AMEP4694 60×, 1.42 NA oil immersion lens.

4.2.1.2 Egg chambers

The *Drosophila melanogaster* egg chamber samples were prepared by prepared by Dr Richard Parton according to the following protocol. Ovaries were isolated from *Drosophila melanogaster* adult females straight into fixation medium and fixed in 4% PFA (prepared fresh from a stock solution of 16% paraformaldehyde, methanol free ultra - pure EM grade, Polysciences) in Cytoskeleton Buffer for 10 minutes without added detergent[146, 147, 148]. Ovaries were then heptane permeabilised with 800μl heptane and post fixed in 4% PFA in PBS for not more than 15 minutes, then washed three times with PBS/TX-100, 0.05%. Actin was labelled with phalloidin Alexa 488 Phalloidin: stock 200 units/ml in Methanol, 6.6 μM) at between 5 and 20 μl stock in 200 μl for at least 45 min at RT (or O/N at 4°C). Labelled ovarioles were washed three times with PBS TX-100, 0.05%, and then finally with PBS before being pre-incubated at RT for at least 3 hours in 70% Vectashield. This was removed and replaced with fresh 70% Vectashield prior to samples being mounted under a coverslip raised on two thin strips of double-sided sticky tape to avoid flattening[149]. The edges of the coverslips were double varnished, and slides were stored at 4°C until use.

4.3 Experimental Results

The same aberration modes were corrected for all the results presented. These are oblique and vertical astigmatism, vertical and horizontal coma and primary spherical, corresponding to Noll indices 5, 6, 7, 8 and 11 respectively[73]. These are the low order optical aberrations whose effects are particularly detrimental to image quality. For example, spherical aberration has been shown to reduce peak intensity by 40% at a focal plane 20μm deep compared to a focal plane 10μm deep

in homogeneous media[144]. The effect is likely to be more pronounced in heterogenous media such as biological tissue. To show the effectiveness of aberration correction throughout the sample, the sensorless adaptive optics correction routine described in Section 3.2.1 was performed at multiple depths in the neuro-muscular junction samples. Figure 4.1 shows the results of these corrections. At all imaging depths, aberration correction yields an improvement in both contrast and overall image intensity. This improvement in image quality reveals biological structures which, without correction, are not visible. Overall intensity does decrease with imaging depth. This is likely due to a combination of varying marker density throughout the sample, residual aberration and loss of signal through absorption or scattering as the light passes through more tissue.

Since the egg chambers samples were fixed and cleared, the sample induced aberrations were considerably less severe over a larger Z range. Figure 4.2 shows maximum intensity projections of 36μm Z-stacks obtained at high optical sectioning (0.9 μm), both without and with aberration correction. Ovarioles were separated out to better visualise individual egg-chambers Once again the overall contrast and intensity are improved with aberration correction. This is most noticeable with the actin associated with ring-canals. Ring-canals are pores which connect the oocyte to adjacent nurse cells, which supports oocyte growth[150]. In many of the cases highlighted in Figure 4.2 with the arrows, the ring structure of these ring-canals is not visible without aberration correction.

Finally, Figure 4.3 shows maximum intensity projections of 20μm Z-stacks obtained at high optical sectioning, both without and with aberration correction. Despite the sensorless adaptive optics routine being performed only using the data from the Alexa568 (HRP) channel, improvements in intensity and contrast are observed in all imaging channels. Notably, the aberration correction allows for individual fibres in the segmental nerve to be resolved, shown in the middle row of Figure 4.3. Without aberration correction the structure of individual round postsynaptic densities, boutons, are either unclear or not visible, shown in the bottom row of Figure 4.3. Once the sample induced aberrations have been corrected, the structure of these boutons becomes clearer and the presence of several new, previously obscured, boutons can be observed.

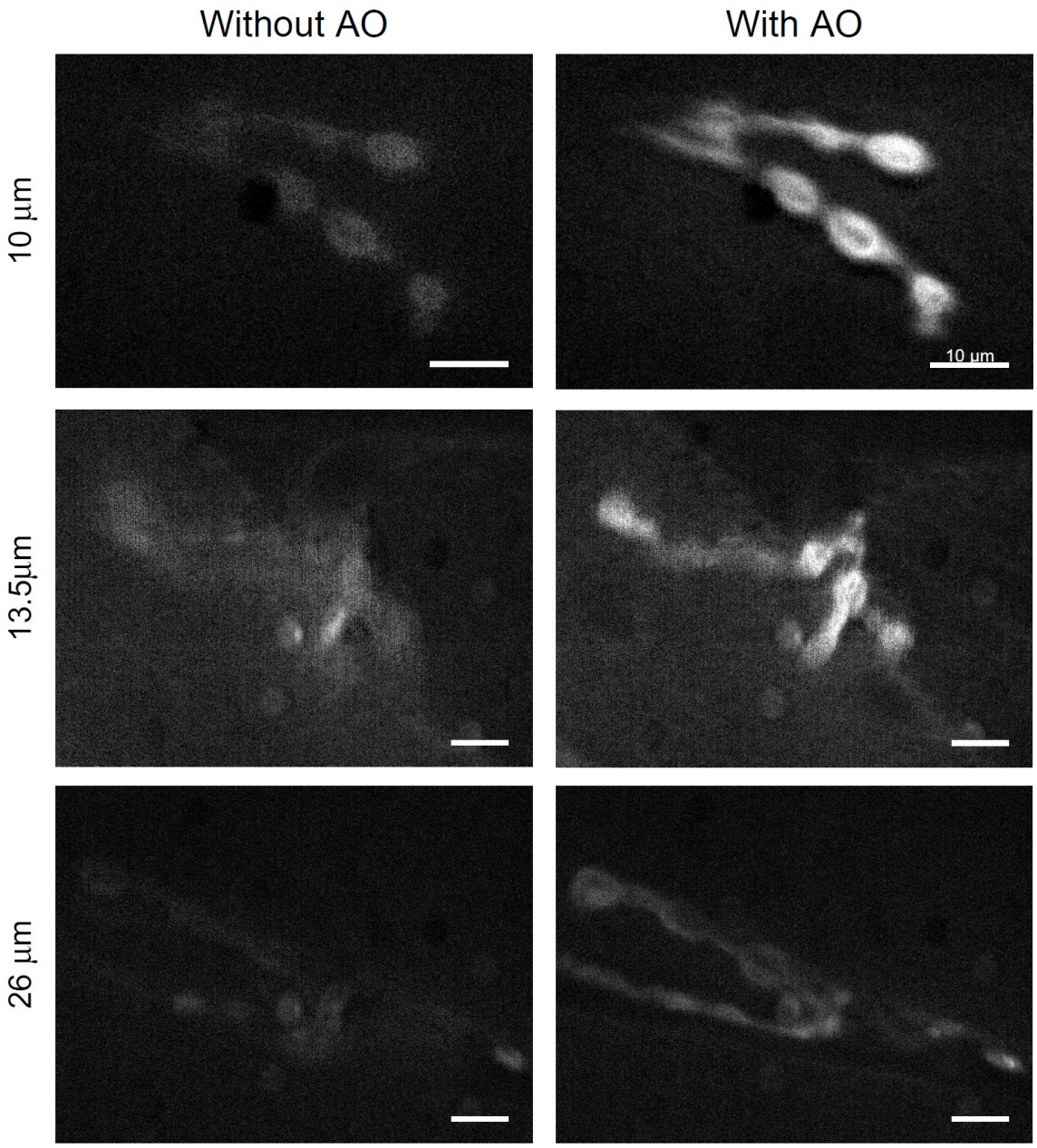


Figure 4.1: *Neuro-muscular junction images acquired at 10µm, 13.5µm and 26µm with high optical sectioning. The images are of single Z-positions. Aberration correction yields improvements in signal and contrast at all depths. Scale bars are all 10µm. Discs large (DLG) counterstained with secondary antibody to detect the DLG (donkey anti-mouse conjugated to Alexa 488 fluorophore) is shown. All images are displayed on the same intensity scale.*

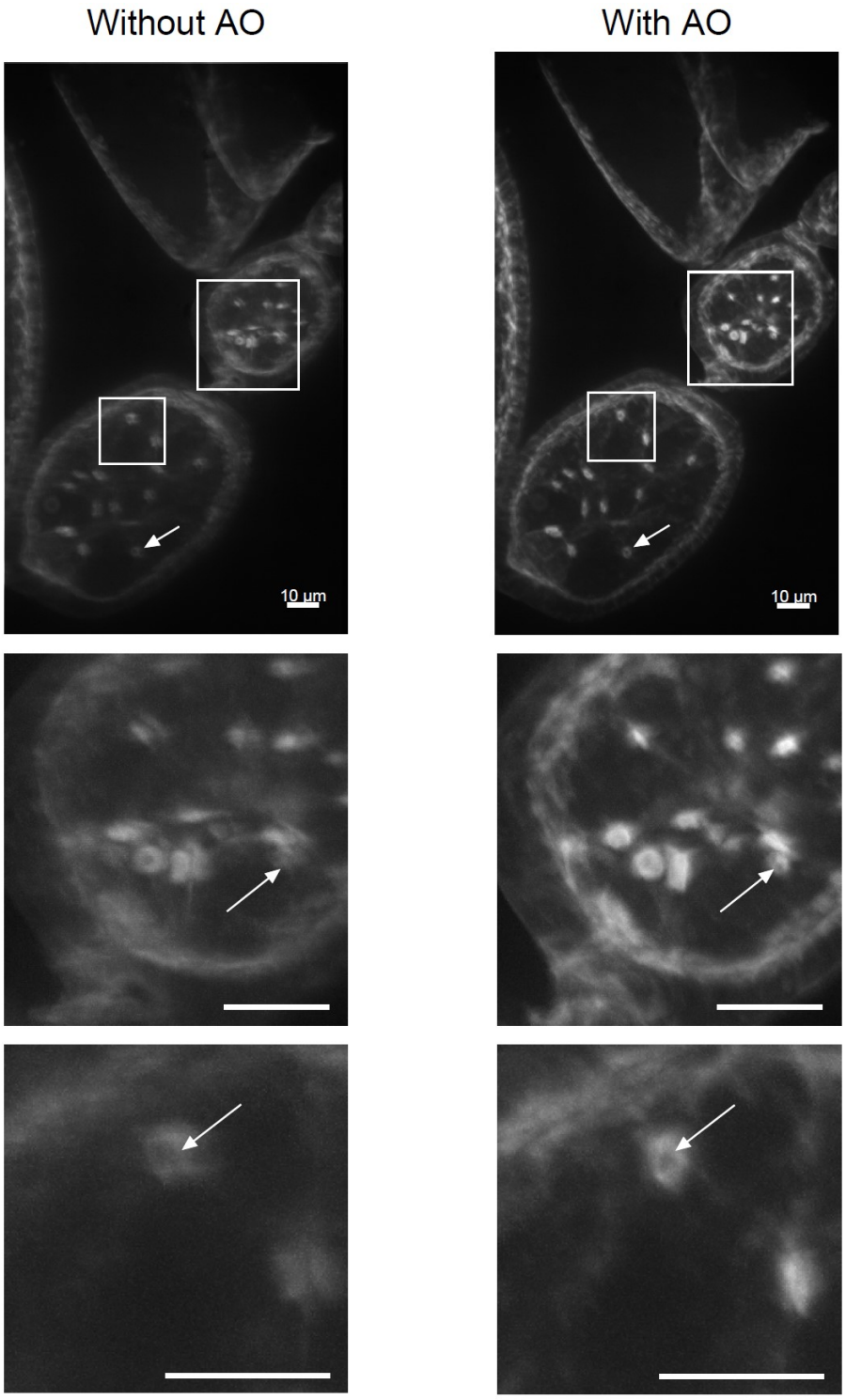


Figure 4.2: *Maximum intensity projections of 36µm Z-stacks of egg chamber samples acquired without (left) and with (right) adaptive optics correction at high optical sectioning. The overall intensity and contrast are improved after correction. The arrows highlight particularly notable areas of improvement where fine details, such as the outline of ring canals, become clearly visible. Scale bars are all 10µm. Actin (labelled with phalloidin Alexa 488) signal is shown. All images are displayed on the same intensity scale.*

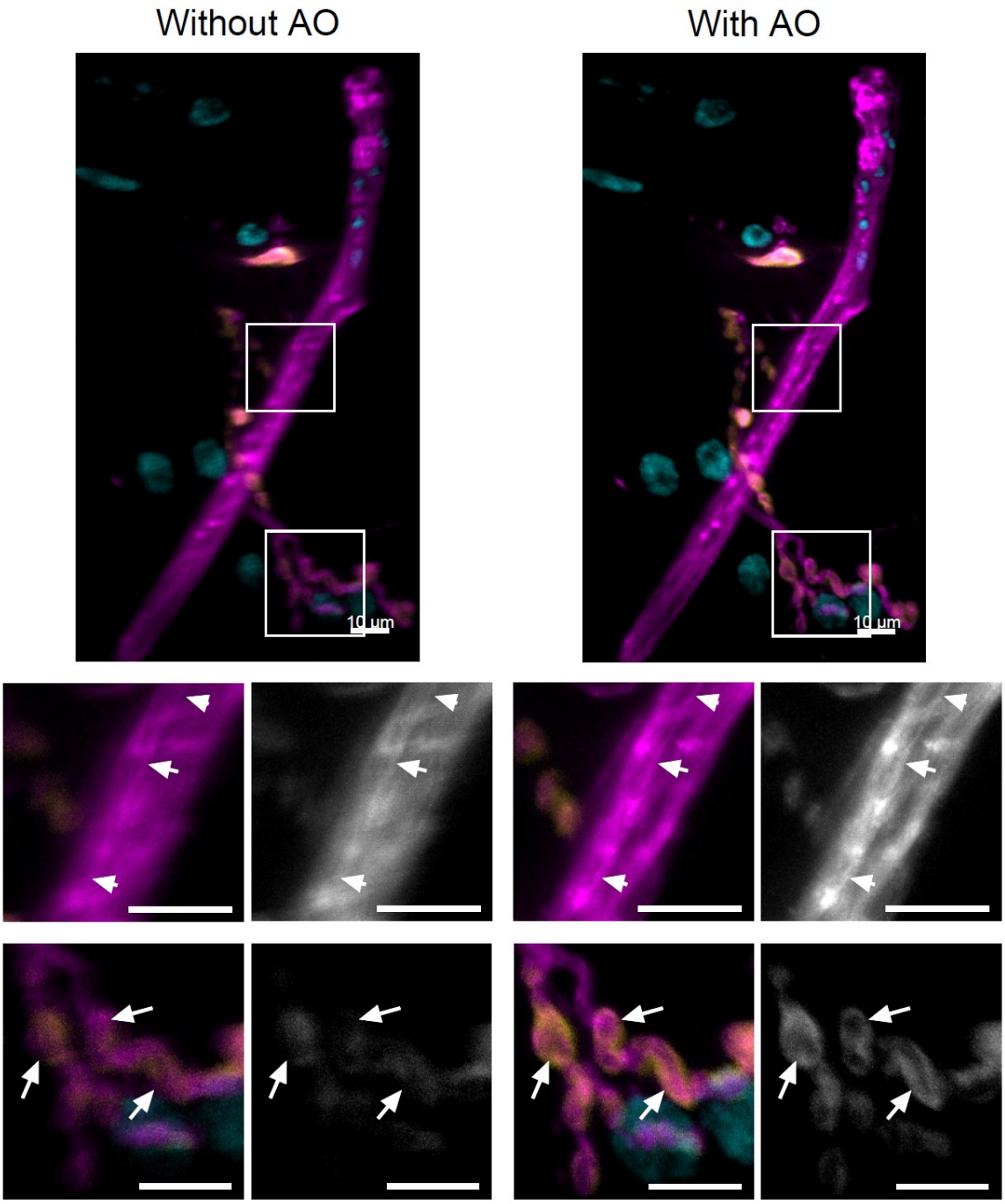


Figure 4.3: *Maximum intensity projections of 20µm z-stacks of neuro-muscular junction samples acquired without (left) and with (right) AO correction at high optical sectioning. Discs large (DLG) counterstained with secondary antibody to detect the DLG (donkey anti-mouse conjugated to Alexa 488 fluorophore) is shown in yellow. Horseradish Peroxidase (HRP) (conjugated to Alexa 568 fluorophore) to visualise the neurons is shown in magenta, nuclei shown in cyan. Middle row greyscale images show only HRP. Bottom row greyscale images show only DLG. The overall intensity and contrast are improved after correction. The arrows highlight particularly notable areas of improvement where fine details, such as individual nerve fibres, become clearly visible. Scale bars are all 10µm. All images are displayed on the same intensity scale.*

Chapter 5

Enabling Structured Illumination Microscopy at greater depth

5.1 Sample Induced Aberrations in Structured Illumination Microscopy

The origin of optical aberrations and their effect on image formation from a geometric optics standpoint and how this leads to decreased image quality and resolution has already been covered in Section 1.3. The extent of optical aberrations in thick samples and the particular effects of aberrations on structured illumination microscopy (SIM) imaging are worth paying attention to.

In widefield microscopy, an even field of illumination is applied to the field of view and the resultant fluorescent signal from the sample is measured. In SIM, this even illumination is replaced by a sinusoidally varying illumination pattern. Multiple images with variations to the angle and phase shift to the illumination pattern are acquired. These images are then used to reconstruct a single super-resolved image[49, 59]. Recall a single fluorescent image, $F(\mathbf{r})$, is defined by:

$$\begin{aligned} F(\mathbf{r}) &= (E \circledast H)(\mathbf{r}) \\ F(\mathbf{r}) &= [D(\mathbf{r})I(\mathbf{r})] \circledast H(\mathbf{r}), \end{aligned} \tag{1.12}$$

where $D(\mathbf{r})$ is the sample fluorescence distribution, $I(\mathbf{r})$ is the illumination pattern, $E(\mathbf{r})$ is the resultant emission signal and $H(\mathbf{r})$ is the system point spread function (PSF). Section 1.3 has already discussed the effect aberrations have on distorting the system PSF, $H(\mathbf{r})$. However, in SIM imaging the illumination pattern,

$I(\mathbf{r})$, is also formed in the same imaging path and therefore the illumination pattern formation is also affected by aberrations.

Consider the illumination pattern function. Fully coherent illumination conditions yield optimum imaging performance and are therefore chosen. In practice, only partially coherent conditions are achievable. Utilising the fully coherent approximation, $I(\mathbf{r})$ can be expressed as:

$$I(\mathbf{r}) = \left\| \frac{1}{2}[1 + \cos(\mathbf{r} \bullet \mathbf{p} + \phi)] \circledast H_{amp}(\mathbf{r}) \right\|^2, \tag{5.1}$$

where $\mathbf{p}$ and ϕ define the orientation and phase of the illumination pattern respectively. $H_{amp}(\mathbf{r})$ is the amplitude PSF - as opposed to $H(\mathbf{r})$ which is the intensity PSF - and is defined as:

$$H_{amp}(\mathbf{r}) = \mathcal{F}[P(\mathbf{r}')], \tag{5.2}$$

where P is the pupil function, $\mathbf{r}'$ is the coordinate vector in the pupil plane and $\mathcal{F}$ is the Fourier transform operation. Utilizing the Fourier convolution theorem, Equation 5.1 becomes:

$$I(\mathbf{r}) = \left| \mathcal{F}^{-1} \left\{ \frac{1}{2} \left[\delta(\mathbf{r}') + \frac{\exp^{-i\theta}}{2} \delta(\mathbf{r}' - \mathbf{p}) + \frac{\exp^{i\theta}}{2} \delta(\mathbf{r}' + \mathbf{p}) \right] P(\mathbf{r}') \right\} \right|^2, \tag{5.3}$$

where value of $\mathbf{p}$ positions the delta functions in the pupil plane. $\mathbf{p}$ is chosen to have a value of or close to 1, to maximise the resolution increase. Equation 5.3 shows there is clearly only illumination at three points in the pupil plane, at the centre and diametrically opposed at the edge of the pupil i.e. the location of the 3 delta functions. There are two principle consequences of this fact. Firstly, since the illumination only exists at the centre and edges of the pupil plane, the illumination pattern is only affected by phase variations at those points. Therefore, the illumination pattern should be immune to aberrations with little phase variation at the edges of the pupil. Secondly, rotationally symmetrical aberrations, such as spherical aberration, have the main effect of refocusing the illumination pattern[99].

It has also been shown that the imaging properties of a SIM system and the quality of the reconstructed super-resolution images are determined by the system's ability to reliably image the high spatial frequencies[98, 100]. The aberrations which affect the strength of high spatial frequency signals can be divided into two categories: isoplanar and anisoplanar aberrations. In this context, isoplanar

aberrations are aberrations which are constant over the imaging field of view. Anisoplanar aberrations are, intuitively, ones which vary over the field of view. Single adaptive elements, such as the deformable mirror in the DeepSIM setup, can only correct for the isoplanar aberrations. Anisoplanar aberrations will still introduce artifacts in the final, reconstructed data. However, provided that the anisoplanar aberrations are considerably smaller than the isoplanar aberrations, the effect of these aberrations will be small and will not prevent a successful reconstruction[100].

The cumulative effect of the optical aberrations is that traditional SIM imaging is limited in its imaging depth to approximately $10 - 20\mu m$[45, 61]. However, correcting the optical aberrations present would not yield an infinite depth of imaging due to a multitude of issues such as increased scattering of photons with depth, photon absorption, optical working distances, laser coherence length, etc. Nonetheless, by correcting for optical aberrations present DeepSIM offers the potential to acquire super-resolution SIM images at an unprecedented depth.

5.2 IsoSense

Anisotropies in the sample fluorescence distribution can bias the corrections towards improving the image quality in a non-uniform manner. There has recently been a technique developed to overcome this issue; IsoSense[151]. It relies on producing spatially structured light in order to fill empty sections of the image Fourier spectrum. IsoSense is designed to be used in SIM setups since they often incorporate spatial light modulators (SLM) as high-speed, dynamic diffraction gratings and SIM is particularly sensitive to Fourier space anisotropies. This technique was developed by Dr Mantas Žurauskas. Previously, a bespoke LabView implementation which was not integrated into the rest of the microscope control framework, and an user experienced in adaptive optics were required to successfully implement this technique.

Microscope-AOtools incorporates the methods necessary for a general user to implement IsoSense and is integrated into the Microscope Cockpit UI. Figure 5.1 shows both the structured illumination pattern applied to the SLM and the location of the beams in Fourier space. The illumination pattern shown in Figure 5.1a is the inverse Fourier transform of the 4-beam interference pattern in Figure 5.1b. The location of these beams, κ, are: $(0,0)$, $(0,\gamma\omega_l)$, $(0,-\gamma\omega_l)$, $(\gamma\omega_l,0)$, $(-\gamma\omega_l,0)$, $(\frac{\gamma\omega_l}{2},\frac{\gamma\omega_l}{2})$, $(-\frac{\gamma\omega_l}{2},\frac{\gamma\omega_l}{2})$, $(\frac{\gamma\omega_l}{2},-\frac{\gamma\omega_l}{2})$, $(-\frac{\gamma\omega_l}{2},-\frac{\gamma\omega_l}{2})$. ω_l is the lateral diffraction limit

in reciprocal space as per Equation 1.8 and γ is a user defined fill fraction, where γ has a range $[0, 1]$. This fill fraction controls the positions of the beams in the interference pattern and hence the region of the Fourier spectrum which will be enhanced over normal illumination. The resultant emission image obtained, $E(\mathbf{r})$, can be described as:

$$E(\mathbf{r}) = D(\mathbf{r}) \times I(\mathbf{r}), \tag{5.4}$$

where $I(\mathbf{r})$ is the interference pattern, similar to that shown in Figure5.1a, $D(\mathbf{r})$ is the sample fluorescence distribution as before and $\mathbf{r}$ is the spatial coordinate vector. Applying a Fourier transform yields:

$$\begin{aligned} \mathcal{F}[E(\mathbf{r})] &= \mathcal{F}[D(\mathbf{r}) \times I(\mathbf{r})] \\ \tilde{\mathbf{E}}(\mathbf{k}) &= \tilde{\mathbf{D}}(\mathbf{k}) \circledast \tilde{\mathbf{I}}(\mathbf{k}) \\ \tilde{\mathbf{E}}(\mathbf{k}) &= \sum_{\kappa} \iint \tilde{\mathbf{D}}(\mathbf{k}) \delta(\mathbf{k} - \kappa) du dv \\ \tilde{\mathbf{E}}(\mathbf{k}) &= \sum_{\kappa} \tilde{\mathbf{D}}(\mathbf{k} - \kappa), \end{aligned} \tag{5.5}$$

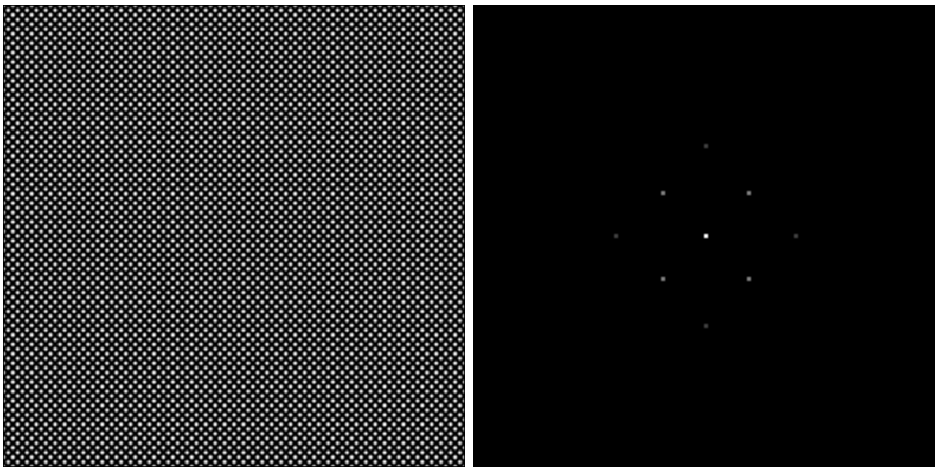
where bold text and $\sim$ indicates the Fourier transform of the respective real-space functions, the κ frequencies are the locations of interference pattern beams described above and $\mathbf{k}$ is the spatial frequency vector. By convolving the sample fluorescence distribution with multiple δ-functions, multiple copies of the sample spatial frequency information are created and regions of the system OTF left unfilled by sample fluorescence distribution anisotropies are filled, leading to improved sampling of the system OTF particularly at high spatial frequencies close to ω_l and greater aberration sensitivity[151].

5.3 Experimental Setup

As previously noted in Section 1.2.1, the theoretical resolution extension factor for a diffraction limited SIM system is given by:

$$\alpha_l = \frac{\left(\frac{1}{\lambda_{ex}} + \frac{1}{\lambda_{em}}\right)}{\frac{1}{\lambda_{em}}} = 1 + \frac{\lambda_{em}}{\lambda_{ex}}. \tag{1.21}$$

There are two complicating factors. Firstly, as mentioned in Section 1.1.1, fluorescent proteins do not present a single wavelength of emission, λ_{em} but rather have an emission spectrum. For simplicity, the peak of the emission spectrum is



(a) **(b)**

Figure 5.1: *IsoSense pattern visualisation.* ***(a)*** *A simulated IsoSense pattern created with a 4-beam interference. A pattern similar to this is applied to the SLM* ***(b)*** *A diagram of a 4-beam interference pattern in Fourier space. The diagonal axis and the horizontal/vertical axis have $\frac{1}{2}$ and $\frac{1}{4}$ of the intensity of the central beam respectively.*

used to calculate the resolution extension. Secondly, Equation 1.21 assumed that the locations of the $m = \pm 2$ Fourier components of the illumination pattern are placed at $|\mathbf{k}| = \frac{1}{\lambda_{ex}}$. This is not necessarily the case. As such, an accurate measure of the theoretical resolution extension factor for a practical SIM implementation is given as:

$$\alpha_l = \frac{\left(\frac{1}{\lambda_I} + \frac{1}{\lambda'_{em}}\right)}{\frac{1}{\lambda'_{em}}} = 1 + \frac{\lambda'_{em}}{\lambda_I}, \tag{5.6}$$

where $\lambda'_{em}$is the wavelength of the peak of the emission spectrum and λ_I is the stripe width of the illumination pattern. For DeepSIM, the conventional resolution limit for the green and red channels respectively is 291nm and 338nm, utilising the Rayleigh criterion from Equation 1.3 for wavelengths 525nm and 610nm respectively. The stripe width was 322nm and 367nm for 488nm and 561nm excitation wavelengths respectively.

5.4 Biological Exemplar

To demonstrate both the improvement in image quality adaptive optics provides in the DeepSIM system and the viability of an upright configuration for live-sample,

open-dish imaging, we utilise the live *Drosophila melanogaster* neuro-muscular junction (NMJ) sample.

5.4.1 Sample preparation

The samples were prepared by were prepared by Ms Dalia Sara Gala according to the following protocol.[145]. 3rd instar *Drosophila melanogaster* larvae (Bruchpilot (Brp)-GFP strain) were dissected in HL3 buffer with 0.3mM Ca^{2+} to prepare a larval fillet, and the larval brains were removed. After this, larvae were stained for 15 minutes with 1:50 Horseradish Peroxidase (HRP) conjugated to Alexa568 fluorophore to visualise the neurons, washed with HL3 buffer with 0.3mM Ca^{2+} and imaged in HL3 buffer with 0mM Ca^{2+} to prevent the larvae from moving.

5.5 Experimental Results

To verify both that the system is capable of achieving super-resolution and that Microscope-AOtools is capable of correcting for optical aberrations, an Argolight SIM slide was imaged. The Argolight SIM slide is a commercially available slide provided by Argolight. It consists of several different fluorescent patterns are embedded inside a special glass substrate. They are designed for assessing and following the performances of fluorescence-based imaging systems.[152]

The structure chosen for imaging was a set of pairs of 36μm-long horizontal lines pairs lines with gradually increasing spacing, from 0 to 390nm, with a step of 30nm. This structure was chosen for two principal reasons. Firstly, the known separation of the fluorescent structures allows for an accurate gauge of the system resolving power. The structure was excited at 488nm and measured with a peak emission wavelength of 610nm. Therefore, utilising Equation 5.6 the diffraction limited lateral resolution in a SIM reconstruction would be 161nm i.e. the first 6 separations should not be resolvable. Secondly, the refractive index of the Argolight slide at 488nm is 1.53 and the structures are positioned at 170μm below the top glass surface[152]. This represents a significant source of optical aberrations, primarily spherical aberration, which would degrade the image quality and decrease resolution in the absence of AO correction.

Figure 5.2 shows both the maximum intensity projection of 13μm SIM z-stacks and a xz slice at the midpoint of the y-axis. In both datasets, the 150nm separation is resolvable, which is slightly better than the anticipated lateral resolution. The

150nm line pair is marked in Figures 5.2a and 5.2b with arrows. This is not entirely surprising as the Argolight sample is a highly fluorescent, regular structure with very little out-of-focus fluorescence to compromise the image quality. As mentioned in Section 1.1.2, the assumptions used to estimate the lateral resolution leave a number of factors unaccounted for and mainly provide a useful estimate[32]. For a structure such as that present in the Argolight slide, a slight over-performance is normal. There are significant artifacts present in the dataset without AO correction which makes line pairs with separations greater than 150nm unresolvable in places. The z length of the structures in the xz slice is also extended and shows significant artifacts, primarily "echo" structures above the true fluorescent structures. Additionally, the dataset without AO correction has half the intensity of the dataset with AO correction and must be displayed on a reduced dynamic range for visibility. Applying the AO correction recovers the fluorescent signal and removes these artifacts. The spherical aberration mismatch measurements obtained from the ImageJ plugin SIMCheck in Figures 5.2c and 5.2d confirms that the AO has successfully removed the majority of the spherical aberration present[153].

For the NMJ imaging, the sensorless correction routine detailed in Section 3.2.1 using the Fourier Power image quality metric described in Section 3.2.2 was used since it is well suited to maximising the spatial frequency content essential to SIM imaging. The aberrations corrected were: primary and secondary spherical, oblique and vertical astigmatism, vertical and horizontal coma, and oblique and vertical trefoil - corresponding to Noll indices 11, 22, 5, 6, 7, 8, 9, and 10. These modes were corrected in the order listed here. They were corrected with the IsoSense pattern applied to the SLM. The range of amplitudes applied was [-1.5 radians, 1.5 radians] over 9 images, with 2 iterations for a total of 144 images for a complete correction routine. These variables were specified in the dialogue box shown in Figure 3.1d.

Figure 5.3 shows maximum intensity projections of 12.75μm z-stacks obtained with the centre of the stack $\sim$ 20μm deep in the sample, both without and with aberration correction. Despite the sensorless adaptive optics routine being performed only using the data from the red imaging channel, improvements in intensity and contrast are observed in both imaging channels. Much of the neuron membrane, visualised with HRP conjugated to Alexa568, is not visible without AO correction. Almost all of the Brp, endogenously labelled with GFP, is extremely dim or invisible without AO correction. The insets in Figures 5.3c - 5.3h show

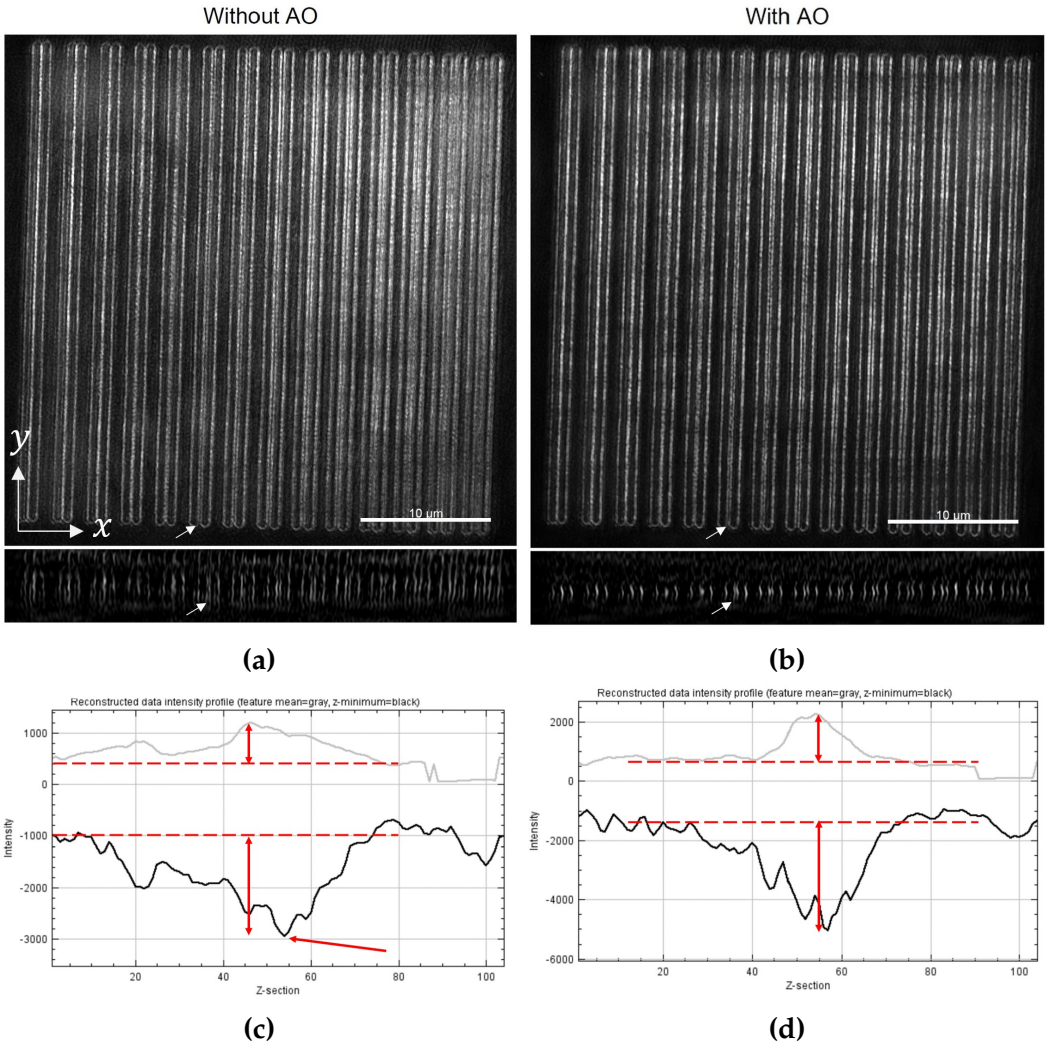


Figure 5.2: *Argolight slide data. Both* ***(a)*** *without AO correction and* ***(b)*** *with AO correction datasets are maximum intensity projection of* 13*µm SIM z-stacks (top) and a xz slice at the midpoint of the y-axis (bottom). Without AO correction data is displayed with half the maximum intensity level of data with AO correction for clarity.* 150*nm line pair marked with an arrow The spherical aberration mismatch from the SIMCheck ImageJ plug-in[153] is shown* ***(c)*** *without AO correction and* ***(d)*** *with AO correction*

subsections of the dataset where structures which are invisible or of poor contrast without AO correction become visible.

From Equation 5.6, the diffraction limited lateral resolution in a SIM reconstruction would be 151nm and 175nm for the GFP and Alexa568 channels respectively, assuming structures of such size exist in the dataset. Figure 5.4 shows the Fourier Transform Lateral (FTL) and Fourier Transform Radial (FTR) of the central z-slice obtained from the SIMCheck ImageJ plug-in[153]. The red dashed lines in the FTR figures show the point where the signal Fourier information is no longer above the Fourier noise, which here is used as a proxy for lateral resolution limit of the dataset. Without AO correction this is 179nm and 192nm for the GFP and Alexa568 channels respectively. With AO correction this is 168nm and 188nm for the GFP and Alexa568 channels respectively.

Despite the sensorless AO correction being performed on the Alexa568 channel, only a moderate resolution improvement is observed. Taken together with the results from the Argolight slide and the overall contrast improvement with AO correction, it is reasonable to conclude that the smallest structures in the Alexa568 channel are $\sim$ 165-170nm. A more substantial improvement in resolution is observed the GFP channel. The fact that both channels benefit from the applied correction despite it being acquired from image quality measurements from only one channel implies that a significant portion of the aberrations present are broadly achromatic.

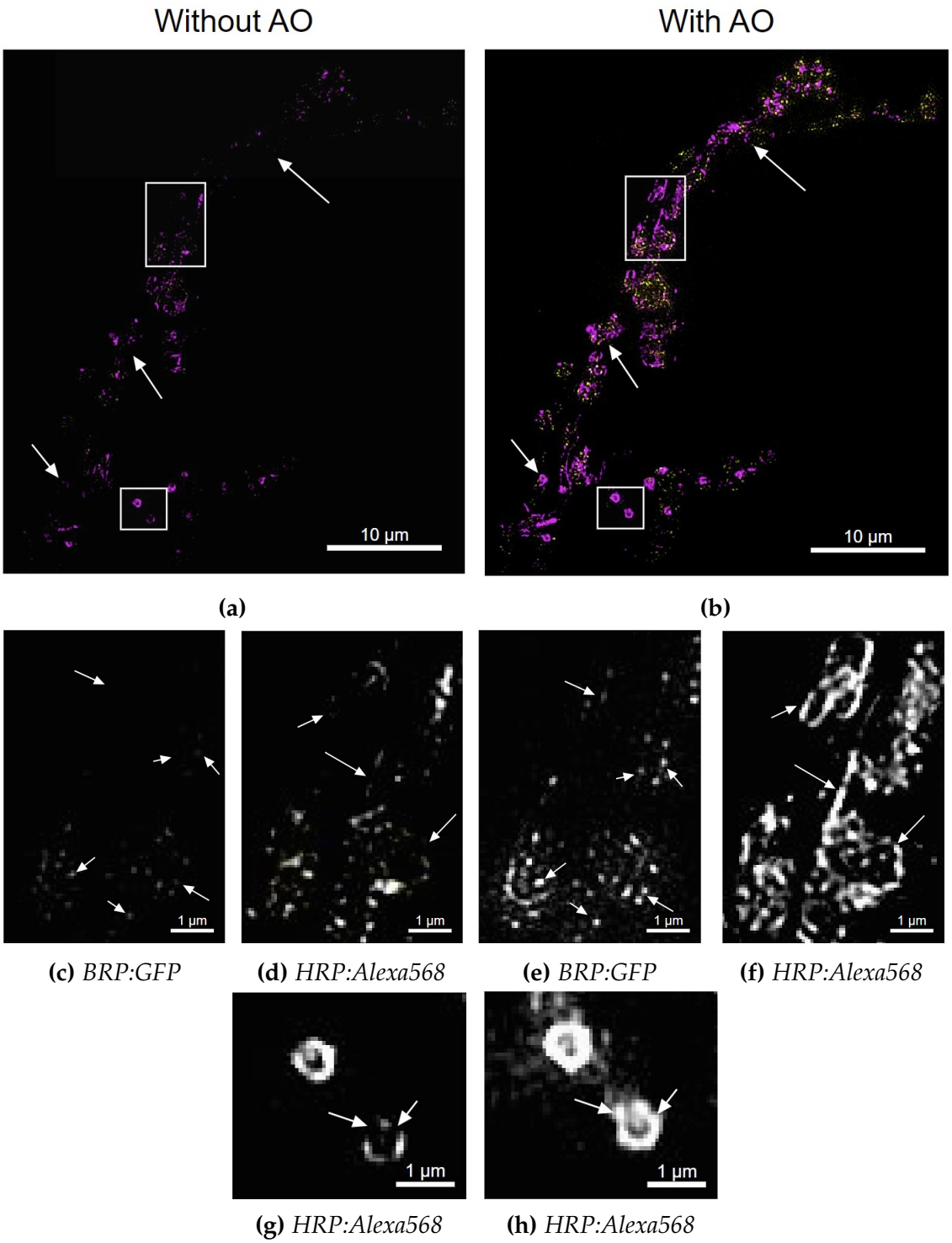
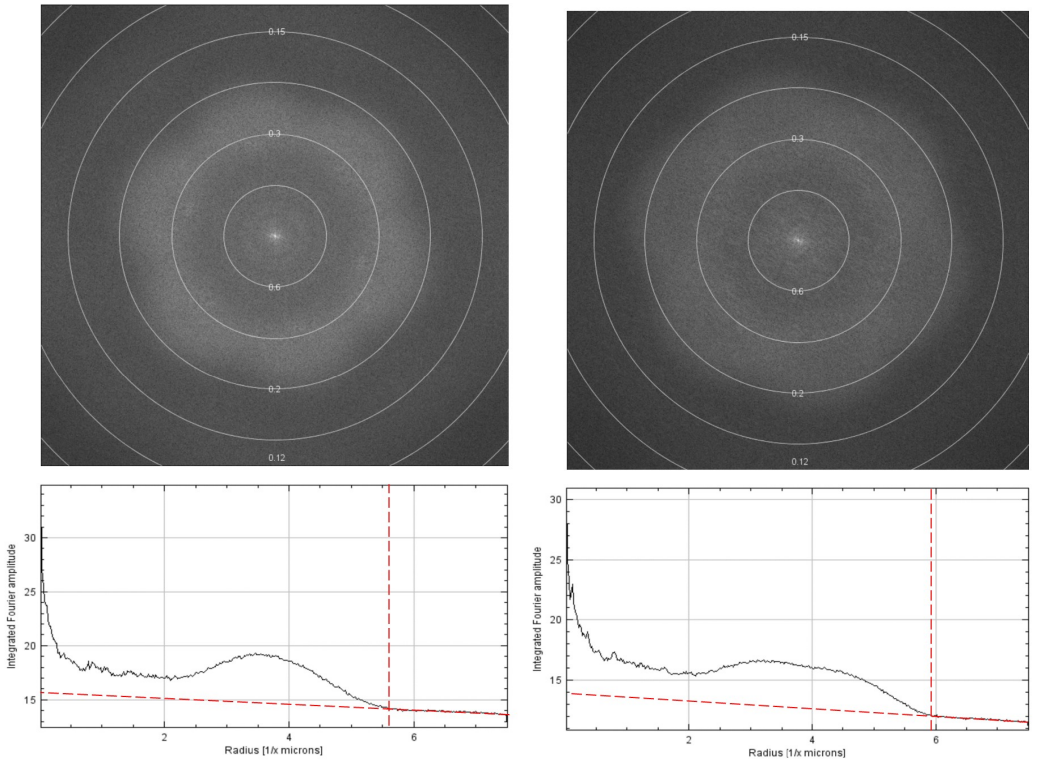
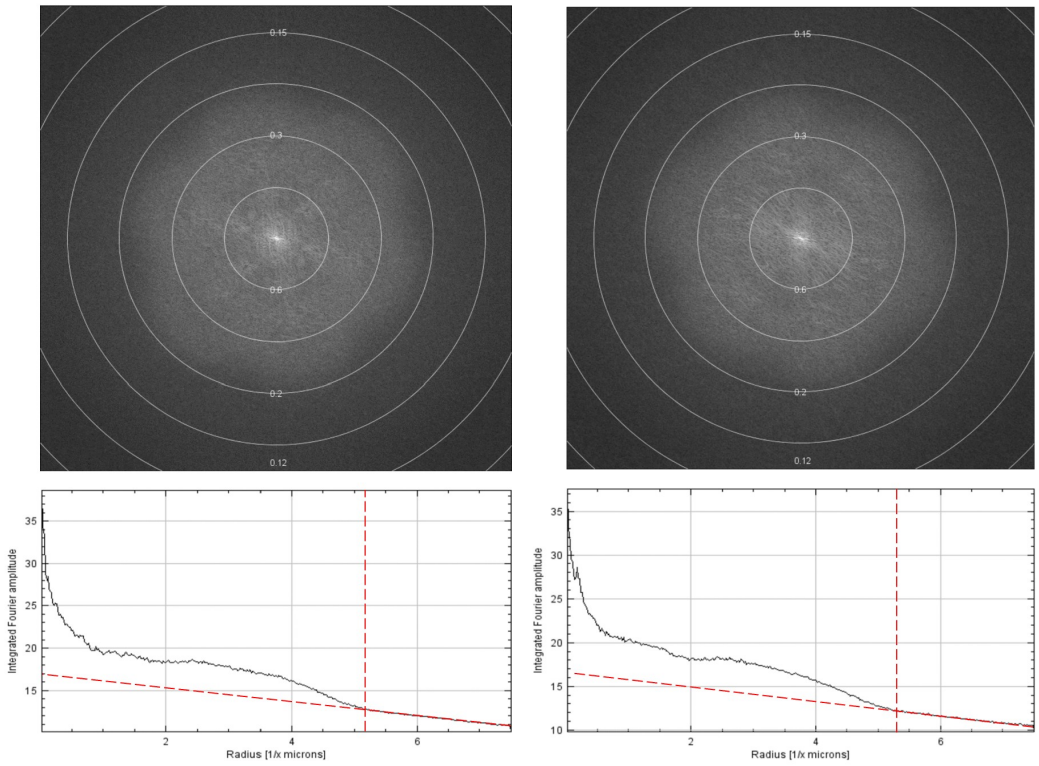


Figure 5.3: *Maximum intensity projections of 12.75µm z-stacks of neuro-muscular junction samples acquired without (left) and with (right) AO correction. Bruchpilot (Brp), endogenously labelled with GFP, is shown in yellow. Horseradish Peroxidase (HRP), conjugated to Alexa568 fluorophore to visualise the neuron, is shown in magenta. The arrows highlight particularly notable areas of improvement where fine details, such as individual puncta, become clearly visible. All images are displayed on the same intensity*



(a) *Without AO, green channel* **(b)** *With AO, green channel*



(c) *Without AO, red channel* **(d)** *With AO, red channel*

Figure 5.4: *Fourier plots of Drosophila neuro-muscular junction data acquired on the DeepSIM imaging system. Each subplot shows the Fourier Transform Lateral (FTL) (top) and Fourier Transform Radial (FTR) (bottom) of the central z-slice from the SIMCheck ImageJ plug-in[153] for* ***(a)*** *green channel without AO correction* ***(b)*** *green channel with AO correction* ***(c)*** *red channel without AO correction* ***(d)*** *red channel with AO correction. Green channel used for imaging Bruchpilot (Brp), endogenously labelled with GFP. Red channel used for imaging Horseradish Peroxidase (HRP), conjugated to Alexa568 fluorophore*

Chapter 6

Discussion

Chapter 3 details the robust and generalised nature of Microscope-AOtools as well as its accessible implementation within the Microscope-Cockpit UI. The results in Sections 4.2 and 5.4 demonstrate significantly improved image quality and resolution, most notably in deep in challenging, live samples as shown in Section 5.4. However, no implementation is without limitations and it is worthwhile spending some time discussing them.

6.1 Limitations of Microscope-AOtools

6.1.1 Zernike mode fitting accuracy

Many the setup methods for Microscope-AOtools outlined in Section 3.1 and the direct wavefront correction outlined in Section 3.1.5 rely on the Zernike modes generated from the *AOtools* Python package and the method described in Section 3.1.2 to determine the Zernike mode amplitudes present in a phase wavefront[136]. It is therefore worth investigating the accuracy of this fitting for determining the amplitude of Zernike modes present. In theory, measuring the Zernike mode amplitudes present in a wavefront image created with known Zernike mode amplitudes using *AOtools* should be trivial and yield the same Zernike mode amplitudes exactly. Measuring the Zernike mode amplitude present is done using the method described in Section 3.1.2, but in this case the simulated wavefront image created using *AOtools* takes the place of the measured phase wavefront, $\Phi(x, y)$.

The simplest test of the accuracy of the Zernike mode amplitude fitting follows thusly. *AOtools* is used to create a wavefront image with amplitude 1 radian (i.e. $\alpha_j = 1$) of a particular Zernike mode. The Zernike mode amplitudes present in the wavefront image is then measured and the percentage error between the measured

and simulated Zernike mode amplitudes is recorded. This process is repeated 50 times for all Zernike modes up to radial order, $n = 10$. Figure 6.1 shows the results of this experiment on wavefront images of various sizes. In no case is the expected Zernike mode amplitude returned exactly - there is always some degree of error in the Zernike mode amplitude measurement. Zernike modes with an even azimuthal frequency appear to perform either considerably worse or better than Zernike modes with either an odd or zero azimuthal frequency. All non-zero azimuthal frequency Zernike modes display a trend of increasing percentage error with radial order. The magnitude of percentage error also decreases with increasing simulated wavefront size.

Interestingly, there is often a clear split in percentage error between Zernike modes with positive and negative even azimuthal frequencies. This is most visible in Figure 6.1d but it can be observed in some radial orders in all the simulated wavefront sizes shown in Figure 6.1. This observed difference in performance between these Zernike modes occurs because positive even azimuthal frequencies have a component of variation aligned with either the x or y axis whereas negative even azimuthal frequencies do not. Zernike modes with a positive even azimuthal frequencies are vulnerable to a class of discretisation error where some of the principle variation in the simulated wavefront shape falls between pixels and is therefore not captured by the discrete representation of the Zernike mode. Odd azimuthal frequency Zernike modes do not exhibit this splitting since positive and negative odd azimuthal frequencies both have some component of variation along the aligned with either the x or y axis. Therefore, odd azimuthal Zernike modes always suffer from this class of discretisation error. For smaller simulated wavefront sizes, this split in the even azimuthal frequency Zernike modes is less visible at higher radial orders because other, less geometrically determined, discretisation errors dominate the overall percentage error measurements.

A wavefront may be dominated by a single Zernike mode, but they are almost never composed entirely of one Zernike mode. Figure 6.2a shows the mean percentage error in the Zernike mode amplitude measurement for 50 wavefronts, 256×256 pixel size, generated with random amplitudes for Zernike modes up to radial order, $n = 10$. Clearly, having multiple modes present simultaneously adds a degree of variance to the amplitude measurement accuracy as well as an overall increase in the error magnitude.

It is a time-consuming process for *AOtools* to generate wavefront images of sizes greater than 256×256 pixels, typically about a $0.1 - 1$ seconds per image

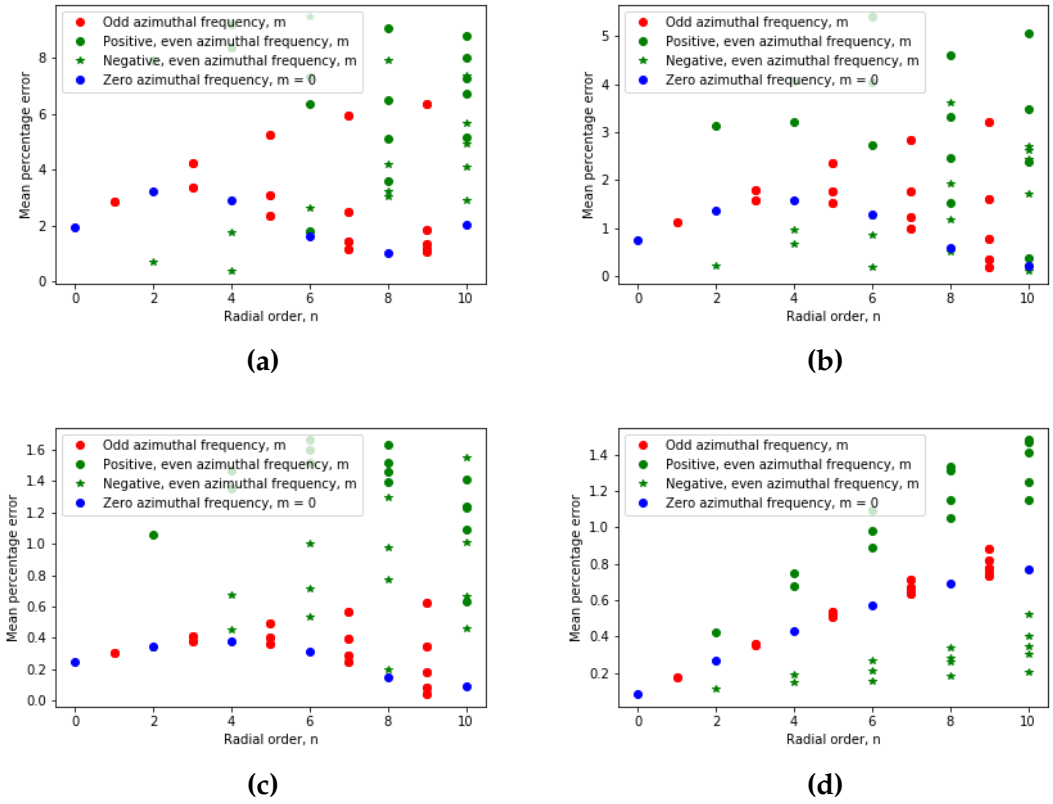


Figure 6.1: *The effect of image size on Zernike mode fitting accuracy. Each subfigure shows the percentage error in the Zernike mode measurement and the linear regression of all Zernike mode measurements for images of size* ***(a)*** 32×32 *pixels* ***(b)*** 64×64 *pixels* ***(c)*** 128×128 *pixels* ***(d)*** 256×256 *pixels*

depending on the overall size and number of Zernike modes simulated. In order to increase the speed of fitting, acquired wavefront images are often resized. This too has an effect on Zernike mode accuracy fitting since the resizing function bins multiple pixels together and takes their mean, effectively smoothing the wavefront. Figures 6.2b-6.2d show the same set of wavefronts used for the results in Figure 6.2a, except that the wavefronts were resized by varying factors prior to the Zernike modes amplitude measurements. Clearly, the resizing factor is inversely proportional to the overall Zernike mode fitting accuracy.

The splitting in fitting error between positive and negative even azimuthal frequencies is once again observed, and it is observed for all resizing factors. A splitting in fitting error is also observed in Figure 6.2 between positive and negative odd azimuthal frequencies which was not present previously. One might suspect that this is due to the order in which the image axes are integrated along using *scipy*'s *trapz* function. However, the error splitting presented in Figure 6.2 between

positive and negative azimuthal frequencies is preserved even when the order in which the axes are integrated along is reversed. Another reasonable candidate for suspicion might be the function used to resize the wavefront. If this were the source of this difference in fitting errors, it should not occur in Figure 6.2a since the simulated wavefronts used in this dataset have not been resized. This difference in fitting errors may be a result of some internal preference within *AOtools' phaseFromZernikes()* function used to generate the simulated wavefronts. Alternatively, this may reflect a genuine preference in the Zernike mode amplitude measurements in complex wavefronts for azimuthal frequencies less than 0.

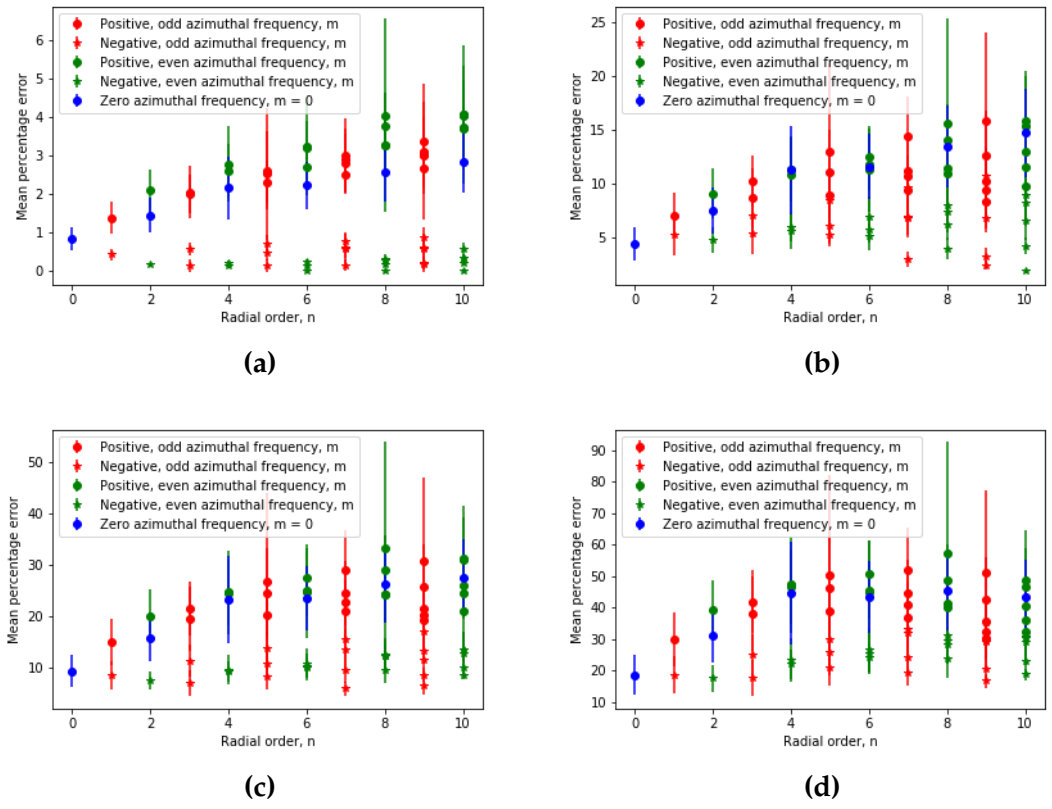


Figure 6.2: *The effect of image resizing on Zernike mode fitting accuracy. Original images of size* 256×256 *pixels was generated with random amplitudes for Zernike modes up to radial order,* $n = 10$*. Each subfigure shows the percentage error in the Zernike mode measurement and the linear regression of all Zernike mode measurements for images resized by* ***(a)*** 1 *i.e. no resizing* ***(b)*** $\frac{1}{2}$ *i.e* 128×128 *pixels* ***(c)*** $\frac{1}{4}$ *i.e* 64×64 *pixels* ***(d)*** $\frac{1}{8}$ *i.e.* 32×32 *pixels*

The accuracy of the Zernike mode amplitude fitting is a limiting factor in two key areas. Firstly, the accuracy of the Zernike mode fitting is one of the limiting factors to acquiring an ideal control matrix and, therefore, the ideal characterisation assay shown in Figure 3.8a. Secondly, the accuracy of the Zernike mode fitting is

one of the limiting factors to acquiring a perfectly flat wavefront through direct wavefront sensing correction.

6.1.2 Sensorless correction accuracy

In order to make sensorless correction accessible to users the entire workflow detailed in Section 3.2.1 is automated. The image quality metric is measured for each image and Python's *scipy*'s *curve_fit* functionality[133] is used to fit a Gaussian function of the form:

$$f(x) = (\Delta - \eta) + \eta e^{-\frac{(x-\mu)^2}{2\sigma^2}}, \tag{6.1}$$

to the data, where Δ is the offset value, η is the normalisation constant, μ is the mean, and σ is the standard deviation. The Zernike mode amplitudes applied and the image quality metric measurements are used as the x and $f(x)$ variables respectively. *scipy*'s *curve_fit* functionality then estimates the values of Δ, η, μ, and σ which give the best fit to the data. An amplitude μ of the current Zernike mode is then applied to obtain the optimum correction for that mode. It is necessary to constrain the values which these parameters can take, otherwise it is possible for the automation to go awry.

Figure 6.3a shows some sample image quality metric values acquired from a correction routine on a *Drosophila* neuro-muscular junction preparation similar to that shown in Section 5.4, acquired on the DeepSIM setup. Here the metric measurements were acquired for oblique astigmatism (Noll index 5) using the Fourier Power metric from Section 3.2.2 and the sampled Zernike mode amplitudes were $[-2, 2]$ radians. If *scipy*'s *curve_fit* functionality is applied with no constraints, the fitting shown in Figure 6.3b is obtained. Clearly, there are two problems with this fit. Firstly, the value of μ is -688 radians. This is a frankly absurdly high aberration, certainly not physically possible for the sample type and depth of imaging in question, and not an aberration amplitude the ALPAO-69 DM on DeepSIM (or any microscopy deformable mirror) is capable of applying. Secondly, the fit has allegedly found a minimum opposed to the desired maximum image quality for this mode.

Imposing the constraint that $\mu \in [z_l, z_u]$ yields Figure 6.3c. Here $z_l = z_{min} - 0.25(z_{max} - z_{min})$ and $z_u = z_{max} + 0.25(z_{max} - z_{min})$ where z_{max} and z_{min} are the maximum and minimum Zernike mode amplitudes applied. The amplitude acquired is of a sensible order of magnitude, 1.85 radians, however the fit still

acquires a minimum. Imposing the constraint that $\eta \in [0, \infty)$ yields Figure 6.3d. These constraints guarantee that the value of μ is both of a sensible order of magnitude and corresponds to a maximum.

It is worth noting that the image quality amplitudes for data points labelled "Measured metric values" in Figure 6.3 were obtained from images acquired with the corresponding Zernike mode amplitudes applied. By contrast, the data points labelled "Zernike amplitude for maximum quality" are obtained from the theoretical image quality metric value according to the obtained fit (i.e. $f(\mu)$) and not from an acquired image. They do not represent the image quality obtained when applying the corresponding Zernike mode amplitude, only the calculated Zernike amplitude for maximum image quality.

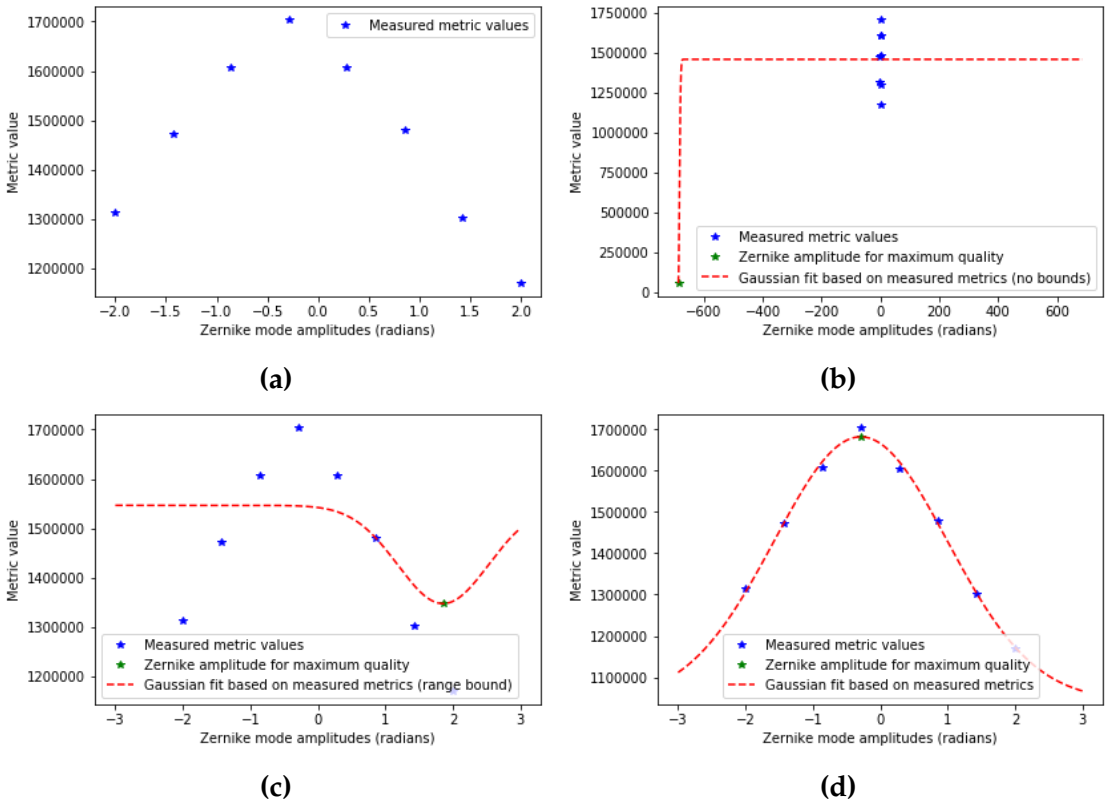


Figure 6.3: *Effect of parameter bounds on sensorless correction fitting accuracy. Metric measurements were acquired for Zernike mode 5 (Noll index) using the Fourier Power metric from Section 3.2.2* ***(a)*** *Measured metric values* ***(b)*** *Gaussian fit with no parameter bounds* ***(c)*** *Gaussian fit with bound on* μ ***(c)*** *Gaussian fit with bound on* μ *and* η

Of course, these constraints do not guarantee a good fit to the data, but they do eliminate some sources of fitting error. If the sample aberration is primarily from one source - i.e. spherical aberration mismatch - then correcting for aberration

modes with smaller amplitudes can prove challenging since the image quality is already heavily degraded. Similarly, if the fit for one mode is poor and leads to an incorrect Zernike mode amplitude being applied, this can bias future image quality measurements and prevent correction of subsequent Zernike modes. The first case explains why the order Zernike modes are corrected in, specified by the user in the interface shown in Figure 3.1d, is important. The second case explains the existence of the "Reset DM" and "Apply last pattern" buttons in Figure 3.1a. "Reset DM" returns all actuators to their default 0 position. "Apply last pattern" applies the last recorded actuator pattern applied to the DM. Actuator patterns applied through "Reset DM" are not recorded. These buttons allow a user to toggle between the calculated sensorless correction pattern and no correction pattern (i.e. all mirror actuators have no voltage applied).

For a sensorless correction routine which has failed due to, for example, an incorrect correction for one mode has caused a run-away degradation of the image quality, this will be visually apparent. Often an incorrect or run-away sensorless routine will result in a decrease in image contrast, overall image intensity, and the loss of fine structures due a decrease in resolving power. For samples with point objects, such as beads or single molecule mRNA, characteristic PSF distortions may be visible. Figure 6.4b shows the results of an unsuccessful sensorless correction routine performed on the Alexa488 channel of bovine pulmonary artery endothelial cells (F36924, Invitrogen), where Alexa488-phalloidin was used to stain F-actin. Figure 6.4b displays poorer contrast, lower intensity, and overall lower resolution compared to Figure 6.4a.

In a successful sensorless correction routine, the improvement in image quality will be visually apparent. Typically, this manifests as increased image contrast, overall image intensity, and additional fine structures becoming observable. Where a structured illumination pattern has been applied during correction, such with IsoSense, the illumination pattern maybe become visible. Figure 6.4d shows the results of a successful sensorless correction routine performed on the Alexa488 channel of a *Drosophila* neuro-muscular junction, prepared as described in Section 5.4.1. Figure 6.4d shows enhanced contrast, higher overall intensity and additional fine structure compared to Figure 6.4c.

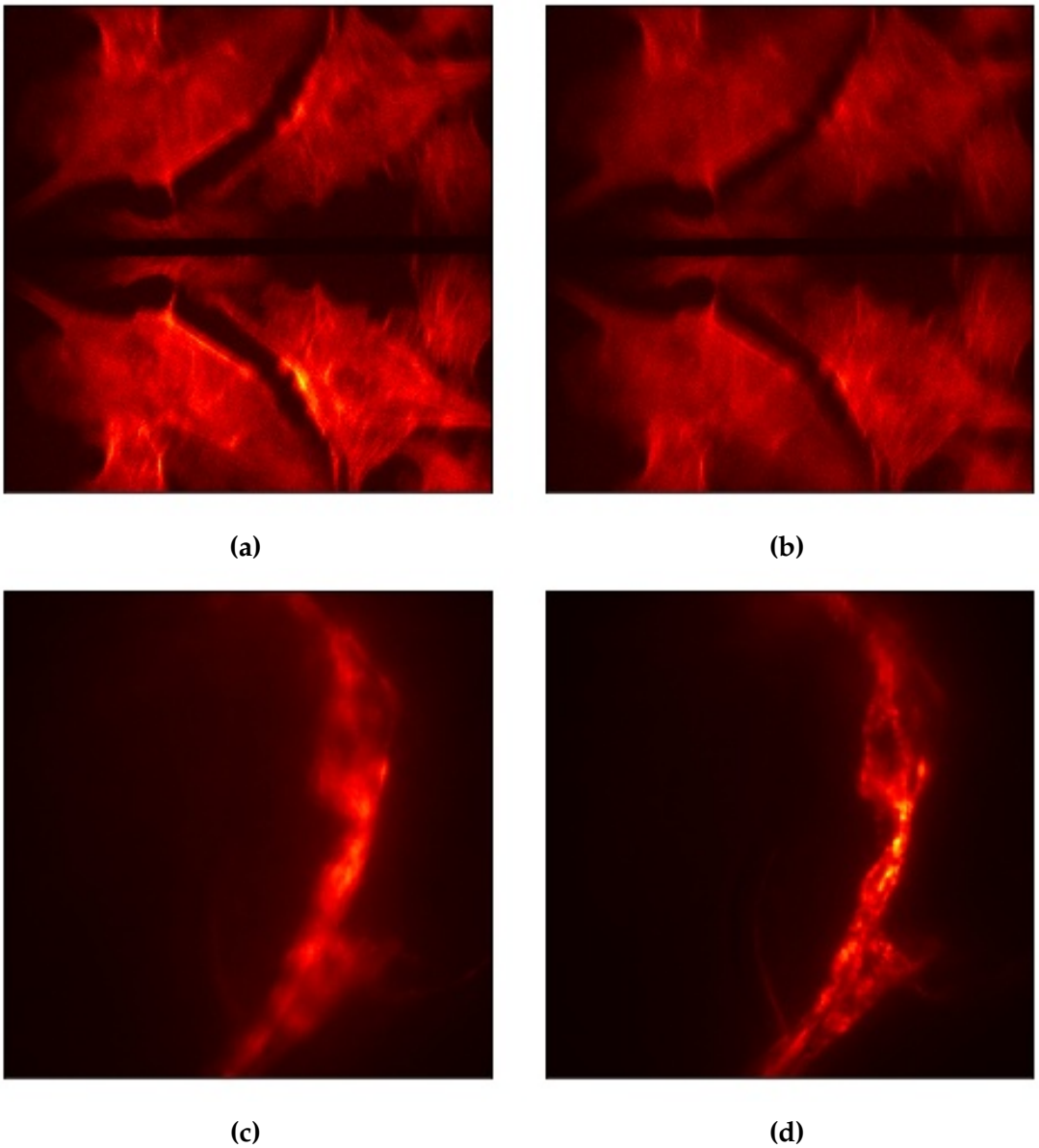


Figure 6.4: *Visual distinction between successful and unsuccessful sensorless correction routines.* ***(a)*** *A bovine pulmonary artery endothelial junction before an unsuccessful sensorless correction routine* ***(b)*** *A bovine pulmonary artery endothelial after an unsuccessful sensorless correction routine.* ***(a)*** *and* ***(b)*** *are displayed on the same colour scale and show the Alexa488 channel staining F-actin.* ***(c)*** *A Drosophila neuro-muscular junction before a successful sensorless correction routine* ***(d)*** *A Drosophila neuro-muscular junction after a successful sensorless correction routine.* ***(c)*** *and* ***(d)*** *are displayed on the same colour scale and show the neuron, visualised with Horseradish Peroxidase (HRP) conjugated to Alexa568 fluorophore.*

Chapter 7

Conclusions

7.1 Summary of Contributions

The primary contributions of this thesis surround enabling the successful deployment of AO in microscopy, culminating in enabling AO in super-resolution systems for improved image quality and imaging depth. As outlined in Figure 1.11 this process consists of four phases:

1. *System Design Phase*: A potential user should consider the needs of their imaging modality, system constraints, desired sample types before deciding on the appropriate AO element to implement.

2. *Installation Phase*: The user installs the chosen AO element into their beam path.

3. *Set-up Phase*: The AO element is calibrated to correct for optical aberrations. This calibration is checked and the system aberrations are corrected.

4. *Sample Correction Phase*: The sample correction routine is designed. This will typically fall into one of two categories: sensorless AO or direct wavefront sensing.

The development of the alignment tool BeamDelta improves the accuracy of the *Installation Phase* by providing an empirical accurate measure of relative alignment between beam paths[103]. It also aids in aberration correction indirectly by minimising the initial optical aberrations present due to alignment errors.

The development of Microscope-AOtools provides a robust, generalised software implementation for the methods required by the *Set-up Phase* and *Sample*

Correction Phase[106]. Microscope-AOtools is designed to be modular and configurable in order to enable it to be used on a range of microscopes with varying adaptive elements, wavefront sensing techniques and sample correction techniques. Microscope-AOtools is integrating into Python-Microscope in order to enable accessibility to microscope users without requiring a complete understanding of all the technical details of the implementation and wide applicability due to the varied hardware support. It is also integrated into Microscope-Cockpit to enable accessibility for biologists.

The primary evidence for the claim that Microscope-AOtools is robust and generalised is its successful deployment on two separate imaging systems, with additional deployments forthcoming. On both the Aurox Clarity and DeepSIM systems, AO correction provided by Microscope-AOtools yielded significant increases in image quality and contrast. On the DeepSIM system, the AO correction was able to enable diffraction-limited imaging of a highly regular fluorescent structure deep in a glass structure with significant spherical aberration. The AO correction also enabled 3D SIM imaging up to 30μm in live biological samples, well beyond the typical 10-20μm imaging depth for SIM[45, 61]. This is particularly notable given the live nature of the samples imaged, since live specimens represent an particularly challenging subset of sample types.

7.2 Future development

Chapter 3 discussed the specific methods implemented in Microscope-AOtools for both AO device set-up and operation. These Set-up and Sample Correction methods rely on suites of techniques, wavefront sensing and image quality metric assessment respectively. These are designed to be easily extensible by users as new techniques are developed. The functions defining the existing wavefront sensing and image quality metric assessment techniques are stored in separate files. A detailed guide of where the appropriate classes and dictionaries are located and how to add new wavefront sensing and image quality metric assessment techniques is included in the *README.md* file for Microscope-AOtools. Briefly, these suites are composed of functions with a defined set of input and output variables. A user creates a new wavefront sensing or image quality metric assessment functions with the input and outputs defined in the *README.md*, adds this function to the correct file and then adds the function option to the correct suite dictionary.

Microscope-AOtools has been designed so a user can take an adaptive element in an arbitrary set-up, calibrate the adaptive element and use it on any sample type in a range of imaging modalities. Since Microscope-AOtools leverages Python-Microscope it already supports a number of adaptive elements, mostly deformable mirrors, which will expand as hardware support in Python-Microscope expands. Adding new devices to Python-Microscope is relatively simple. Refer to Python-Microscope (`https://www.python-microscope.org/`) for more details. Microscope-AOtools only requires that the adaptive element be a Python-Microscope device which has an attribute *n_actuators* which defines the number of variable components of the device.

The process of setting up an adaptive element requires a wavefront sensor to observe the shape of the phase wavefront and calibrate how the variable components of the adaptive element affect this wavefront. By designing the set-up methods in Microscope-AOtools to accept any method from a suite of wavefront sensing techniques, Microscope-AOtools is both generalised and easily extensible. If the desired wavefront sensing technique is not already incorporated then a user only has to add the function necessary to perform the wavefront sensing step rather than to reimplement the set-up methods in their entirety. Swapping between wavefront sensing techniques is not implemented in the Microscope-Cockpit user interface (UI) for AO control since the sensing technique is generally reliant on the physical setup and is unlikely to change between experiments.

Microscope-AOtools is further generalised as it allows for the control matrix to be acquired by some external method and then set in Microscope-AOtools with the *set_controlMatrix* method. This ensures that a user with an existing calibration routine wishing to access the sensorless AO methods in Microscope-AOtools can do so without having to repeat work they have already performed, as was the case in the Aurox Clarity system. It also allows control matrices acquired from routines using different phase acquisition techniques to be compared. Characterisation assays can be acquired for each method's control matrix and the accuracy of the Zernike mode recreation compared.

The generalised nature of Microscope-AOtools continues into the Sample Correction methods. By allowing the user to swap between wavefront sensing techniques, Microscope-AOtools already possesses all the methods necessary for performing sample correction using direct wavefront sensing, provided the wavefront sensing technique is already included in the suite of methods. If the

desired wavefront sensing technique is not currently included, it can easily be implemented and added to the suite of wavefront sensing techniques.

Similarly, Microscope-AOtools utilises a suite of image quality metrics suited to different sample types and imaging modalities for sensorless AO correction. A user can select a pre-existing metric well suited to their application. If no appropriate metric currently exists a new one can easily be implemented and added to the suite of metrics. Since the best image quality metric can vary between samples, this variable is left configurable from the Microscope-Cockpit UI as shown in Figure 3.1b. A user need only add the appropriate label for the newly implemented image quality metric assessment technique to the options present in the Microscope-Cockpit device code and it will be available with the other techniques shown in Figure 3.1b.

Furthermore, Microscope-AOtools allows for Zernike mode amplitudes to be set directly with the *set_phase* method. This means that if a user has an offline analysis technique, such as a machine learning approach, Microscope-AOtools can be used to calibrate the deformable mirror, the calculations of sample induced aberrations are performed offline and then the appropriate correction applied through Microscope-AOtools.

Microscope-AOtools is free and open-source. It is intended to be a resource for the microscopy community at large and it is designed to minimise the time and effort spent replicating work other AO users have already done. As Microscope-AOtools acquires a larger base of users, some adding their own wavefront sensing techniques or image quality metrics to expand the existing suites, future and existing users will have a wider array of usability options, accelerating the adoption of novel techniques by the microscopy community and lowering the barrier to entry to set-up an AO system.

Beyond the open-ended task of expanding the existing suite of phase acquisition techniques and image quality metrics, there are a number of future developments that could be made to Microscope-AOtools. Image quality metrics attempt to assign a numerical value for how 'good' an image is, but what makes a 'good' image varies between imaging modalities, sample type and even users. Most metrics pick some aspect of the image deemed to be significant (e.g. contrast, maximum intensity, spatial frequency information etc) and maximise it. Since Microscope-AOtools has access to multiple image quality metrics, one development would be designing a sensorless AO routine which measures multiple image qualities simultaneously, assigns some weight to each metric measurement and maximises the image quality

based on several criteria. Such combined approaches have already been shown to be successful[154]. There have also been attempts at ranking various image quality metrics for particular microscopy techniques[155]. A combined, weighted image quality analysis is likely to prove a worthwhile addition to the arsenal of sensorless correction methods present in Microscope-AOtools.

Another direction for further development concerns restructuring the sensorless correction workflow. As explained in Section 3.2.1, each Zernike mode is corrected for separately. There is an underlying assumption here that since the Zernike modes themselves are an orthonormal basis set, the effect they have on the image quality must also be orthogonal. However, phenomena such as the focal shift which accompanies spherical aberration would suggest that this is not necessarily the case[156]. It may therefore be possible to obtain the optimum image quality faster and with fewer images utilising the family of solvers used for objective function maximisation, such as the Nelder-Mead method, than the current uni-variant approach[157]. Such an approach has been shown to work in principle on point objects to recover diffraction limited images but has not yet been demonstrated on biological samples[158].

Finally, the integration of adaptive optical elements, primarily deformable mirrors, into Microscope-Cockpit allows for the construction of remote focusing experiments. In remote focusing experiments, the adaptive element is used to shift the focal plane by applying a known amount of optical aberrations to the beam path, instead of manually moving the sample plane. This allows for higher axial scan speeds - since deformable mirrors are, on average, an order of magnitude faster than mechanical stages - and avoids mechanical interference between the objective lens and the sample through dipping media such as water or oil[159, 160] This would require constructing another calibration routine to obtain the maps between physical displacement and defocus aberration applied in order to ensure accurate and reliable remote focusing.

7.3 Final Conclusion

For some time, there has been a call for a robust, generalised implementation for AO. Such an implementation should incorporate all the methods needed to setup and operate an AO element for a range of imaging modalities and sample types. These methods should be exposed to the users in an accessible fashion to allow ease-of-use and require minimal direct user involvement. Microscope-AOtools includes

methods for calibration, direct wavefront and sensorless correction. In particular, it already incorporates several image quality metrics suited to sensorless correction in a number of different imaging modalities. It also includes a characterisation method for assessing the accuracy of the calibration step. It has also been designed in a modular manner allowing for new wavefront sensing techniques and image quality metrics to be added with minimal disruption to the rest of the workflows and, therefore, minimal work duplication. Microscope-AOtools has been integrated into the Microscope-Cockpit user interface in an accessible manner which allows for a user to control key parameters whilst obfuscating much of the technical complexity. It has been shown to be successfully deployed on a number of different systems, with additional deployments forthcoming. It has demonstrably yielded significant improvements in image quality, particularly in challenging samples deep in biological tissue. With time and community support, such an implementation has scope to go beyond its current state of "generalised software implementation" and become a universal software implementation for AO.

7.4 Distribution

Microscope-AOtools is distributed under the GNU General Public License version 3.0 or later. Source releases are available for download from the Python Package Index (`https://pypi.org/project/microscope-aotools/`). Development sources are available from GitHub (`https://github.com/MicronOxford/microscope-aotools`).

Microscope-Cockpit is distributed under the GNU General Public License version 3.0 or later and available from GitHub (`https://github.com/MicronOxford/cockpit`) a more descriptive website and links at `https://micronoxford.com/python-microscope-cockpit`.

Python Microscope is distributed under the GNU General Public License version 3.0 or later. Source releases are available for download from the Python Package Index (`https://pypi.org/project/microscope/`). Development sources are available from GitHub (`https://github.com/python-microscope/microscope`).

Appendix A

Noll indexing and Zernike polynomial expansions

Table A.1 contains the algebraic expansion up to radial order $n = 7$ of the Zernike polynomial sequence expressed in its general form in Equation 1.27. The Zernike polynomials in Table A.1 are presented in ascending Noll index order. The Zernike polynomials are assigned a Noll index, j, first according to their radial order, n, in ascending order. For Zernike polynomials with the same radial order, a Noll index is then assigned according to their absolute azimuthal frequency, $|m|$, in ascending order. Finally, for Zernike polynomials with the same absolute azimuthal frequency, a Noll index is assigned according to the convention that Zernike polynomials with an even Noll index have a $\cos(m\theta)$ term and Zernike polynomials with an odd Noll index have a $\sin(m\theta)$ term[73]. Table A.1 lists for each Zernike polynomial: the Noll index, j; radial order, n; azimuthal frequency, m; algebraic expansion, $\mathcal{Z}_n^m(\rho, \theta)$; and classical aberration name.

Noll index (j)	Radial order (n)	Azimuthal frequency (m)	$\mathcal{Z}_n^m(\rho,\theta)$	Classical aberration name
1	0	0	1	Piston
2	1	$+1$	$2\rho\cos(\theta)$	Tip
3	1	-1	$2\rho\sin(\theta)$	Tilt
4	2	0	$\sqrt{3}\left(2\rho^2-1\right)$	Defocus
5	2	-2	$\sqrt{6}\rho^2\sin(2\theta)$	Oblique Astigmatism
6	2	$+2$	$\sqrt{6}\rho^2\cos(2\theta)$	Vertical Astigmatism
7	3	-1	$\sqrt{8}\left(3\rho^3-2\rho\right)\sin(\theta)$	Vertical Coma
8	3	$+1$	$\sqrt{8}\left(3\rho^3-2\rho\right)\cos(\theta)$	Horizontal Coma
9	3	-3	$\sqrt{8}\rho^3\sin(3\theta)$	Vertical Trefoil
10	3	$+3$	$\sqrt{8}\rho^3\cos(3\theta)$	Oblique Trefoil
11	4	0	$\sqrt{5}\left(6\rho^4-6\rho^2+1\right)$	Primary Spherical
12	4	$+2$	$\sqrt{10}\left(4\rho^4-3\rho^2\right)\cos(2\theta)$	Vertical Secondary Astigmatism
13	4	-2	$\sqrt{10}\left(4\rho^4-3\rho^2\right)\sin(2\theta)$	Oblique Secondary Astigmatism
14	4	$+4$	$\sqrt{10}\rho^4\cos(4\theta)$	Vertical Quadrafoil
15	4	-4	$\sqrt{10}\rho^4\sin(4\theta)$	Oblique Quadrafoil
16	5	$+1$	$\sqrt{12}\left(10\rho^5-12\rho^3+3\rho\right)\cos(\theta)$	Secondary Horizontal Coma
17	5	-1	$\sqrt{12}\left(10\rho^5-12\rho^3+3\rho\right)\sin(\theta)$	Secondary Vertical Coma
18	5	$+3$	$\sqrt{12}\left(5\rho^5-4\rho^3\right)\cos(3\theta)$	-
19	5	-3	$\sqrt{12}\left(5\rho^5-4\rho^3\right)\sin(3\theta)$	-
20	5	$+5$	$\sqrt{12}\rho^5\cos(5\theta)$	Vertical Pentafoil
21	5	-5	$\sqrt{12}\rho^5\sin(5\theta)$	Horizontal Pentafoil
22	6	0	$\sqrt{7}\left(20\rho^6-30\rho^4+12\rho^2-1\right)$	Secondary Spherical
23	6	-2	$\sqrt{14}\left(15\rho^6-20\rho^4+6\rho^2\right)\sin(2\theta)$	-
24	6	$+2$	$\sqrt{14}\left(15\rho^6-20\rho^4+6\rho^2\right)\cos(2\theta)$	-
25	6	-4	$\sqrt{14}\left(6\rho^6-5\rho^4\right)\sin(4\theta)$	-
26	6	$+4$	$\sqrt{14}\left(6\rho^6-5\rho^4\right)\cos(4\theta)$	-
27	6	-6	$\sqrt{14}\rho^6\sin(6\theta)$	-
28	6	$+6$	$\sqrt{14}\rho^6\cos(6\theta)$	-
29	7	-1	$4\left(35\rho^7-60\rho^5+30\rho^3-4\rho\right)\sin(\theta)$	-
30	7	$+1$	$4\left(35\rho^7-60\rho^5+30\rho^3-4\rho\right)\cos(\theta)$	-
31	7	-3	$4\left(2\rho^7-30\rho^5+10\rho^3\right)\sin(3\theta)$	-
32	7	$+3$	$4\left(2\rho^7-30\rho^5+10\rho^3\right)\cos(3\theta)$	-
33	7	-5	$4\left(7\rho^7-6\rho^5\right)\sin(5\theta)$	-
34	7	$+5$	$4\left(7\rho^7-6\rho^5\right)\cos(5\theta)$	-
35	7	-7	$4\rho^7\sin(7\theta)$	-
36	7	$+7$	$4\rho^7\cos(7\theta)$	-

Table A.1: *Algebraic expansion of the Zernike polynomial sequence*

Appendix B

Point object seperation figure generation

Figures 1.3 and 1.8 were generated using the code presented in Sections B.1 and B.2 respectively. The majority of imported packages are freely available through PyPI. czernike is part of the enzpy Python package. The fourier package is used to generate aberrated PSFs using regular Fourier optics[161] and real-valued Zernike coefficients in the pupil only. It was developed and provided by Dr Jacopo Antonello.

B.1 Ideal point object seperation

```
#!/usr/bin/env python3
# -*- coding: utf-8 -*-

import sys  # noqa
import numpy as np  # noqa
import matplotlib.pyplot as plt  # noqa

from h5py import File

from czernike import RZern  # noqa
from fourier import Fraunhofer  # noqa

plt.close('all')

Np = 256
wavelength = 561.0e-9
NA = 1.1
n1 = 1.51
```

```
d = 1.22*wavelength/(2*NA)
pixel_size = d/32
crit_fracs = [0.5,1.0,1.22,1.5,2.0]
n_alpha = 8  # maximum radial order of Zernike polynomials

v = np.linspace(-((pixel_size*(Np/2))/d)*np.pi,
((pixel_size*(Np/2))/d)*np.pi, Np)

# load an object
#with File('./obj.h5', 'r') as f:
#    obj = f['obj'][()]
it = 0

for crit_frac in crit_fracs:

        point_obj_1 = np.zeros((Np,Np))
        point_obj_1[Np//2, Np//2] = 1

        point_obj_2 = np.zeros((Np,Np))
        point_obj_2[Np//2, Np//2 +
                int((crit_frac*wavelength)/(2*NA*pixel_size))] = 1

        obj = np.zeros((Np,Np))
        obj[Np//2, Np//2] = 1
        obj[Np//2, Np//2 +
                int((crit_frac*wavelength)/(2*NA*pixel_size))] = 1

        # object to make PSFs using Fourier optics
        fh = Fraunhofer(wavelength=wavelength, NA=NA, N=Np,
                pixel_size=pixel_size, n_alpha=n_alpha)

        # random aberration
        alpha = fh.make_random_aberration(rms=1)

        # uncomment for fixed aberration
        alpha *= 0
        noll = 1
        alpha[noll - 1] = 0

        psf = fh.psf(alpha)
        mtf = fh.mtf(psf)

        point_obj_1_img = fh.incoherent(point_obj_1, psf)
        point_obj_1_img_norm =
                point_obj_1_img/np.max(point_obj_1_img)
```

```
        point_obj_2_img = fh.incoherent(point_obj_2, psf)
        point_obj_2_img_norm =
                point_obj_2_img/np.max(point_obj_2_img)

        img = fh.incoherent(obj, psf)
        img_norm = img/np.max(img)

        display_min = np.min(img_norm)
        display_max = np.max(img_norm)

        plt.figure(it*2,figsize=(10,3.85))
        nn = 1
        mm = 2

        plt.subplot(nn, mm, 1)
        plt.plot(v, point_obj_1_img_norm[Np//2,:], 'r--')
        plt.plot(v, point_obj_2_img_norm[Np//2,:], 'b--')
        plt.plot(v, (point_obj_1_img_norm+
                point_obj_2_img_norm)[Np//2,:], 'g')
        plt.ylabel("Normalised intensity")
        plt.xlabel("Normalised lateral coordinate")
        #plt.title("Object separation %.3f\u03C0" %crit_frac)
        #plt.tight_layout()

        plt.subplot(nn, mm, 2)
        plt.imshow(img)
        plt.tick_params(axis='both', which='both',
                bottom=False, top=False, labelbottom=False,
                right=False, left=False, labelleft=False)

        plt.tight_layout()
        plt.savefig("Airy_ring_2_object_seperation_%s_%s"
                %(str(crit_frac)[0],str(crit_frac)[2:]),
                bbox_inches='tight')

        it += 1

plt.show()
```

B.2 Aberrated point object seperation

```
#!/usr/bin/env python3
# -*- coding: utf-8 -*-
```

```
import sys  # noqa
import numpy as np  # noqa
import matplotlib.pyplot as plt  # noqa

from h5py import File

from czernike import RZern  # noqa
from fourier import Fraunhofer  # noqa

plt.close('all')

Np = 256
wavelength = 561.0e-9
NA = 1.1
n1 = 1.51
d = 1.22*wavelength/(2*NA)
pixel_size = d/32
crit_frac = 1.22
n_alpha = 8  # maximum radial order of Zernike polynomials

v = np.linspace(-3*np.pi, 3*np.pi, Np)

# load an object
#with File('./obj.h5', 'r') as f:
#    obj = f['obj'][()]

point_obj_1 = np.zeros((Np,Np))
point_obj_1[Np//2, Np//2] = 1

point_obj_2 = np.zeros((Np,Np))
point_obj_2[Np//2, Np//2 +
        int((crit_frac*wavelength)/(2*NA*pixel_size))] = 1

obj = np.zeros((Np,Np))
obj[Np//2, Np//2] = 1
obj[Np//2, Np//2 +
        int((crit_frac*wavelength)/(2*NA*pixel_size))] = 1

# object to make PSFs using Fourier optics
fh = Fraunhofer(
wavelength=wavelength, NA=NA, N=Np, pixel_size=pixel_size,
n_alpha=n_alpha)

# random aberration
```

```
alpha = fh.make_random_aberration(rms=1)

# uncomment for fixed aberration
alpha *= 0
noll = 1
alpha[noll - 1] = 0

psf = fh.psf(alpha)
mtf = fh.mtf(psf)

point_obj_1_img = fh.incoherent(point_obj_1, psf)
point_obj_1_img_norm = point_obj_1_img/np.max(point_obj_1_img)

point_obj_2_img = fh.incoherent(point_obj_2, psf)
point_obj_2_img_norm = point_obj_2_img/np.max(point_obj_2_img)

img = fh.incoherent(obj, psf)
img_norm = img/np.max(img)

display_min = np.min(img_norm)
display_max = np.max(img_norm)

# random aberration
alpha_ab = fh.make_random_aberration(rms=1)

it = 0
for noll in range(1,12):
#for noll in range(1):

        # uncomment for fixed aberration
        alpha_ab *= 0
        alpha_ab[noll - 1] = 1

        psf_ab = fh.psf(alpha_ab)
        mtf_ab = fh.mtf(psf_ab)

        point_obj_1_img_ab = fh.incoherent(point_obj_1, psf_ab)
        point_obj_1_img_norm_ab =
                point_obj_1_img_ab/np.max(point_obj_1_img)

        point_obj_2_img_ab = fh.incoherent(point_obj_2, psf_ab)
        point_obj_2_img_norm_ab =
                point_obj_2_img_ab/np.max(point_obj_2_img)

        img_ab = fh.incoherent(obj, psf_ab)
```

```
img_norm_ab = img_ab/np.max(img)

plt.figure(it*2)
nn = 2
mm = 2

plt.subplot(nn, mm, 1)
plt.plot(v, point_obj_1_img_norm_ab[Np//2,:])
plt.ylabel("Normalised intensity")
plt.xlabel("Normalised lateral coordinate")

plt.subplot(nn, mm, 2)
plt.imshow(point_obj_1_img_norm_ab, vmin=display_min,
        vmax=display_max)
plt.tick_params(axis='both', which='both', bottom=False,
        top=False, labelbottom=False, right=False,
        left=False, labelleft=False)
plt.title('PSF')

plt.subplot(nn, mm, 3)
plt.plot(v, point_obj_1_img_norm_ab[Np//2,:], 'r--')
plt.plot(v, point_obj_2_img_norm_ab[Np//2,:], 'b--')
plt.plot(v,
        (point_obj_1_img_norm_ab+point_obj_2_img_norm_ab)
        [Np//2,:], 'g')
plt.ylabel("Normalised intensity")
plt.xlabel("Normalised lateral coordinate")
#plt.title("Object separation %.3f\u03C0" %crit_frac)

plt.subplot(nn, mm, 4)
plt.imshow(img_norm_ab, vmin=display_min,
vmax=display_max)
plt.tick_params(axis='both', which='both', bottom=False,
        top=False, labelbottom=False, right=False,
        left=False, labelleft=False)
plt.title('Image')

plt.tight_layout()
plt.savefig("Airy_ring_2D_2_object_seperation_%s_%s_Noll_%i"
%(str(crit_frac)[0],str(crit_frac)[2:],noll),
bbox_inches='tight')

plt.figure((it*2)+1)
nn = 2
mm = 2
```

```
        plt.subplot(nn, mm, 1)
        plt.plot(v, point_obj_1_img_norm[Np//2,:], 'r--')
        plt.plot(v, point_obj_2_img_norm[Np//2,:], 'b--')
        plt.plot(v,
                (point_obj_1_img_norm+point_obj_2_img_norm)[Np//2,:]
                ,'g')
        plt.ylabel("Normalised intensity")
        plt.xlabel("Normalised lateral coordinate")
        #plt.title("Object separation %.3f\u03C0" %crit_frac)

        plt.subplot(nn, mm, 2)
        plt.imshow(img_norm, vmin=display_min, vmax=display_max)
        plt.tick_params(axis='both', which='both', bottom=False,
                top=False, labelbottom=False, right=False,
                left=False, labelleft=False)
        plt.title('Unaberrated image')

        plt.subplot(nn, mm, 3)
        plt.plot(v, point_obj_1_img_norm_ab[Np//2,:], 'r--')
        plt.plot(v, point_obj_2_img_norm_ab[Np//2,:], 'b--')
        plt.plot(v,
                (point_obj_1_img_norm_ab+point_obj_2_img_norm_ab)
                [Np//2,:], 'g')
        plt.ylabel("Normalised intensity")
        plt.xlabel("Normalised lateral coordinate")
        #plt.title("Object separation %.3f\u03C0" %crit_frac)

        plt.subplot(nn, mm, 4)
        plt.imshow(img_norm_ab, vmin=display_min,
                vmax=display_max)
        plt.tick_params(axis='both', which='both', bottom=False,
                top=False, labelbottom=False, right=False,
                left=False, labelleft=False)
        plt.title('Aberrated image')

        plt.tight_layout()
        plt.savefig("Airy_ring_2D_2_object_seperation_aberration_c
        omparison_Noll_%i" %noll, bbox_inches='tight')

        it += 1

plt.show()
```

Bibliography

[1] Lucius Annaeus Seneca. *Naturales quaestiones: Book I-III*. 450. Harvard University Press, 1971.

[2] Seyyed Hossein Nasr and Giorgio De Santillana. *Science and civilization in Islam*. Vol. 16. Harvard University Press Cambridge, MA, 1968.

[3] David Bardell. "The invention of the microscope". In: *Bios* 75.2 (2004), pp. 78–84.

[4] Robert Hooke. *Micrographia, or, Some physiological descriptions of minute bodies made by magnifying glasses: With observations and inquiries thereupon.* London: Printed by J. Martyn and J. Allestry, 1665.

[5] King-Thom Chung and Jong-Kang Liu. *Pioneers in Microbiology: The Human Side of Science*. World Scientific, 2017.

[6] CR Burch and JPP Stock. "Phase-contrast microscopy". In: *Journal of Scientific Instruments* 19.5 (1942), p. 71.

[7] Hani A Alturkistani, Faris M Tashkandi, and Zuhair M Mohammedsaleh. "Histological stains: a literature review and case study". In: *Global journal of health science* 8.3 (2016), p. 72.

[8] Rafael Yuste. "Fluorescence microscopy today". In: *Nature methods* 2.12 (2005), pp. 902–904.

[9] Ionita C Ghiran. "Introduction to fluorescence microscopy". In: *Light microscopy*. Springer, 2011, pp. 93–136.

[10] Mick A Phillips, David M Susano Pinto, and Ian M Dobbie. "SPEKcheck-fluorescence microscopy spectral visualisation and optimisation: a web application, javascript library, and data resource". In: *Wellcome open research* 3 (2018).

[11] Malte Renz. "Fluorescence microscopyâĂŤA historical and technical perspective". In: *Cytometry Part A* 83.9 (2013), pp. 767–779.

[12] Albert H Coons et al. "The demonstration of pneumococcal antigen in tissues by the use of fluorescent antibody". In: *The Journal of Immunology* 45.3 (1942), pp. 159–170.

[13] AH Coons. "Fluorescent antibodies as histochemical tools." In: *Federation proceedings*. Vol. 10. 2. 1951, p. 558.

[14] Thomas H Weller and Albert H Coons. "Fluorescent antibody studies with agents of varicella and herpes zoster propagated in vitro." In: *Proceedings of the Society for Experimental Biology and Medicine* 86.4 (1954), pp. 789–794.

[15] Douglas C Prasher et al. "Primary structure of the Aequorea victoria green-fluorescent protein". In: *Gene* 111.2 (1992), pp. 229–233.

[16] Roger Heim and Roger Y Tsien. "Engineering green fluorescent protein for improved brightness, longer wavelengths and fluorescence resonance energy transfer". In: *Current biology* 6.2 (1996), pp. 178–182.

[17] Harekrushna Sahoo. "Fluorescent labeling techniques in biomolecules: a flashback". In: *RSC advances* 2.18 (2012), pp. 7017–7029.

[18] Martin Chalfie et al. "Green fluorescent protein as a marker for gene expression". In: *Science* 263.5148 (1994), pp. 802–805.

[19] Christopher P Toseland. "Fluorescent labeling and modification of proteins". In: *Journal of chemical biology* 6.3 (2013), pp. 85–95.

[20] Michael W Davidson and Mortimer Abramowitz. "Optical microscopy". In: *Encyclopedia of imaging science and technology* (2002).

[21] Joseph W Goodman. *Introduction to Fourier optics*. Roberts and Company Publishers, 2005.

[22] Max Born and Emil Wolf. *Principles of optics: electromagnetic theory of propagation, interference and diffraction of light*. Elsevier, 2013.

[23] George Neville Watson. *A treatise on the theory of Bessel functions*. Cambridge university press, 1995.

[24] Tony Wilson and Colin Sheppard. *Theory and practice of scanning optical microscopy*. Vol. 180. Academic Press London, 1984.

[25] Lord Rayleigh. "XII. On the manufacture and theory of diffraction-gratings". In: *The London, Edinburgh, and Dublin Philosophical Magazine and Journal of Science* 47.310 (1874), pp. 81–93.

[26] Lord Rayleigh. "Investigations in optics, with special reference to the spectroscope". In: *Monthly Notices of the Royal Astronomical Society* 40 (1880), p. 254.

[27] James Pawley. *Handbook of biological confocal microscopy*. Vol. 236. Springer Science & Business Media, 2006.

[28] Robert L Lucke. "Rayleigh-Sommerfeld Fraunhofer diffraction". In: *arXiv preprint physics/0604229* (2006).

[29] John E Greivenkamp. *Field guide to geometrical optics*. Vol. 1, pp. 19–20.

[30] Peter Török and Fu-Jen Kao. *Optical imaging and microscopy: techniques and advanced systems*. Vol. 87. Springer, 2007.

[31] Matthew R Foreman and Peter Török. "Computational methods in vectorial imaging". In: *Journal of Modern Optics* 58.5-6 (2011), pp. 339–364.

[32] Arnold Jan Den Dekker and A Van den Bos. "Resolution: a survey". In: *JOSA A* 14.3 (1997), pp. 547–557.

[33] Ernst Abbe. "Beiträge zur Theorie des Mikroskops und der mikroskopischen Wahrnehmung". In: *Archiv für mikroskopische Anatomie* 9.1 (1873), pp. 413–418.

[34] Siegfried Weisenburger and Vahid Sandoghdar. "Light microscopy: an ongoing contemporary revolution". In: *Contemporary Physics* 56.2 (2015), pp. 123–143.

[35] Sripad Ram, E. Sally Ward, and Raimund J. Ober. "Beyond Rayleigh's criterion: A resolution measure with application to single-molecule microscopy". In: *Proceedings of the National Academy of Sciences* 103.12 (2006), pp. 4457–4462. ISSN: 0027-8424. DOI: 10.1073/pnas.0508047103. eprint: https://www.pnas.org/content/103/12/4457.full.pdf. URL: https://www.pnas.org/content/103/12/4457.

[36] Siân Culley et al. "NanoJ-SQUIRREL: quantitative mapping and minimisation of super-resolution optical imaging artefacts". In: *BioRxiv* (2017), p. 158279.

[37] B Roy Frieden. "Optical transfer of the three-dimensional object". In: *JOSA* 57.1 (1967), pp. 56–66.

[38] G Behan et al. "Three-dimensional imaging by optical sectioning in the aberration-corrected scanning transmission electron microscope". In: *Philosophical Transactions of the Royal Society A: Mathematical, Physical and Engineering Sciences* 367.1903 (2009), pp. 3825–3844.

[39] Matthew R Arnison and Colin JR Sheppard. "A 3D vectorial optical transfer function suitable for arbitrary pupil functions". In: *Optics communications* 211.1-6 (2002), pp. 53–63.

[40] David A Agard and John W Sedat. "Three-dimensional architecture of a polytene nucleus". In: *Nature* 302.5910 (1983), pp. 676–681.

[41] Wes Wallace, Lutz H Schaefer, and Jason R Swedlow. "A workingperson's guide to deconvolution in light microscopy". In: *Biotechniques* 31.5 (2001), pp. 1076–1097.

[42] CJR Sheppard and T Wilson. "The theory of the direct-view confocal microscope". In: *Journal of microscopy* 124.2 (1981), pp. 107–117.

[43] Marvin Minsky. "Memoir on inventing the confocal scanning microscope". In: *Scanning* 10.4 (1988), pp. 128–138.

[44] Lothar Schermelleh, Rainer Heintzmann, and Heinrich Leonhardt. "A guide to super-resolution fluorescence microscopy". In: *The Journal of cell biology* 190.2 (2010), pp. 165–175.

[45] Lothar Schermelleh et al. "Super-resolution microscopy demystified". In: *Nature cell biology* 21.1 (2019), p. 72.

[46] Alex von Diezmann, Yoav Shechtman, and WE Moerner. "Three-dimensional localization of single molecules for super-resolution imaging and single-particle tracking". In: *Chemical reviews* 117.11 (2017), pp. 7244–7275.

[47] Hans Blom and Hjalmar Brismar. "STED microscopy: increased resolution for medical research?" In: *Journal of internal medicine* 276.6 (2014), pp. 560–578.

[48] Giuseppe Vicidomini, Paolo Bianchini, and Alberto Diaspro. "STED super-resolved microscopy". In: *Nature methods* 15.3 (2018), p. 173.

[49] Mats GL Gustafsson. "Surpassing the lateral resolution limit by a factor of two using structured illumination microscopy". In: *Journal of microscopy* 198.2 (2000), pp. 82–87.

[50] Stefan W Hell et al. "The 2015 super-resolution microscopy roadmap". In: *Journal of Physics D: Applied Physics* 48.44 (2015), p. 443001.

[51] Bonnie O Leung and Keng C Chou. "Review of super-resolution fluorescence microscopy for biology". In: *Applied spectroscopy* 65.9 (2011), pp. 967–980.

[52] Giulia MR De Luca et al. "Re-scan confocal microscopy: scanning twice for better resolution". In: *Biomedical optics express* 4.11 (2013), pp. 2644–2656.

[53] Joseph Huff. "The Airyscan detector from ZEISS: confocal imaging with improved signal-to-noise ratio and super-resolution". In: *Nature methods* 12.12 (2015), pp. i–ii.

[54] Andrew G York et al. "Instant super-resolution imaging in live cells and embryos via analog image processing". In: *Nature methods* 10.11 (2013), pp. 1122–1126.

[55] Alistair Curd et al. "Construction of an instant structured illumination microscope". In: *Methods* 88 (2015), pp. 37–47.

[56] Jelmer Cnossen et al. "Localization microscopy at doubled precision with patterned illumination". In: *Nature methods* 17.1 (2020), pp. 59–63.

[57] Rainer Heintzmann and Christoph G Cremer. "Laterally modulated excitation microscopy: improvement of resolution by using a diffraction grating". In: *Optical Biopsies and Microscopic Techniques III*. Vol. 3568. International Society for Optics and Photonics. 1999, pp. 185–196.

[58] Mats GL Gustafsson. "Extended resolution fluorescence microscopy". In: *Current opinion in structural biology* 9.5 (1999), pp. 627–628.

[59] Mats GL Gustafsson et al. "Three-dimensional resolution doubling in wide-field fluorescence microscopy by structured illumination". In: *Biophysical journal* 94.12 (2008), pp. 4957–4970.

[60] Clare D McGillem and George R Cooper. *Continuous and discrete signal and system analysis*. Oxford University Press, USA, 1991.

[61] Yicong Wu and Hari Shroff. "Faster, sharper, and deeper: structured illumination microscopy for biological imaging". In: *Nature methods* 15.12 (2018), pp. 1011–1019.

[62] John R Allen, Stephen T Ross, and Michael W Davidson. "Structured illumination microscopy for superresolution". In: *Chemphyschem* 15.4 (2014), pp. 566–576.

[63] James C Wyant and Katherine Creath. "Basic wavefront aberration theory for optical metrology". In: *Applied optics and optical engineering* 11.part 2 (1992), pp. 28–39.

[64] Emil Wolf. "The diffraction theory of aberrations". In: *Reports on progress in physics* 14.1 (1951), p. 95.

[65] Joel A Kubby. *Adaptive Optics for Biological Imaging*. CRC press, 2013.

[66] Martin J Booth. "Adaptive optics in microscopy". In: *Philosophical Transactions of the Royal Society of London A: Mathematical, Physical and Engineering Sciences* 365.1861 (2007), pp. 2829–2843.

[67] Alexey N Bashkatov, Elina A Genina, and Valery V Tuchin. "Optical properties of skin, subcutaneous, and muscle tissues: a review". In: *Journal of Innovative Optical Health Sciences* 4.01 (2011), pp. 9–38.

[68] Steven L Jacques. "Optical properties of biological tissues: a review". In: *Physics in Medicine & Biology* 58.11 (2013), R37.

[69] Anthony Kim and Brian C Wilson. "Measurement of ex vivo and in vivo tissue optical properties: methods and theories". In: *Optical-Thermal Response of Laser-Irradiated Tissue*. Springer, 2010, pp. 267–319.

[70] Julia L Sandell and Timothy C Zhu. "A review of in-vivo optical properties of human tissues and its impact on PDT". In: *Journal of biophotonics* 4.11-12 (2011), pp. 773–787.

[71] J Antonello. "Optimisation-based wavefront sensorless adaptive optics for microscopy". PhD thesis. TU Delft, Delft University of Technology, 2014.

[72] Frits Zernike. "Diffraction theory of the knife-edge test and its improved form, the phase-contrast method". In: *Monthly Notices of the Royal Astronomical Society* 94 (1934), pp. 377–384.

[73] Robert J Noll. "Zernike polynomials and atmospheric turbulence". In: *JOsA* 66.3 (1976), pp. 207–211.

[74] Virendra N Mahajan. "Zernike circle polynomials and optical aberrations of systems with circular pupils". In: *Applied optics* 33.34 (1994), pp. 8121–8124.

[75] Xiang Hao et al. "Aberrations in 4Pi microscopy". In: *Optics express* 25.13 (2017), pp. 14049–14058.

[76] Michael Schwertner, Martin J Booth, and Tony Wilson. "Characterizing specimen induced aberrations for high NA adaptive optical microscopy". In: *Optics express* 12.26 (2004), pp. 6540–6552.

[77] Christopher J Progler and Alfred KK Wong. "Zernike coefficients: are they really enough?" In: *Optical Microlithography XIII*. Vol. 4000. International Society for Optics and Photonics. 2000, pp. 40–52.

[78] Vasudevan Lakshminarayanan and Andre Fleck. "Zernike polynomials: a guide". In: *Journal of Modern Optics* 58.7 (2011), pp. 545–561.

[79] Larry N Thibos et al. "Standards for reporting the optical aberrations of eyes". In: *Journal of refractive surgery* 18.5 (2002), S652–S660.

[80] John Loomis. "A computer program for analysis of interferometric data". In: *Optical InterferogramsâĂŤReduction and Interpretation*. ASTM International, 1978.

[81] Oleg Soloviev. "Optimal basis for modal sensorless adaptive optics". In: *arXiv preprint arXiv:1707.08489* (2017).

[82] GJ Burton and ND Haig. "Effects of the Seidel aberrations on visual target discrimination". In: *JOSA A* 1.4 (1984), pp. 373–385.

[83] Martin J Booth. "Adaptive optical microscopy: the ongoing quest for a perfect image". In: *Light: Science & Applications* 3.4 (2014), e165.

[84] Chen Wang et al. "Multiplexed aberration measurement for deep tissue imaging in vivo". In: *Nature methods* 11.10 (2014), p. 1037.

[85] John M Girkin, Simon Poland, and Amanda J Wright. "Adaptive optics for deeper imaging of biological samples". In: *Current opinion in biotechnology* 20.1 (2009), pp. 106–110.

[86] Horace W Babcock. "Adaptive optics revisited". In: *Science* 249.4966 (1990), pp. 253–257.

[87] V Fraisier et al. "Adaptive optics in spinning disk microscopy: improved contrast and brightness by a simple and fast method". In: *Journal of microscopy* 259.3 (2015), pp. 219–227.

[88] Alexander Jesacher and Martin J Booth. "Sensorless adaptive optics for microscopy". In: *MEMS Adaptive Optics V*. Vol. 7931. International Society for Optics and Photonics. 2011, 79310G.

[89] Yifan Jian et al. "Wavefront sensorless adaptive optics optical coherence tomography for in vivo retinal imaging in mice". In: *Biomedical optics express* 5.2 (2014), pp. 547–559.

[90] Scot S Olivier. "Advanced adaptive optics technology development". In: *Adaptive Optics Systems and Technology II*. Vol. 4494. International Society for Optics and Photonics. 2002, pp. 1–10.

[91] Isaac Trumper, Heejoo Choi, and Dae Wook Kim. "Instantaneous phase shifting deflectometry". In: *Optics Express* 24.24 (2016), pp. 27993–28007.

[92] Michael Schwertner et al. "Measurement of specimen-induced aberrations of biological samples using phase stepping interferometry". In: *Journal of microscopy* 213.1 (2004), pp. 11–19.

[93] Daniel Burke et al. "Adaptive optics correction of specimen-induced aberrations in single-molecule switching microscopy". In: *Optica* 2.2 (2015), pp. 177–185.

[94] Martin J Booth et al. "Adaptive aberration correction in a confocal microscope". In: *Proceedings of the National Academy of Sciences* 99.9 (2002), pp. 5788–5792.

[95] JR Fienup and JJ Miller. "Aberration correction by maximizing generalized sharpness metrics". In: *JOSA A* 20.4 (2003), pp. 609–620.

[96] Jacopo Antonello et al. "Multi-scale sensorless adaptive optics: application to stimulated emission depletion microscopy". In: *Optics Express* 28.11 (2020), pp. 16749–16763.

[97] Delphine Débarre, Martin J Booth, and Tony Wilson. "Image based adaptive optics through optimisation of low spatial frequencies". In: *Optics Express* 15.13 (2007), pp. 8176–8190.

[98] Delphine Débarre et al. "Adaptive optics for structured illumination microscopy". In: *Optics express* 16.13 (2008), pp. 9290–9305.

[99] Martin Booth et al. "Aberrations and adaptive optics in super-resolution microscopy". In: *Microscopy* 64.4 (2015), pp. 251–261.

[100] Benjamin Thomas et al. "Enhanced resolution through thick tissue with structured illumination and adaptive optics". In: *Journal of biomedical optics* 20.2 (2015), p. 026006.

[101] Na Ji. "Adaptive optical fluorescence microscopy". In: *Nature methods* 14.4 (2017), p. 374.

[102] Cristina Rodríguez and Na Ji. "Adaptive optical microscopy for neurobiology". In: *Current opinion in neurobiology* 50 (2018), pp. 83–91.

[103] Nicholas Hall, David M S Pinto, and Ian M Dobbie. "BeamDelta: simple alignment tool for optical systems". In: *Wellcome Open Research* 4 (2019).

[104] David Miguel Miguel Susano Susano Pinto et al. "Python-Microscope: high performance control of arbitrarily complex and scalable bespoke microscopes". In: *bioRxiv* (2021).

[105] Mick A Phillips et al. "Microscope-Cockpit: Python-based bespoke microscopy for bio-medical science". In: *bioRxiv* (2021).

[106] Nicholas Hall et al. "Microscope-AOtools: A generalised adaptive optics implementation". In: *Optics Express* 28.20 (2020), pp. 28987–29003.

[107] Syed Asad Hussain et al. "Wavefront-sensorless adaptive optics with a laser-free spinning disk confocal microscope". In: *Journal of Microscopy* (2020).

[108] Adaobi Nwaneshiudu et al. "Introduction to confocal microscopy". In: *Journal of Investigative Dermatology* 132.12 (2012), pp. 1–5.

[109] GQ Xiao, To R Corle, and GS Kino. "Real-time confocal scanning optical microscope". In: *Applied physics letters* 53.8 (1988), pp. 716–718.

[110] M David Egger and Mojmir Petran. "New reflected-light microscope for viewing unstained brain and ganglion cells". In: *Science* 157.3786 (1967), pp. 305–307.

[111] John Fuseler, W Gray Jay Jerome, and Robert L Price. "Types of confocal instruments: Basic principles and advantages and disadvantages". In: *Basic confocal microscopy*. Springer, 2018, pp. 187–213.

[112] Roger Y Tsien and Brian J Bacskai. "Video-rate confocal microscopy". In: *Handbook of biological confocal microscopy*. Springer, 1995, pp. 459–478.

[113] GS Kino. "Intermediate optics in Nipkow disk microscopes". In: *Handbook of Biological Confocal Microscopy*. Springer, 1995, pp. 155–165.

[114] Denis Semwogerere and Eric R Weeks. "Confocal microscopy". In: *Encyclopedia of biomaterials and biomedical engineering* 23 (2005), pp. 1–10.

[115] E Wang, CM Babbey, and Kenneth W Dunn. "Performance comparison between the high-speed Yokogawa spinning disc confocal system and single-point scanning confocal systems". In: *Journal of microscopy* 218.2 (2005), pp. 148–159.

[116] R Juskaitis et al. "Efficient real-time confocal microscopy with white light sources". In: *Nature* 383.6603 (1996), pp. 804–806.

[117] Tony Wilson et al. "Confocal microscopy by aperture correlation". In: *Optics letters* 21.23 (1996), pp. 1879–1881.

[118] Mark AA Neil, Rimas Juškaitis, and Tony Wilson. "Method of obtaining optical sectioning by using structured light in a conventional microscope". In: *Optics letters* 22.24 (1997), pp. 1905–1907.

[119] Lei Huang et al. "Close-loop performance of a high precision deflectometry controlled deformable mirror (DCDM) unit for wavefront correction in adaptive optics system". In: *Optics Communications* 393 (2017), pp. 83–88.

[120] Tony Wilson. *Confocal microscopy*. Academic press, 1990.

[121] Marcel JE Golay. "Multi-slit spectrometry". In: *JOSA* 39.6 (1949), pp. 437–444.

[122] Lothar Schermelleh et al. "Subdiffraction multicolor imaging of the nuclear periphery with 3D structured illumination microscopy". In: *Science* 320.5881 (2008), pp. 1332–1336.

[123] Timothy T Weil et al. "Distinguishing direct from indirect roles for bicoid mRNA localization factors". In: *Development* 137.1 (2010), pp. 169–176.

[124] Sebastian Haase. "OMX-a novel high speed and high resolution microscope and its application to nuclear and chromosomal structure analysis". In: (2008).

[125] Ian Dobbie et al. “OMX: A new platform for multi-modal, multi-channel widefield imaging”. In: *Cold Spring Harbor protocols* 2011.8 (2011), p. 899.

[126] Michael A Phillips et al. “CryoSIM: super-resolution 3D structured illumination cryogenic fluorescence microscopy for correlated ultrastructural imaging”. In: *Optica* 7.7 (2020), pp. 802–812.

[127] Kenneth N Ogle. “On the resolving power of the human eye”. In: *JOSA* 41.8 (1951), pp. 517–520. DOI: 10.1364/JOSA.41.000517.

[128] Diako Mardanbegi and Dan Witzner Hansen. “Parallax error in the monocular head-mounted eye trackers”. In: *Proceedings of the 2012 ACM conference on ubiquitous computing*. ACM. 2012, pp. 689–694. DOI: 10.1145/2370216.2370366.

[129] David H Sliney. “Laser safety”. In: *Lasers in surgery and medicine* 16.3 (1995), pp. 215–225. DOI: 10.1002/lsm.1900160303.

[130] Kai Wang et al. “Rapid adaptive optical recovery of optimal resolution over large volumes”. In: *nature methods* 11.6 (2014), pp. 625–628.

[131] Kai Wang et al. “Direct wavefront sensing for high-resolution in vivo imaging in scattering tissue”. In: *Nature communications* 6.1 (2015), pp. 1–6.

[132] Stéfan van der Walt, S Chris Colbert, and Gael Varoquaux. “The NumPy array: a structure for efficient numerical computation”. In: *Computing in science & engineering* 13.2 (2011), pp. 22–30.

[133] Pauli Virtanen et al. “SciPy 1.0: fundamental algorithms for scientific computing in Python”. In: *Nature methods* 17.3 (2020), pp. 261–272.

[134] Stefan Van der Walt et al. “scikit-image: image processing in Python”. In: *PeerJ* 2 (2014), e453.

[135] Aaron Meurer et al. “SymPy: symbolic computing in Python”. In: *PeerJ Computer Science* 3 (2017), e103.

[136] MJ Townson et al. “AOtools: a Python package for adaptive optics modelling and analysis”. In: *Optics express* 27.22 (2019), pp. 31316–31329.

[137] Andrew John Lewis. “Absolute length measurement using multiple-wavelength phase-stepping interferometry”. In: *Doktora Tezi* (1993).

[138] Miguel Arevallilo Herráez et al. “Fast two-dimensional phase-unwrapping algorithm based on sorting by reliability following a noncontinuous path”. In: *Applied Optics* 41.35 (2002), pp. 7437–7444.

[139] Lijun Zhu et al. “Adaptive control of a micromachined continuous-membrane deformable mirror for aberration compensation”. In: *Appl. Opt.* 38.1 (1999), pp. 168–176. DOI: 10.1364/AO.38.000168. URL: http://ao.osa.org/abstract.cfm?URI=ao-38-1-168.

[140] Eric W Weisstein. “Gibbs phenomenon”. In: *https://mathworld. wolfram. com/* (2003).

[141] Martin Booth et al. “Methods for the characterization of deformable membrane mirrors”. In: *Applied optics* 44.24 (2005), pp. 5131–5139.

[142] Sheng Liu et al. “sCMOS noise-correction algorithm for microscopy images”. In: *Nature methods* 14.8 (2017), p. 760.

[143] Biagio Mandracchia et al. “Fast and accurate sCMOS noise correction for fluorescence microscopy”. In: *Nature communications* 11.1 (2020), pp. 1–12.

[144] S Hell et al. “Aberrations in confocal fluorescence microscopy induced by mismatches in refractive index”. In: *Journal of microscopy* 169.3 (1993), pp. 391–405.

[145] Jonathan R Brent, Kristen M Werner, and Brian D McCabe. “Drosophila larval NMJ dissection”. In: *JoVE (Journal of Visualized Experiments)* 24 (2009), e1107.

[146] Dongyu Jia et al. “Automatic stage identification of Drosophila egg chamber based on DAPI images”. In: *Scientific reports* 6.1 (2016), pp. 1–12.

[147] Yongdeng Zhang et al. “Nanoscale subcellular architecture revealed by multicolor three-dimensional salvaged fluorescence imaging”. In: *Nature methods* 17.2 (2020), pp. 225–231.

[148] Daniela Leyton-Puig et al. “PFA fixation enables artifact-free super-resolution imaging of the actin cytoskeleton and associated proteins”. In: *Biology open* 5.7 (2016), pp. 1001–1009.

[149] Alexander Davidson et al. “Localized translation of gurken/TGF-α mRNA during axis specification is controlled by access to Orb/CPEB on processing bodies”. In: *Cell reports* 14.10 (2016), pp. 2451–2462.

[150] Nicolas Loyer et al. “Drosophila E-cadherin is required for the maintenance of ring canals anchoring to mechanically withstand tissue growth”. In: *Proceedings of the National Academy of Sciences* 112.41 (2015), pp. 12717–12722.

[151] Mantas Žurauskas et al. “IsoSense: frequency enhanced sensorless adaptive optics through structured illumination”. In: *Optica* 6.3 (2019), pp. 370–379.

[152] Argolight. *User Guide: Argo-SIM Slide*. English. Version 1.1. Argolight. 28 pp. June 01, 2017.

[153] Graeme Ball et al. “SIMcheck: a toolbox for successful super-resolution structured illumination microscopy”. In: *Scientific reports* 5 (2015), p. 15915.

[154] Travis J Gould et al. “Adaptive optics enables 3D STED microscopy in aberrating specimens”. In: *Optics express* 20.19 (2012), pp. 20998–21009.

[155] Sami Koho et al. “Image quality ranking method for microscopy”. In: *Scientific reports* 6.1 (2016), pp. 1–15.

[156] P Török, SJ Hewlett, and P Varga. “The role of specimen-induced spherical aberration in confocal microscopy”. In: *Journal of microscopy* 188.2 (1997), pp. 158–172.

[157] John A Nelder and Roger Mead. “A simplex method for function minimization”. In: *The computer journal* 7.4 (1965), pp. 308–313.

[158] LP Murray, J Chris Dainty, and E Daly. “Wavefront correction through image sharpness maximisation”. In: *Opto-Ireland 2005: Imaging and Vision*. Vol. 5823. International Society for Optics and Photonics. 2005, pp. 40–48.

[159] Edward J Botcherby et al. “An optical technique for remote focusing in microscopy”. In: *Optics Communications* 281.4 (2008), pp. 880–887.

[160] Mantas Žurauskas et al. “Rapid adaptive remote focusing microscope for sensing of volumetric neural activity”. In: *Biomedical optics express* 8.10 (2017), pp. 4369–4379.

[161] Jason Schmidt. “Numerical simulation of optical wave propagation with examples in MATLAB”. In: Society of Photo-Optical Instrumentation Engineers. 2010.